Contents

Part I

A search for highly ionising, short tracks at the CMS detector

1 Motivation

Supersymmetry is able to offer solutions to many unexplained phenomena in astrophysics and can solve many of the shortcomings of the Standard Model of particle physics (see Section **??**). While SUSY has been studied at previous particle colliders including Tevatron and LEP [1,2], the LHC with its high centre-of-mass energy offers a unique opportunity to investigate SUSY models with high sparticle masses that were not accessible in previous experiments.

Therefore, a variety of searches were hunting for SUSY during the run I of the LHC in 2011 and 2012. Proton-proton collision data from the CMS and ATLAS experiments were analysed with a strong focus on the search for SUSY in the strong production sector (e. g. [3–5]). As a consequence, wide, previously unexplored regions of SUSY parameter space are already excluded. However, due to the unknown mechanism of supersymmetry breaking, the most general parametrisation of the Minimal Supersymmetric Standard Model (MSSM) introduces over 100 new parameters and thus opens up an incredibly large phenomenological space. Therefore, SUSY models can lead to a plethora of possible signatures at particle colliders.

(I think it is wrong - What motivation??)

Among more "exotic" SUSY scenarios are models with compressed spectra, where two or more particles are nearly mass-degenerate. Especially scenarios with a nearly mass-degenerate lightest chargino ($\tilde{\chi}_1^\pm$) and lightest neutralino ($\tilde{\chi}_1^0$) are very interesting from a theoretical and cosmological perspective, as will be explained immediately. In R-Parity conserving Supersymmetry, such a mass-degeneracy naturally occurs in case of wino-like neutralinos and charginos, since the mass gap is fully determined by higher loop corrections (see Section **??**) and thus very small. A wino-like neutralino on the other hand is attractive from an cosmological perspective, as it can help to explain the sources of the relic density [6–8]. While it is not possible to explain the full relic density with thermally produced neutralinos for $m_{\tilde{\chi}_1^0} \lesssim 2.9\,\text{TeV}$ [9], neutralinos can still be the dominant part if they are non-thermally produced via the decay of a heavy and long-lived particle (moduli field). The enhanced annihilation cross section (called Sommerfeld enhancement) into WW- , ZZ- or ff-pairs for a wino-like dark matter candidate leads to an underprediction of the relic density if the neutralino mass is too small [10]. This underprediction can be cured, however, if there is an additional non-thermal production of dark matter as explained before. If the wino mass paramater is much smaller than the bino and higgsino

mass parameters, both, the lightest neutralino and the lightest chargino are wino-like and almost mass-degenerate. Apart from heaving a viable Dark Matter candidate, it would also lead to the prediction of a charged sparticle, that could be detected in the CMS experiment.

SUSY scenarios with nearly mass-degenerate particles have two distinctive phenomenological properties that require a very different search strategy compared to general SUSY searches. First, if the chargino and the neutralino are almost mass-degenerate ($\Delta m \lesssim 200\,\mathrm{MeV}$), the remaining decay product (e. g. a pion) is very soft in p_T, making it hard to detect. Second, the chargino is long-lived due to phase space suppression (see Section **??**) and may traverse several detector layers before decaying.

Although supersymmetric models with nearly mass-degenerate $\tilde{\chi}_1^\pm$ and $\tilde{\chi}_1^0$ lead to exotic signatures with long-lived charginos and soft decay products, existing SUSY searches at CMS can in principle be sensitive to these models. The exclusion power of existing SUSY searches can be assessed by interpreting their results in terms of the fraction of excluded parameter points in the phenomenological MSSM (see Section **??** for an introduction to the pMSSM). The results of such a study which has been performed in [11] are shown in Figure 1.1. It can be seen that general SUSY searches (blue area) are sensitive to shorter chargino lifetimes ($c\tau \lesssim 10\,\mathrm{cm}$). Due to technical reasons[1], the general SUSY searches were never interpreted in the context of SUSY models with longer chargino lifetimes. Two existing searches, the search for long-lived charged particles [12] and the search for disappearing tracks [11] focus on long and intermediate chargino lifetimes, respectively. These two searches (purple and red areas) are sensitive to chargino lifetimes of $c\tau \gtrsim 35\,\mathrm{cm}$. Taken together, the existing searches exclude a large fraction of pMSSM points at different chargino lifetimes. However, there is a gap between the general SUSY searches and the search for disappearing tracks that is not accessible by any of the existing searches.

The here presented analysis aims at targeting this gap by optimising the search strategy for charginos with intermediate lifetimes of $10\,\mathrm{cm} \lesssim c\tau \lesssim 40\,\mathrm{cm}$. The targeted optimisation strategy is a combination of the strategies used in the search for long-lived charged particles [12] and the search for disappearing tracks [11]. While in [12], the high ionisation losses of hypothetical new massive particles is exploited, it does not take into account whether its reconstructed track is disappearing. In [11], the disappearance of the track is utilised but it does not incorporate the large ionisation losses into the search. Additionally, neither of the search does take into account the possible very short tracks of a early decaying chargino. Thus, the here presented search is the first analysis at CMS combining the two signature properties that are highly distinctive for charginos with intermediate

---

[1]The pMSSM interpretation relied on the use of fast simulation techniques which are not capable of simulating charginos with lifetimes $c\tau > 1\,\mathrm{cm}$.
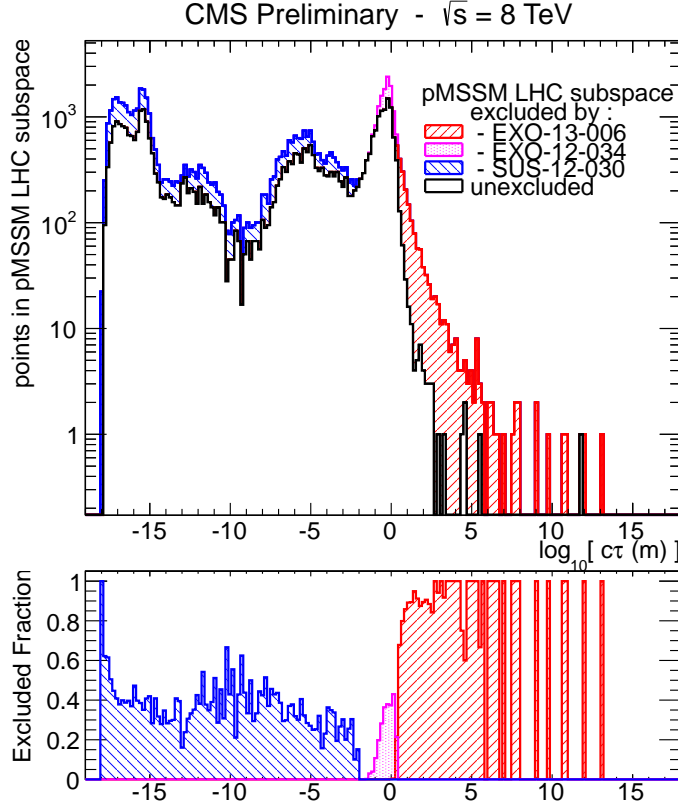
Figure 1.1: The number of excluded pMSSM points at 95% C.L. (upper part) and the fraction of excluded pMSSM points (bottom part) vs. the chargino lifetime for different CMS searches. Red area: the search for long-lived charged particles [12], Purple area: the search for disappearing tracks [11], Blue area: a collection of various general SUSY searches [13] The black line indicates the unexcluded pMSSM parameter points. The sampling of the parameter space points was done according to a prior probability density function which takes pre-LHC data and results from indirect SUSY searches into account (see [14] for further details). Taken from: [15].

lifetimes: first, the characteristically high ionisation losses of heavy charginos; second, short reconstructed tracks due to chargino decays early in the detector.

The associated challenges and the general search strategy of this analysis will be presented in the next section.

2 General search strategy

At the LHC, there are several possible chargino production channels. Chargino pairs can be produced through a photon or a Z-boson exchange. The chargino then decays via a virtual W-boson to the lightest neutralino and a fermion pair (e.g. a pion). This process is illustrated in the Feynman diagram in Fig. 2.1. Other possible chargino pair production channels include the exchange of a supersymmetric Higgs boson or a t-channel squark exchange (Fig. 2.2).

Apart from pair production, charginos can be produced via the chargino neutralino production channel. On tree-level, there exist two production mechanisms: the s-channel W-boson exchange and the t-channel squark exchange (Fig. 2.3).

Alternatively, charginos can be produced via strong production modes, i.e. in cascade decays of new heavy particles, such as gluinos or squarks. In the here presented search, the focus is, however, put on the electroweak production channels: chargino-pair and chargino-neutralino production.

When searching for supersymmetric models with long-lived $\tilde{\chi}_1^{\pm}$, the strategy is of course highly dependent on the actual lifetime of the chargino. For long lifetimes, the chargino
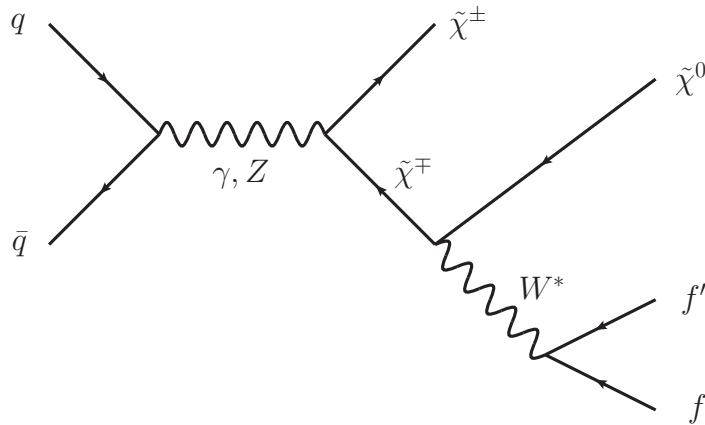

Figure 2.1: Feynman diagram of chargino pair production via gamma or Z-boson exchange and the subsequent decay via a virtual W-boson.
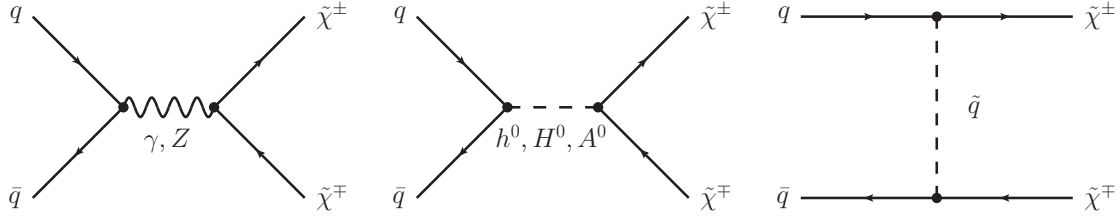
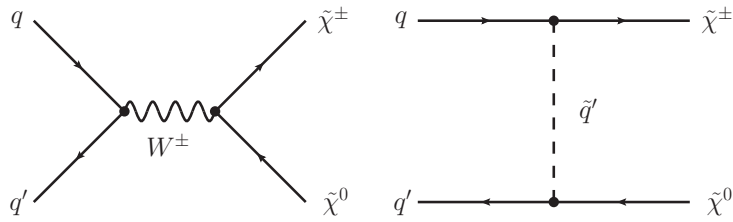Figure 2.2: Main tree-level diagrams for chargino pair production.

Figure 2.3: Main tree-level diagrams for chargino neutralino production.

can reach the muon chambers and can be reconstructed as a muon even despite a longer time-of-flight [16]. For lower lifetimes, the chargino can already decay inside the detector (e. g. the tracker), and can hence not be reconstructed as a muon but leads to an isolated, potentially disappearing track in the tracker. The detector signatures of these two scenarios are visualised in Fig. 2.4, where simulated chargino-chargino events are shown in a cross-sectional view of the CMS detector. In the left picture of Fig. 2.4, both charginos are reconstructed as muons, which can be seen in the energy deposition in the muon chambers. In the middle and right pictures both charginos have a lower lifetime of $c\tau = 0.5\,\mathrm{m}$ and thus are only visible as tracks in the tracker, where both trajectories end inside the silicon strip tracker. Since this analysis targets a search for Supersymmetry with charginos of lifetimes between $c\tau \approx 10\,\mathrm{cm} - 40\,\mathrm{cm}$, the charginos decay rather early in the detector, even in the inner layers of the tracker. Thus, the signature of chargino events consists of isolated, short tracks and the signatures of the decay products, i. e. of a neutralino and a fermion pair.

In case of R-parity conservation one of the chargino decay products, the neutralino, is stable and weakly interacting, thus traversing the detector without leaving any further signature.

The signature of the other decay product, the fermion pair, can in principle be used to select chargino events. However, for mass-degenerate charginos, it can be very hard or even impossible to detect these fermions as will be explained in detail in the next paragraph.

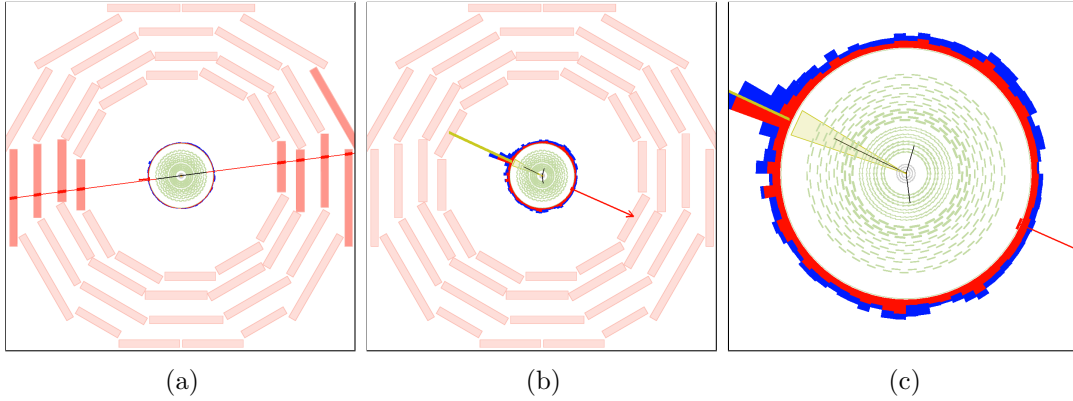(a)   (b)   (c)

Figure 2.4: Visualisation of possible signatures of a chargino pair produced with a lifetime of $c\tau = 10$ m (a) and a lifetime of $c\tau = 0.5$ m (b and c). The muon chambers are the outer layers of the detector and are depicted as red boxes. The black lines represent the reconstructed chargino tracks. The right picture is a zoom of the picture in the middle. Here, only the cross-section of the tracker (green wavy lines for the strip and grey lines for the pixel) is displayed. The red arrow shows the missing transverse energy in the event. The red (blue) towers correspond to the energy deposition in the ECAL (HCAL).

First of all, the fermionic decay product (e. g. a pion) can usually not be reconstructed because it does not origin from the primary vertex. Secondly, it is very low in momentum because of the mass-degeneracy between $\tilde{\chi}_1^\pm$ and $\tilde{\chi}_1^0$. The typical momentum of a pion originating from a chargino to neutralino decay in the $\tilde{\chi}_1^\pm$ rest frame is of the order

$$p_\pi \sim \sqrt{m_{\chi_1^\pm} - m_{\chi_1^0} - m_\pi}. \tag{2.1}$$

For a mass gap between $\tilde{\chi}_1^\pm$ and $\tilde{\chi}_1^0$ of $\Delta m = 150$ MeV, the pt distribution of the resulting pion peaks at ~ 100 MeV and ends at $p_\mathrm{T} \sim 400$ MeV (Fig. 2.5).

If the transverse momentum of a particle is very low, the particle trajectory is much more bended compared to a particle with higher p_T (see Fig. 2.6 for illustration). Due to this bending, the track reconstruction efficiency of particles with a transverse momentum below 1 GeV decreases rapidly, reaching around 40% for isolated pions with a p_T of 100 MeV [17]. Furthermore, for pions that are not produced in the primary vertex, this reconstruction efficiency will be even smaller. It is therefore impossible to rely on a reconstruction of the fermionic chargino decay products in this analysis.

In summary, since an early decaying chargino is not reconstructed as a PF particle, the event signature of a chargino-pair or a chargino-neutralino event consists only of one (or two) - potentially - disappearing track. Such a signature is very difficult to detect, especially since CMS doesn't offer a dedicated track trigger so that triggering on the
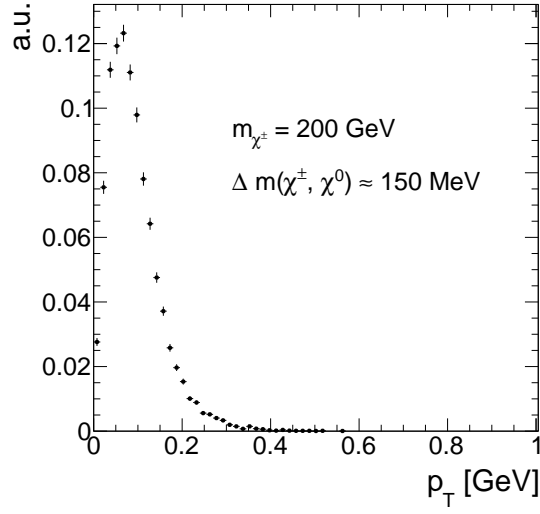
Figure 2.5: Transverse momentum distribution of pions coming from chargino decay into a neutralino with a mass gap of 150 MeV.

chargino track is impossible.

In order to search for such signatures, one therefore needs to trigger on other, less obvious properties of chargino events. This analysis takes advantage of higher order contributions to the Feynman diagrams shown in Figs. 2.2 and 2.3, resulting in initial state radiation (ISR). If the initial quarks radiate a high p_T gluon, the resulting jet can be detected and can offer a possibility to search for events with nothing more than isolated tracks. Furthermore,
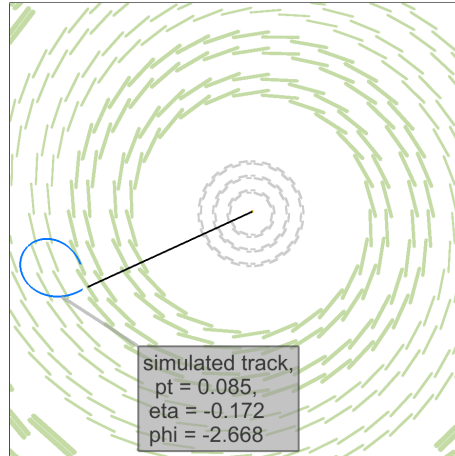
Figure 2.6: Cross-sectional view of the tracker (silicon strip (silicon pixel) tracker layers are illustrated with green (grey) lines) and a simulated chargino track (black line) decaying to a pion (bended blue line) with a p_T of $\sim$85 MeV and a neutralino (not visible).

159 the non-detection of the chargino's decay products plus a high p_T ISR jet lead to missing
160 transverse energy (MET) in the event. Exploiting these two circumstances, it is possible
161 to detect chargino-pair or chargino-neutralino events with the help of Jet+MET triggers.

162 Since Jet+MET triggers are not very specific for chargino events, it is important to
163 identify further track properties that can be used to select chargino candidates. One
164 distinctive property of charginos compared to SM particles is their high mass. Therefore,
165 charginos can be identified by selecting high p_T tracks. Furthermore, the energy loss
166 per path length (dE/dx) depends quadratically on the particle's mass for low velocities
167 ($0.2 < \beta\gamma < 0.9$):

$$\langle\frac{dE}{dx}\rangle = K\frac{m^2}{p^2} + C$$

168 Therefore, dE/dx constitutes a very nice discriminating variable for massive particles like
169 charginos against SM particles. The selection of chargino events in this analysis thus relies
170 on the selection of isolated high p_T tracks with high dE/dx values.

171 If the chargino decays before it has crossed the full pixel and strip detector, the as-
172 sociated track is disappearing. For low lifetimes, the tracks can be very short and can
173 have only a few hits in the detector. In order to reconstruct a particle's trajectory, a
174 minimum of three hits are required since defining a helical path requires five parameters
175 (see [17]). A specific challenge for this analysis is hence the combination of searching for
176 short tracks and utilising the measurement of the energy deposition of the chargino. For
177 very short tracks, eventually only passing the first couple of layers of the whole tracker
178 system, the pixel tracker information becomes very important. Therefore, an accurate
179 energy measurement in the pixel system is of great importance to this analysis. However,
180 no other CMS analysis has used the energy information of the pixel tracker so far. This
181 analysis thus requires a thorough study of the quality of the pixel energy calibration and,
182 potentially, a recalibration in case the pixel energy calibration is not sufficient.

2.1 Comparison to earlier searches

184 As already mentioned before, there are two analyses at CMS at $\sqrt{s} = 8$ TeV with $20\,\mathrm{fb}^{-1}$
185 data that search for intermediate lifetime charginos, the search for long-lived charged
186 particles [12] and the search for disappearing tracks [11]. The here presented analysis
187 aims at achieving an increase in sensitivity towards shorter lifetimes compared to the ear-
188 lier analyses in a twofold way. First, the selection is optimised for the inclusion of very
189 short tracks. Second, the inclusion of the variable dE/dx is used to increase the search
190 sensitivity compared to [11].

192 In [12], a minimum number of eight hits were required for every track, whereas [11]
193 required a minimum of seven hits. This can be very inefficient for shorter lifetimes, where

most of the charginos already decay shortly after the pixel tracker. In Fig. 2.7 (left), the normalised distribution of the number of measurements (N_{hits}) of chargino tracks is shown. It can be seen, that N_{hits} peaks at the minimal possible value needed for track reconstruction of $N_{\text{hits}} = 3$ for lower lifetimes. For a lifetime of $c\tau = 50\,\text{cm}$, a second peak at ~ 17 hits appears corresponding to the number of measurements when crossing all pixel barrel (3) and strip inner and outer barrel (6 from stereo and 8 from normal) layers. However, a notable fraction of $\sim 40\%$ of chargino tracks still has a number of measurements of $N_{\text{hits}} < 8$.

It should be also mentioned, that the track reconstruction efficiency is sufficient for short chargino tracks, such that a loosening of the N_{hits} requirement is expected to be really improving the signal acceptance. The track reconstruction efficiency for different chargino decay points is depicted in Fig. 2.7 (right). For very short tracks ($N_{\text{hits}} = 3$) the efficiency is still around 20%.

Additionally, the search for disappearing tracks which targets models with charginos decaying inside the tracker did not make use of the high energy deposition of heavy particles. Although this variable was indeed used in the search for long-lived charged particles, this search was not optimised for intermediate lifetimes (e. g. no explicit muon veto on the selected tracks was required). Thus, it shows less sensitivity compared to the disappearing track search in the lifetime region between $35\,\text{cm} \lesssim c\tau \lesssim 100\,\text{cm}$ (see Fig. 1.1).
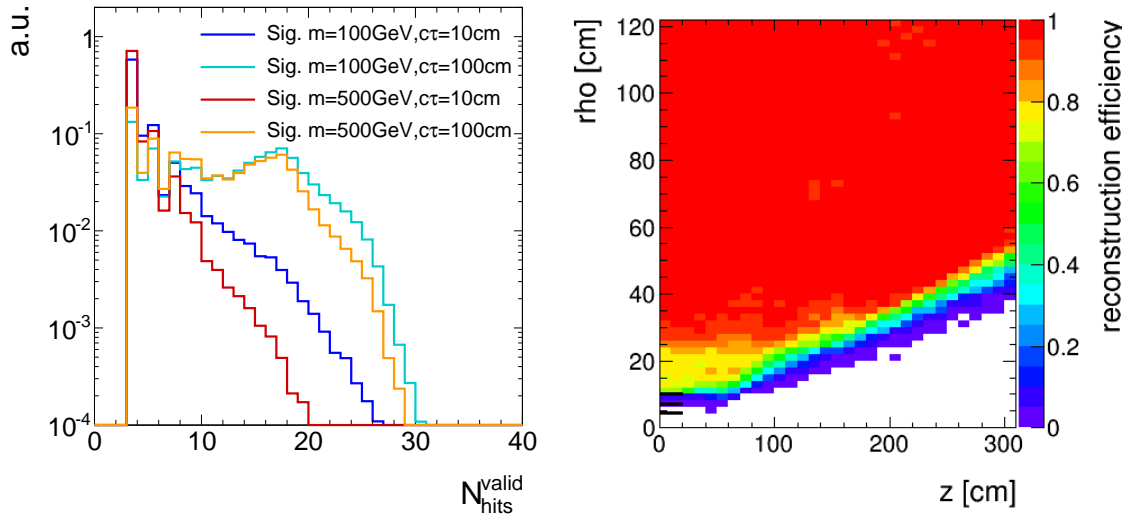

Figure 2.7: Left: Number of measurements in the tracker system N_{hits} for four different signal lifetimes. Right: Probability to reconstruct a track (z) in dependency of the chargino's decay point (x and y). More information on the generation of the simulated signal samples can be found in Section **??**.

214

215   To conclude, the general search strategy of the here presented analysis is to unite the
216   strategies of [12] and [11] and to lower the strong selection on the number of hits in these
217   analyses in order to get an optimised selection for lifetimes around $10\,\mathrm{cm} \lesssim c\tau \lesssim 40\,\mathrm{cm}$.

3 Improved dE/dx measurement for short tracks

219   As already pointed out in the previous chapter, the inclusion of the pixel energy mea-
220   surements can increase the sensitivity when searching for short and highly ionising tracks.
221   While the energy measurements in the silicon strip detector have already been calibrated
222   as part of the search for long-lived charged particles [12], no complete calibration has been
223   done for the pixel silicon tracker so far. To increase the discrimination power of dE/dx for
224   short tracks, such a calibration procedure is therefore conducted within this PhD thesis.
225   The CMS tracker system provides a measurement of the particle's energy loss for each
226   hit in the tracker. This is done by the detection of the number of electrons produced by
227   the ionisation of the silicon. A detailed introduction to the CMS tracker system and the
228   energy measurement can be found in Section **??**.
229   How to combine the single energy measurements for each tracker hit into one track
230   dE/dx estimator that can be used for analysis purposes will be explained in the following
231   Section 3.1. The pixel energy calibration is then described in Section 3.2. How to dis-
232   criminate SM particles and beyond SM particles with the help of a dE/dx measurement
233   is discussed in Section 3.3, followed by an exploration of how the inclusion of the pixel
234   energy measurements in the dE/dx estimates leads to a better discrimination between
235   Standard Model particles and long-lived charginos (Section 3.4).

3.1 Estimation of the ionisation loss of charged particles

237   Energy losses for moderately relativistic charged particles travelling through matter are
238   mostly caused by ionisation effects. The mean energy loss per path length can be described
239   with the Bethe formula [18]:

$$\langle \frac{dE}{dx} \rangle = K z^2 \frac{Z}{A} \frac{1}{\beta^2} \big[\frac{1}{2} \ln \frac{2 m_e c^2 \beta^2 \gamma^2 T_{\max}}{I^2} - \beta^2 - \frac{\delta(\beta\gamma)}{2} \big]. \tag{3.1}$$

240   It is a function of the atomic number (Z), the atomic mass (A) of the absorber, and the
241   mean excitation energy (I) which is $173\,\mathrm{eV}$ for silicon [19]. $T_{\max}$ represents the maximum
242   energy transfer in a single collision. The relevant particle's properties are the velocity (β),

the Lorentz factor (γ) and the charge (z) of the incident particle. The density correction $\delta(\beta\gamma)$ reduces the mean energy loss at high energies because of polarisation effects of the material. The factor K is constant and is 0.307 in units of $\text{MeV} \, \text{mol}^{-1} \text{cm}^2$. The Bethe formula is valid if the main energy loss originates from ionisation effects, i.e. in a region between $0.1 \lesssim \beta\gamma \lesssim 1000$.

Even if widely used, the mean energy loss is a quantity which is "ill-defined experimentally and is not useful for describing energy loss by single particles" [20]. The problem is caused by the underlying probability distribution of one single dE/dx measurement (this will be named $\Delta E/\Delta x$ throughout the following sections), which can be parametrised by a Landau distribution [21]

$$p(x) = \frac{1}{\pi} \int_0^\infty e^{-t \log t - xt} \sin(\pi t) \, dt. \qquad (3.2)$$

The Landau distribution has no free parameters. Its most probable value is around 0.222. However, it is possible to introduce artificially a different most probable value and a width (at half maximum) with $x \to \frac{x - \text{MPV}}{\sigma} - 0.222$. The Landau distribution is a highly asymmetric distribution with a long tail towards the right end (see Fig. 3.1). Theoretically it extends to infinite energies, however in nature the maximal deposited energy is of course limited by the particle's full energy.

Because of its strong asymmetry, measurements of the mean energy loss per path length $\langle dE/dx \rangle$ with only a few single measurements are easily fluctuating towards high values. This makes the use of the mean energy loss described by the Bethe formula for the discrim-
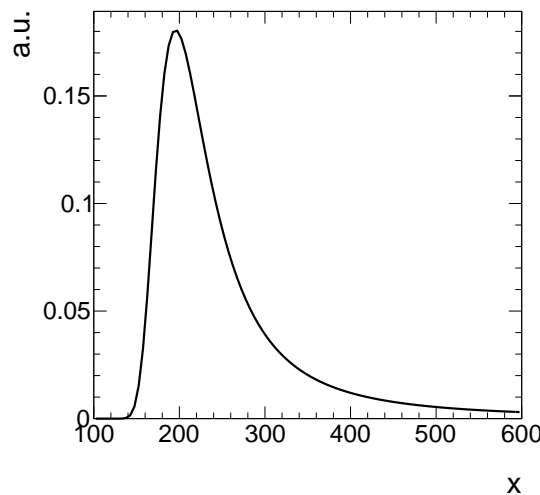

Figure 3.1: Illustration of the shape of a Landau distribution. Parameters were chosen as $\mu = 200$ and $\sigma = 20$.
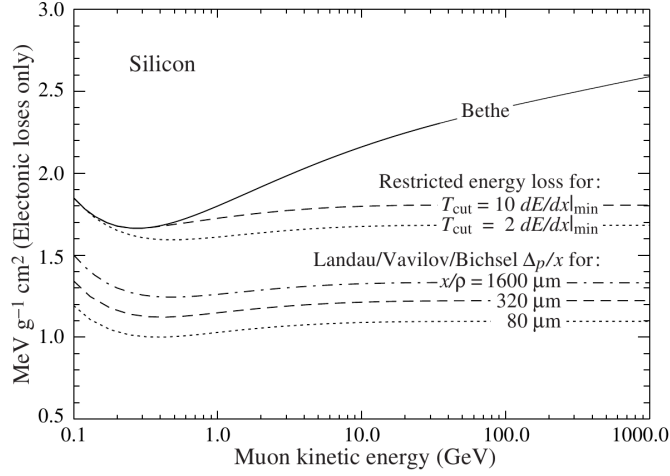
Figure 3.2: Comparison between the Bethe mean energy loss, restricted energy loss and the most probable energy loss described by the Landau-Vavilov-Bichsel function for muons for different values of absorber thickness of silicon. Taken from [20].

ination of new heavy particles problematic, because fluctuations to high values reduce the discrimination power against massive particles which release in general higher amounts of energy in matter.

A much better observable is the most probable value (MPV) of the Landau distribution. The MPV is much more stable compared to the mean and is not as easily fluctuating to higher dE/dx values. The most probable energy loss of a charged particle, Δ_p, can be described by the Landau-Vavilov-Bichsel equation [22]:

$$\Delta_p = \xi \left[\ln \frac{2m_e c^2 \beta^2 \gamma^2}{I} + \ln \frac{\xi}{I} + j - \beta^2 - \delta(\beta\gamma) \right], \qquad (3.3)$$

with $\xi = (K/Z)\langle Z/A \rangle (x/\beta^2)$. The thickness of the absorber x appears explicitly in the Landau-Vavilov-Bichsel equation making the most probable energy loss per path length Δ_p/dx logarithmically dependent on x. A comparison between the Bethe mean energy loss $\langle dE/dx \rangle$ and the most probable energy loss Δ_p/dx for muons is shown in Fig. 3.2.

Particles such as muons are minimally ionising in silicon for $\beta\gamma \sim 3 - 4$. For higher momenta the deposited energies increase again reaching a plateau at around $\beta\gamma \sim 100$. However, new heavy charged particles would mainly be unrelativistic because of their high mass and would therefore deposit much higher energies in the detector. This makes dE/dx a very well discriminating variable. Thus, the energy loss per path length can be used to discriminate between SM particles and new heavy charged particles due to the different velocity distributions.

As said before, the most probable energy loss is much more stable compared to the Bethe mean energy loss. Still, combining only a few measurements of $\Delta E/\Delta x$ can also lead for Δ_p/dx to large fluctuations towards high dE/dx values. In order to estimate experimentally the most probable dE/dx value from only a few energy measurements, several "estimators" can be used that suppress a potential bias towards the high end without introducing a bias towards lower values [23]. One of the estimators for determining a track's dE/dx is the harmonic-2 estimator

$$I_{\mathrm{h2}} = \left(\frac{1}{N} \sum_{i=1}^{N} (\Delta E_i/\Delta x_i)^{-2} \right)^{-1/2}, \tag{3.4}$$

where $\Delta E_i/\Delta x_i$ corresponds to the ΔE and Δx measurement in the ith hit of the track. This estimator is known to be robust and not be easily biased by large fluctuations in $\Delta E/\Delta x$ because of the suppression by the power of minus two.

3.2 Energy calibration of the silicon pixel tracker

During Run I in 2012, the pixel silicon detector was continuously subjected to an energy calibration, a so-called gain calibration. Every pixel was calibrated to the same response, so that the whole pixel tracker should have been well inter-calibrated [24]. Unfortunately, due to various reasons, such as the imperfect constancy of the reference signal, or radiation and temperature induced changes, the energy calibration could not ensure a fully calibrated pixel tracker.

This imperfection of the gain calibration can be seen in Fig. 3.3, where the mean of the harmonic-2 estimator for all tracks $\langle I_{\mathrm{h2}} \rangle$ over the full data-taking period in 2012 is shown. Four different steps can be spotted. The first and the third steps correspond to changes in the settings of the tracker due to irradiation. The second and fourth step are induced by associated adjustments in the online gain calibration. Unfortunately, although the gain calibration was adjusted (even with some delay), it was not able to ensure a constant energy response of the pixel tracker over time. The variations of the dE/dx measurement over time of around 15% are too large to use dE/dx without a further calibration.

The following sections explain the method of the gain calibration of the pixel silicon tracker which is conducted for this analysis. It is splitted into two sections. The first section is dedicated to the gain inter-calibration of the pixel tracker which ensures a homogeneous energy response of all tracker modules. In the second section, the absolute gain calibration is discussed. This calibration step is needed to ensure that the measurement of the energy release of a particle is actually translated to the correct physical value.

Inter-calibration of gain

The main goal of the gain calibration is to get a uniform response in the ionisation energy loss dE/dx over the full data taking period in 2012. To also ensure a uniform response over all modules within one time step, an additional inter-calibration on module level is carried out. The inter-calibration can in principle be done on various levels: the highest granularity would be a calibration on pixel level, followed by a calibration on read-out-chip (ROC) level and then on module-level. Lower granularities in descending order are rings (modules with same z-position) and finally layers (3 layers in the barrel and 4 disks in the endcap). It is verified that all pixels and all ROCs (on one module) are well inter-calibrated, such that the inter-calibration is finally done module-wise.

The gain calibration of the pixel silicon tracker is carried out with the help of minimally ionising particles (MIPs). MIPs in this context are not defined as particles at the minimum of the Bethe formula, but more generally as particles located at or near the plateau of the dE/dx distribution vs. momentum (see Fig. 3.2). This approach ensures that all particles deposit similar amounts of energy so that the variation due to different momenta is minimised.

MIPs are selected by a momentum selection of p > 2 GeV. Additionally, only tracks with at least eight hits and a χ^2/n.d.o.f. < 3 are used to ensure a high-quality track reconstruction. A sample containing around 50 million "minimum bias" events is used for calibration. The "minimum bias" sample was specifically recorded for tracker calibration purposes.

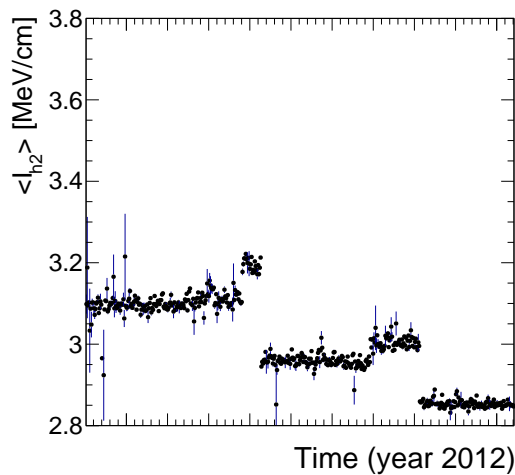For every module in the pixel tracker (there are 1440 modules in total), a distribution

Figure 3.3: Mean of all track's dE/dx (harmonic-2 estimator) over the full year 2012. Only pixel hits are taken into account. Every data point corresponds to one run.
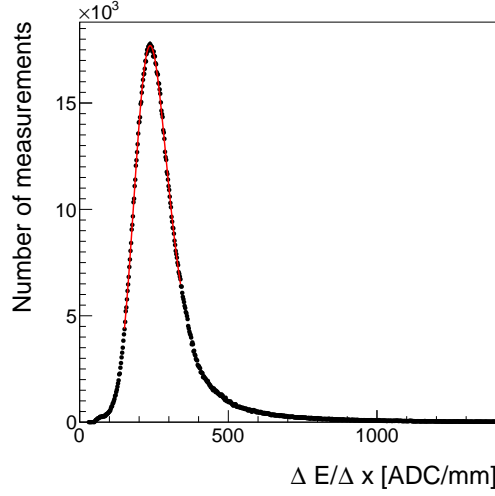
Figure 3.4: An example of the $\Delta E/\Delta x$ distribution measured in ADC count per mm for one module of the CMS pixel tracker. A Landau convoluted with a Gaussian is fitted to the core of the distribution in an iterative procedure.

of the energy loss per path length $\Delta E/\Delta x$ is built. The measurement of $\Delta E/\Delta x$ is done in ADC counts per mm. ADC counts are a measure for the deposited charge after digitisation. Figure 3.4 shows an example distribution for one module. The underlying Landau distribution can be nicely seen. To extract the MPV for every module a fit to the core distribution is performed. The fit is not only done with a Landau but a Landau convoluted with a Gaussian function to be closer to the experimentally observed energy spectrum. This also increases the fit performance and the stability of the fit. The path length Δx is calculated with

$$\Delta x = d_{\text{module}_i} \cdot \cos(\phi_{\text{track}}), \tag{3.5}$$

where d_{module_i} is the thickness of module i and ϕ_{track} is the relative angle of the particle's trajectory to the normal axis of the module. With the measured MPV extracted from the fit, an inter-calibration factor is calculated for every module

$$c_{\text{inter}} = \frac{\text{MPV}_{\text{target}} \, [\text{ADC/mm}]}{\text{MPV} \, [\text{ADC/mm}]} = \frac{300 \cdot 265 \, \text{ADC/mm}}{\text{MPV} \, [\text{ADC/mm}]}. \tag{3.6}$$

The factor $300 \cdot 265 \, \text{ADC/mm}$ is in principal an arbitrary number since the final response is adjusted by the absolute gain calibration described in the next section. However, it is chosen such that the measured calibration factors are close to one. The calibration factor can then be used to scale every single measurement in a module to a calibrated
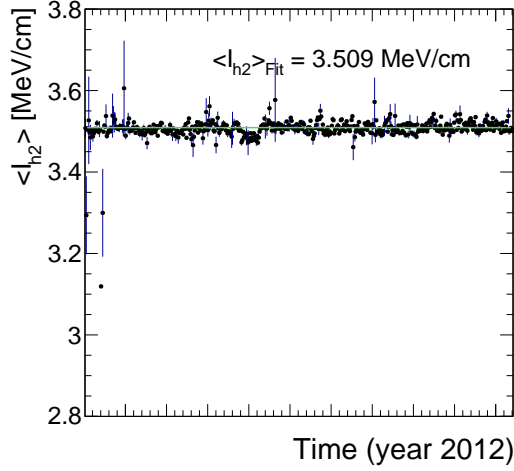
Figure 3.5: Mean of all track's dE/dx (harmonic-2 estimator) over the full year 2012 after applying the calibration factors, resulting in an average dE/dx of 3.51 MeV/cm. Only pixel hits are taken into account. Every data point corresponds to one run.

$\Delta E/\Delta x$ measurement

$$\left(\frac{\Delta E}{\Delta x}\right)_{\text{calibrated}} = c_{\text{inter}} \cdot \left(\frac{\Delta E}{\Delta x}\right)_{\text{uncalibrated}} \tag{3.7}$$

The determination of the calibration factor is done for every of the five time steps, shown in Fig. 3.3 independently, in order to get rid of the time dependency. The outcome of the application of the calibration factors to the single energy measurements in the pixel tracker can be seen in Fig. 3.5. The variation over time is indeed eliminated, resulting in a maximal time variation of less than $\sim 1\%$.

Additionally, the same procedure is carried out for a corresponding simulated data sample to ensure the inter-calibration of the pixel modules on all simulated samples.

Absolute calibration of gain

As a final step, the targeted MPV being $\text{MPV}_{\text{target}} = 300 \cdot 265 \, \text{ADC/mm}$ needs to be translated to a meaningful physical quantity given in physical units (e. g. MeV/cm). That means, that the charge measurement in ADC counts needs to be converted to the real energy release from a particle. The relation between ΔE in ADC counts and the energy loss in eV is given by

$$\Delta E\,[\text{eV}] = c_{\text{inter}} \cdot \Delta E\,[\text{ADC}] \cdot \frac{N_e}{\text{ADC}} \cdot 3.61 \text{ eV}, \tag{3.8}$$

where $N_e/$ADC is the number of electrons which correspond to one calibrated ADC count and 3.61 eV is the mean energy needed to create one electron-hole pair in silicon at - 10°C. Such an absolute gain calibration can be done with the help of several methods (all explained in [23]). The absolute calibration of the silicon pixel tracker can rely on the already conducted absolute calibration of the silicon strip detector. In [23], the absolute gain calibration was done with the help of the most probable energy release per path length of muons, theoretically described by the Landau-Vavilov-Bichsel formula in Eq. (3.3). To calibrate the pixel tracker to the correct energy loss per path length it is therefore sufficient to determine one calibration factor to relate the average dE/dx of all tracks in the pixel tracker as shown in Fig. 3.5 to the average measured dE/dx in the strip tracker, shown in Fig. 3.6 by

$$c_{\text{absolute}} = \frac{\langle dE/dx_{\text{strip}} \rangle}{\langle dE/dx_{\text{pixel}} \rangle} = \frac{3.303}{3.509} = 0.941. \tag{3.9}$$

This factor is then applied on top of c_{inter} for all pixel modules.

Finally, an absolute calibration factor needs to be determined for the simulated samples, where the simulated pixel tracker is calibrated to the average dE/dx of the silicon strip measured in data.
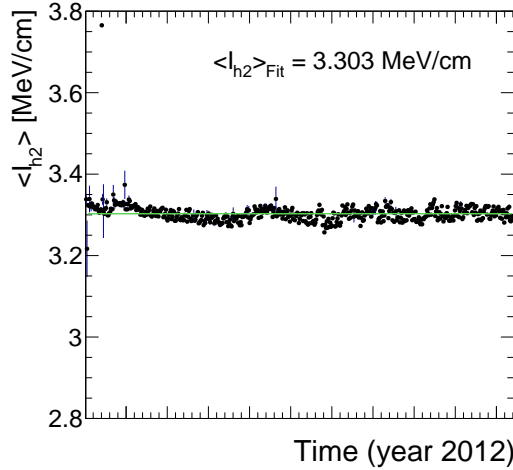

Figure 3.6: Mean of all track's dE/dx (harmonic-2 estimator) measured in the silicon strip detector over the full year 2012. The average most probable dE/dx is $I_{\text{h2}} = 3.303$ MeV/ cm. Every data point corresponds to one run.

3.3 Discrimination of highly-ionising particles

As mentioned before, it is difficult to find a robust estimator for the most probable energy loss of a particle, if only a few measurements of $\Delta E/\Delta x$ along the particle's trajectory are available. The harmonic-2 estimator I_{h2} was already introduced in Section 3.1 in Eq. (3.4). It is known to be a robust estimator not easily affected by large fluctuations in $\Delta E/\Delta x$. However, it was shown in [23] that a better discrimination between SM particles and possible new heavy particles can be achieved when using likelihood techniques, i. e. determining the probability that the set of all $\Delta E/\Delta x$ belonging to one track is actually compatible with the hypothetical probability distribution of a MIP.

That a measured sample has been drawn from a specific distribution can be tested with the co-called Smirnov-Cramér-von Mises test [25, 26]. It is deduced from the integral of the squared difference of a measured distribution to a hypothesis distribution, and leads to a test statistics of [23]

$$I_s = \frac{3}{N} \cdot \left(\frac{1}{12N} + \sum_{i=1}^{N} \left[P_i - \frac{2i-1}{2N} \right]^2 \right), \tag{3.10}$$

where N is the total number of energy measurements and P_i is the cumulative probability that a MIP would release a $\Delta E/\Delta x$ equal or smaller than the measured $\Delta E/\Delta x$ with all P_i arranged in increasing order.

However, this test statistics is not sensitive to the sign of the difference between the measured and the theoretical distribution. It can therefore not distinguish between incompatibilities due to variations towards higher or lower energy deposits compared to the hypothesis distribution. Thus it is not suitable for the discrimination between MIPs and heavy new particles by dE/dx. A so-called Asymmetric Smirnov-Cramér-von Mises discriminator was developed in [23] which is only sensitive to incompatibilities to the MIP hypothesis towards higher energy depositions

$$I_{as} = \frac{3}{N} \cdot \left(\frac{1}{12N} + \sum_{i=1}^{N} \left[P_i \cdot \left(P_i - \frac{2i-1}{2N} \right)^2 \right] \right). \tag{3.11}$$

A value of I_{as} close to zero indicates good compatibility with the MIP hypothesis, whereas a value close to one indicates bad compatibility because of unexpectedly high energy losses.

The underlying probability P_i of the energy release for a given path length in the pixel tracker is extracted from the same "minimum bias" sample used for the pixel energy calibration. In total 28 different templates each for a different given path length are created. In Fig. 3.7 the probability distribution template for the pixel tracker in data and simulation is shown. The corresponding templates for the energy release in the silicon strip detector were already built by [23].
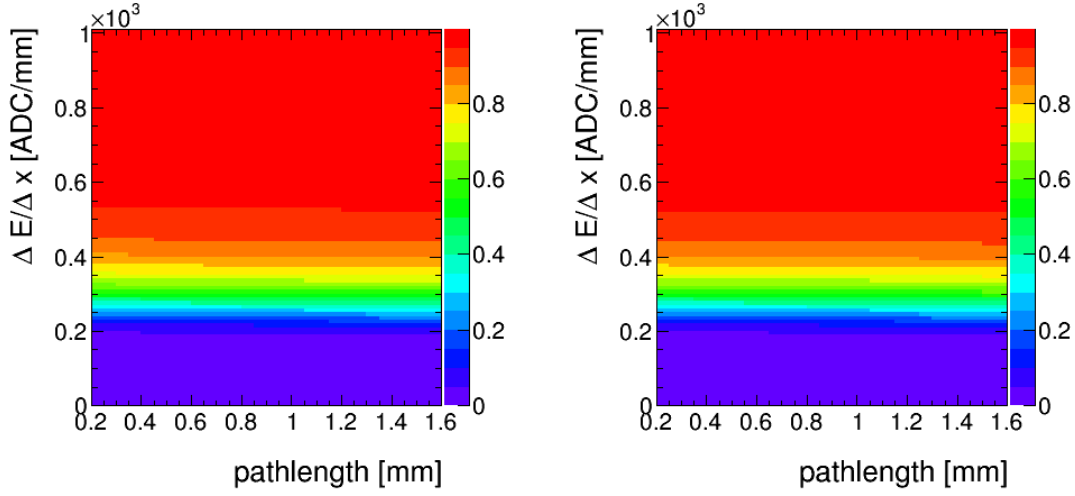
Figure 3.7: Cumulative probability for a MIP to release a $\Delta E/\Delta x$ (y-axis) vs. the path length (x-axis) in data (left) and simulation (right) for the pixel tracker based on the "minimum bias" sample.

A comparison between the energy release by MIPs (I_{as}) in data and simulation for high-quality tracks with $p > 5\,\mathrm{GeV}$ and $|\eta| < 2.1$ can be found in Fig. 3.8.

dE/dx shows good agreement in data and simulation for $I_{as} < 0.1$. For larger values, I_{as} shows a larger decrease in simulation than in measured data. For this reason a data-based approach for analyses exploiting dE/dx information is needed.

3.4 Discrimination improvements

The goal of including the pixel energy information is to increase the discrimination power of I_{as} between background and signal tracks, especially for shorter lifetimes. In Fig. 3.9 (left), a comparison of the shapes of the energy release by MIPs and by signal tracks in simulation is shown (details about the simulated samples can be found in the next section Section **??**). It can be seen, that the I_{as} distributions of the signal models show a larger tail towards $I_{as} = 1$, whereas the I_{as} of the background is rapidly falling.

In the right part of Fig. 3.9, a comparison of four different signal models is shown. Charginos with longer lifetimes have a more pronounced tail toward $I_{as} = 1$. This can be understood with the help of Eq. (3.3), where the influence of the velocity (β) on the
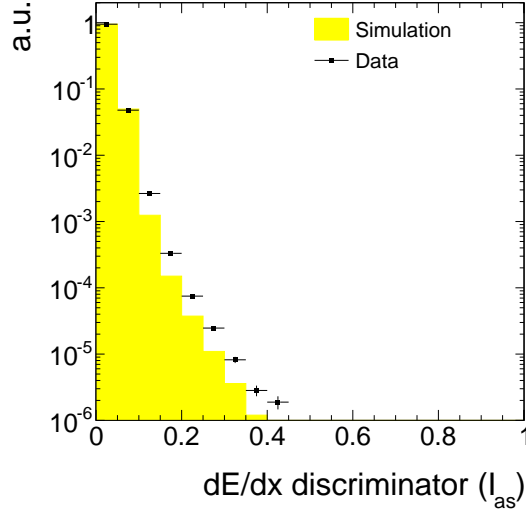
Figure 3.8: Normalised I_{as} distribution for MIPs from the minimum bias sample in data and simulation for high-quality (high purity as defined in [27], a minimum number of eight hits and no missing inner and middle hits) tracks with $p > 5\,\mathrm{GeV}$ and $|\eta| < 2.1$.
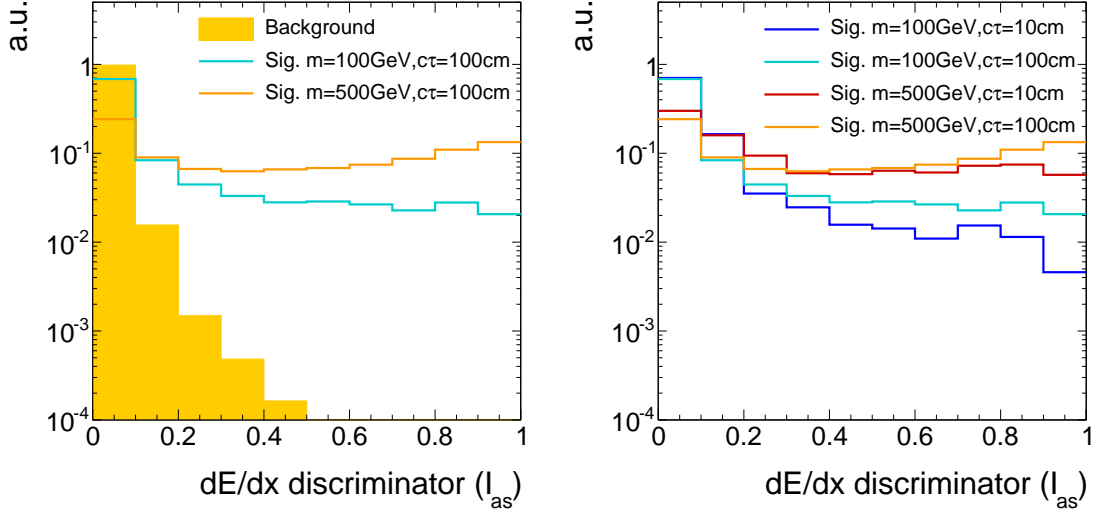
Figure 3.9: Normalised I_{as} distribution for simulated background and signal tracks (left) and for four different signal models (right) for high-purity tracks (as defined in [27]) with $p_{\mathrm{T}} > 10\,\mathrm{GeV}$ and $|\eta| < 2.1$. For the illustration of the background tracks' spectrum simulated $t\bar{t}$+jets events are used (more information about this sample is given in Section **??**).

ionisation loss can be seen. The velocity distribution of the charginos is mostly affected by the mass of the chargino. However, also for charginos with same mass, the velocity is higher in average for shorter lifetimes. This is caused by the fact, that for shorter lifetimes (e. g. $c\tau = 10\,\text{cm}$), already a sizable fraction of the charginos decay before reaching the tracker system. The probability of reaching the detector increases for higher velocities because of the boost, which can be clearly seen at the survival probability

$$P\left(t\right) = e^{-\frac{t}{\gamma\tau}}. \tag{3.12}$$

This means that the track reconstruction/selection lead to a biased average β for shorter lifetimes which in turn lead to lower values of I_{as}.

The I_{as} distribution is not only influenced by the velocity of a particle but also by the number of hits of a track. The number of measurements in the tracker system defines the influence of single fluctuations in $\Delta E/\Delta x$ on the I_{as} discriminator, because of the long right tail of the Landau distribution. A low number of hits lead therefore to higher I_{as} values. This effect is also visible Fig. 3.9 (right) by the small surplus for lower lifetimes between 0.1 and 0.2 is caused by the smaller number of measurements for earlier decaying charginos.

Finally, the impact of the additional $\Delta E/\Delta x$ information from the pixel tracker on the selection efficiency of signal and background tracks is quantified. Figure 3.10 shows the signal selection efficiency against the background selection efficiency for different selection cuts in I_{as}, once including the pixel information and once without it. The background selection efficiency is estimated with simulated W+jets events but was additionally checked on simulated $t\bar{t}$+jets and QCD-multijet events (further information about the simulated samples can be found in the next section). No significant difference between these processes in the background selection efficiency was observed.

The signal selection efficiency and the background suppression depend on the mass and the lifetime of the charginos. The improvement of the discriminating power is much more pronounced for higher chargino masses.

It can be seen that the inclusion of the pixel information increases the background suppression for a given signal efficiency throughout the investigated signal models. This background suppression improvement is most pronounced for very tight cuts on I_{as} up to a factor of 20 and even more and still considerable for looser selections with signal efficiencies of around 40% (factor of 10).
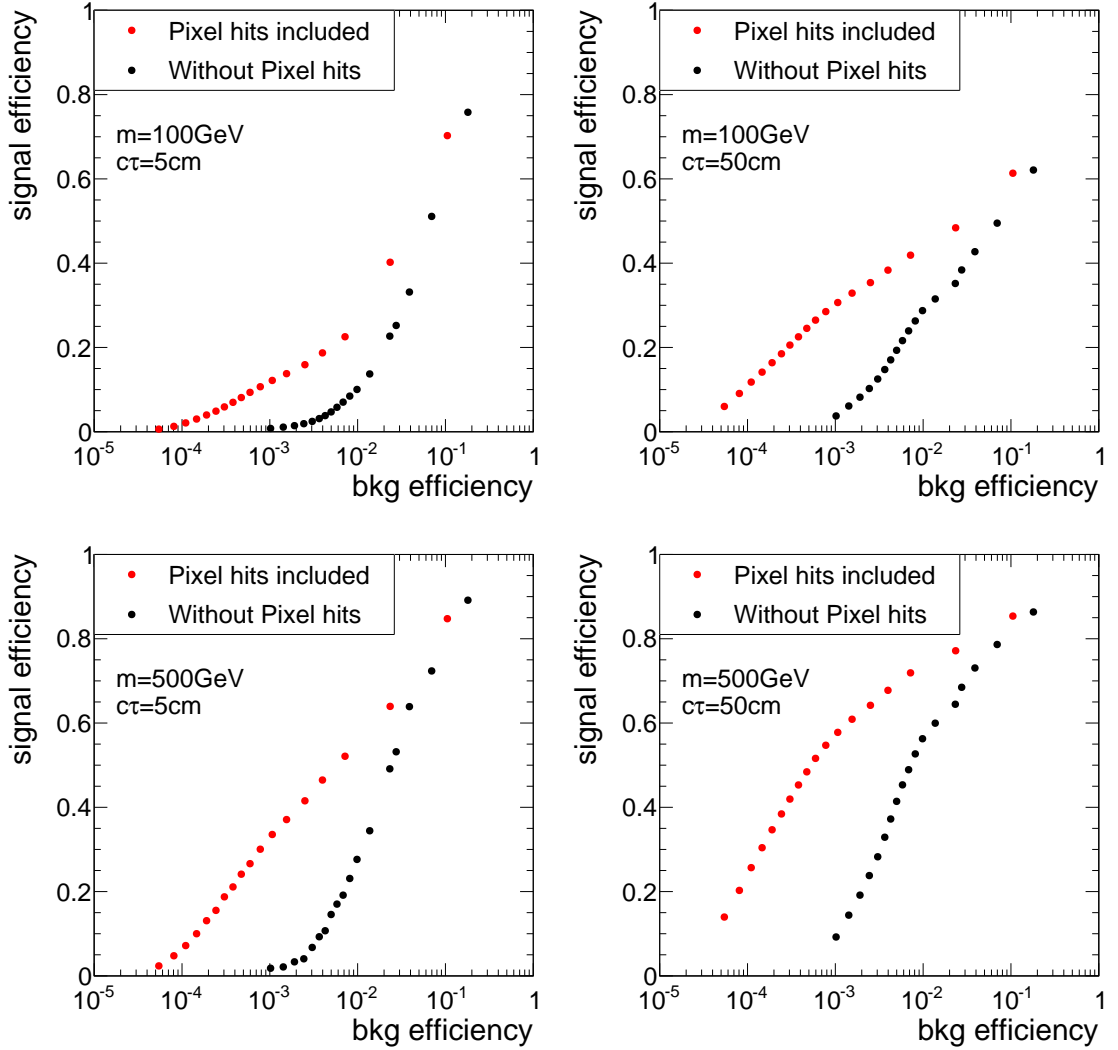
Figure 3.10: Signal selection efficiency vs. background selection efficiency with (red) and without (black) pixel information. Each point correspond to one selection cut in I_{as}. The figure is based on a simulated $W + \text{jets}$ sample and a simulated signal sample with chargino-chargino production, both subject to a selection of high-quality tracks (without a selection on N_{hits}) with $p_{\text{T}} > 10\,\text{GeV}$.

4 Simulated samples

In order to design the search and to study background and signal characteristics, this analysis relies on simulated SM and SUSY datasets. An extensive introduction to the techniques and tools required for the simulation of SM and beyond SM processes can be found in Section **??**.

The following two sections present an overview of the SM (Section **??**) and SUSY samples (Section **??**) used in this search. All samples are reweighted to match the measured distribution of primary vertices per event in data. Additionally, event weights are applied to ensure the same ISR spectrum in simulation as in data.

4.1 Standard Model background samples

To investigate the sources of background, various simulated SM samples are used. Since this analysis aims at making use of dE/dx, a special data format of the simulated samples, the so-called RECO format, is required. Unfortunately, not all SM processes are available in this specific format making it impossible to compare the total number of events in simulation and real data. This, however, does not constitute a serious problem since this analysis will finally use data-based background estimation methods. The simulated SM datasets can still be used to compare the shapes of important distributions in simulation and data.[1] Still, the most important SM background sample including W + jets events is available. Due to the intrinsic missing energy in W + jets events and the additional lepton that can fail reconstruction (see Section **??** for further details on the backgrounds) it constitutes the major background to the presented search.

In Table **??** all available SM samples used in this analysis are listed. The matrix-elements of the W + jets, $t\bar{t}$ + jets and $Z \to \ell\bar{\ell}$ + jets samples are generated using MADGRAPH 5 [**?**]. For the QCD sample PYTHIA6 [**?**] is used for generation. All samples are then passed to PYTHIA 6 to simulate the hadronisation and the showering. The interactions between the particles and the detector material is simulated using GEANT4 [**?**, **?**].

Due to the size of the samples (between 5 and 70 TB per sample) a reduction is required in order to limit the storage space requirements. This is achieved by selecting only events

---

[1]For example, the simulated $Z \to \nu\bar{\nu}$ + jets sample that can contribute to the background of this search via fake tracks is not available in RECO format. However, as the shape of important observables of fake tracks is independent of the underlying process, this background can be studied with a simulated W + jets sample.

Table 4.1: Available Standard Model background samples containing $\Delta E/\Delta x$ information that are used for background estimation studies.

Process	Generator	Cross section [pb]	$\mathcal{O}_{\text{calculation}}^{\text{cross section}}$
$W + \text{jets}$	MADGRAPH 5	36703.2	NNLO [?]
$t\bar{t} + \text{jets}$	MADGRAPH 5	245.8	NNLO [?]
$Z \to \ell\bar{\ell} + \text{jets} \ (\ell = e, \mu, \tau)$	MADGRAPH 5	3531.9	NNLO [?]
QCD $(50\,\text{GeV} < \hat{p}_{\text{T}} < 1400\,\text{GeV})$	PYTHIA 6	9374794.2	LO

which contain at least one jet with a minimum transverse momentum of $p_{\text{T}} > 60\,\text{GeV}$.

In addition, further simulated samples not containing the energy information are used (so-called AOD samples). Because of their much smaller size, these samples are available in full size. They are needed to study the background inclusively in the variable dE/dx.

4.2 Signal samples

For the investigation of a possible SUSY signal, events containing either chargino pair production $q\bar{q} \to \tilde{\chi}_1^{\pm}\tilde{\chi}_1^{\mp}$ or chargino neutralino production $q\bar{q} \to \tilde{\chi}_1^{\pm}\tilde{\chi}_1^0$ are simulated within this thesis. The simulation of the samples is done as described in Section ?? for the $W + \text{jets}$ sample. However, a special treatment for long-lived particles is required for this analysis. In order to get a correct detector simulation of the energy loss of long-lived particles that decay after the beam pipe, the decay of the chargino cannot be simulated within MADGRAPH or PYTHIA but needs to be simulated within GEANT4. The decay mode of the chargino is also specified within GEANT4 to a neutralino plus pion decay, $\tilde{\chi}_1^{\pm} \to \tilde{\chi}_1^0 \pi^{\pm}$.

To reduce the required computing sources, the simulation is only done for a few lifetimes $(1\,\text{cm},\ 5\,\text{cm},\ 10\,\text{cm},\ 50\,\text{cm},\ 100\,\text{cm},\ 1\,000\,\text{cm}$ and $10\,000\,\text{cm})$. The lifetime is hereby not controlled by changing the mass gap between the chargino and the neutralino but is independently specified within GEANT4. In order to scan in a high resolution over the lifetime space, other lifetimes are generated using lifetime reweighting. The weight for each event depends on the individual proper lifetime of the chargino and is given by

$$w = \prod_{i=1}^{n} \frac{\tau^{\text{gen}}}{\tau^{\text{target}}} \cdot \exp\left[t_i \cdot \left(\frac{1}{\tau^{\text{gen}}} - \frac{1}{\tau^{\text{target}}} \right) \right],$$
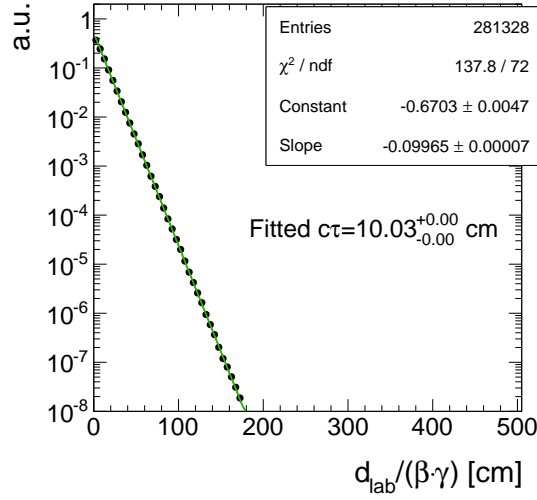
Figure 4.1: Normalised distribution of the proper individual lifetime $d_{\text{lab}}/\left(\beta\gamma\right)$ of all charginos contained in a signal sample with a generated lifetime of $c\tau^{\text{gen}} = 50\,\text{cm}$ reweighted to a lifetime of $c\tau^{\text{target}} = 10\,\text{cm}$. Fitting an exponential curve $a \cdot \exp\left[\frac{1}{c\tau}ct_i\right]$ yields $c\tau = 1./\text{Slope} = 10\,\text{cm}$.

where n is the number of charginos in the event, τ^{gen} is the generated mean lifetime in the particle's rest frame and t_i is the individual proper lifetime of the chargino. The targeted mean lifetime is given by τ^{target}. A derivation of this formula can be found in Appendix A.1. Using this reweighting procedure a good coverage of the lifetime space can be achieved with lifetimes of $1\,\text{cm} \leq c\tau \leq 10^4\,\text{cm}$. Figure **??** shows the exponential distribution of the individual proper lifetime of the charginos after the reweighting of a simulated sample with $c\tau^{\text{gen}} = 50\,\text{cm}$ to a lifetime of $c\tau^{\text{target}} = 10\,\text{cm}$. It can be seen that the reweighting procedure does indeed reproduce the targeted lifetime of $10\,\text{cm}$.

All samples are generated for different masses of the chargino, but always almost mass-degenerate to the lightest neutralino. The mass gap between chargino and neutralino is set to $150\,\text{MeV}$ and, as said before, is hereby disentangled to the chargino lifetime for the simulation of the signal samples. However, since this analysis does not make use of the decay products of the chargino and the mass gap is for all simulated lifetimes of a similar small size, the choice of the mass gap does not affect the signal prediction. Six different masses from $100\,\text{GeV}$ to $600\,\text{GeV}$ are simulated. This leads to a total number of 42 signal samples. In Table **??** cross sections at $\sqrt{s} = 8\,\text{TeV}$ for $\tilde{\chi}_1^{\pm}\tilde{\chi}_1^{\mp}$ and $\tilde{\chi}_1^{\pm}\tilde{\chi}_1^{0}$ production for wino-like charginos and neutralinos are listed [**?**, **?**]. The cross section does not depend on the lifetime of the chargino.

Table 4.2: Simulated signal mass points with corresponding cross sections at NLO-NLL (NLO: next-to-leading order, NLL: next-to-leading logarithmic) accuracy for wino-like charginos.

$m_{\tilde{\chi}_1^\pm}\,[\,\mathrm{GeV}]$	$\sigma_{\tilde{\chi}_1^\pm \tilde{\chi}_1^\mp}\,[\,\mathrm{pb}]$	$\sigma_{\tilde{\chi}_1^0 \tilde{\chi}_1^\mp}\,[\,\mathrm{pb}]$
100	5.8234	11.5132
200	0.37924	0.77661
300	0.06751	0.14176
400	0.01751	0.03758
500	0.00553	0.01205
600	0.00196	0.00431

5 Event selection

5.1 Datasets and triggers

The analysis is performed on pp collision data recorded in the year 2012 by the CMS experiment at a centre-of-mass energy of $\sqrt{s} = 8\,\text{TeV}$. In total an integrated luminosity of $19.7\,\text{fb}^{-1}$ was recorded in 2012.

As outlined in Section 2, the detection of chargino tracks is a challenging task already on trigger level. Direct triggering of events containing chargino-like tracks is not possible because in 2012 there was no dedicated track trigger available. Furthermore, there is no intrinsic missing transverse energy in the event if the chargino is not reconstructed as a PF particle, e. g. when it decays inside the tracker. Therefore, this analysis uses initial state radiation for the detection of chargino events. If ISR occurs, it is possible to trigger on a high-p_{T} jet ($p_{\text{T}}^{1^{\text{st}}\,\text{jet}}$) and missing transverse momentum ($\not{E}_{\text{T}}$).

For this purpose, several triggers are utilised in this analysis. An event is selected, if at least one of the three triggers in Table **??** fired.

Table 5.1: $\not{E}_{\text{T}}$ and $\not{E}_{\text{T}}$ + jet triggers used in this analysis together with the corresponding recorded integrated luminosity during the time when they were in place.

Trigger	Integrated luminosity $[\,\text{fb}^{-1}\,]$
HLTMonoCentralPFJet80_PFMETnoMu95_NHEF0p95	5.3
HLTMonoCentralPFJet80_PFMETnoMu105_NHEF0p95	14.4
HLT_MET120_HBHENoiseCleaned	19.7

The HLTMonoCentralPFJet80_PFMETnoMu95_NHEF0p95 and HLTMonoCentralPF-Jet80_PFMETnoMu105_NHEF0p95 triggers both rely on the L1 ETM40 trigger which requires the missing energy to be larger than $40\,\text{GeV}$. On HLT level, they further require at least one particle-flow jet within the pseudorapidity range of $|\eta| < 2.6$ with $p_{\text{T}} > 80\,\text{GeV}$ and the PF missing transverse momentum (not taking into account the p_{T} of muons) to be larger than $95\,\text{GeV}$ or $105\,\text{GeV}$ respectively. Finally, no more than

95% of the jet energy must be carried by neutral hadrons. The HLTMonoCentralPF-Jet80_PFMETnoMu95_NHEF0p95 trigger was active during Run A and Run B in 2012 data taking, whereas HLTMonoCentralPFJet80_PFMETnoMu105_NHEF0p95 was in place during Run C and Run D in 2012.

The HLT_MET120_HBHENoiseCleaned trigger is based on the L1 trigger ETM36. On HLT level, the trigger requires that the missing energy measured from calorimeter energy deposits only is larger than 120 GeV. The HBHENoise-filter reduces background from electronic noise in the HCAL.

The events that were selected by the described triggers are available in the MET datasets listed in Table **??**. Again, because of the size of the datasets (~ 150 TB in total), a re-

Table 5.2: MET data samples used in the search with the contained integrated luminosity.

Dataset	Integrated luminosity $[\,\mathrm{fb}^{-1}\,]$
/MET/Run2012A-22Jan2013-v1/RECO	0.876
/MET/Run2012B-22Jan2013-v1/RECO	4.412
/MET/Run2012C-22Jan2013-v1/RECO	7.055
/METParked/Run2012D-22Jan2013-v1/RECO	7.354

duction of the size is achieved by selecting only events where one of the used triggers fired and that contain at least one jet with a minimum p_T of 50 GeV.

5.2 Selection of signal candidate events

In order to suppress events originating from Standard Model processes such as QCD-multijet events, $W + $ jets, etc., a selection favouring signal-like tracks is applied. The signal candidate selection closely follows the selection required in the disappearing track search [29, 30]. It relies on event-based and track-based variables as described in the following two sections.

5.2.1 Event-based selection

First a selection on the quality of the primary vertex is applied in order to suppress cosmic events and noise from the beam halo. This selection includes requirements on the position

of the vertex with respect to the beam axes and the number of degrees of freedom of the vertex [**?**]

- ❖ The vertex must have at least four degrees of freedom: *vtx* with ≥ 4 d.o.f.

- ❖ The position of the vertex along the beam line must be within $24\,\text{cm}$ with respect to the nominal interaction point: $|dz| \leq 24\,\text{cm}$.

- ❖ The position in the transverse direction must be within $2\,\text{cm}$ with respect to the nominal interaction point: $|d0| \leq 2\,\text{cm}$.

To maximise the signal acceptance, the trigger related selection cuts are chosen close to the trigger thresholds (see Section **??**). In Fig. **??**, the distributions of $\not{E}_\text{T}$ and the transverse momentum of the leading jet, $p_\text{T}^{1^\text{st}\,\text{jet}}$, are shown for different signal models. The leading jet has to be centrally produced, $|\eta_{1^\text{st}\text{jet}}| < 2.4$, and to fulfil the following criteria:

- Charged hadron energy fraction $(\text{CHF}_{1^\text{st}\text{jet}}) > 0.2$

- Charged electromagnetic energy fraction $(\text{CEF}_{1^\text{st}\text{jet}}) < 0.5$

- Neutral hadron energy fraction $(\text{NHF}_{1^\text{st}\text{jet}}) < 0.7$

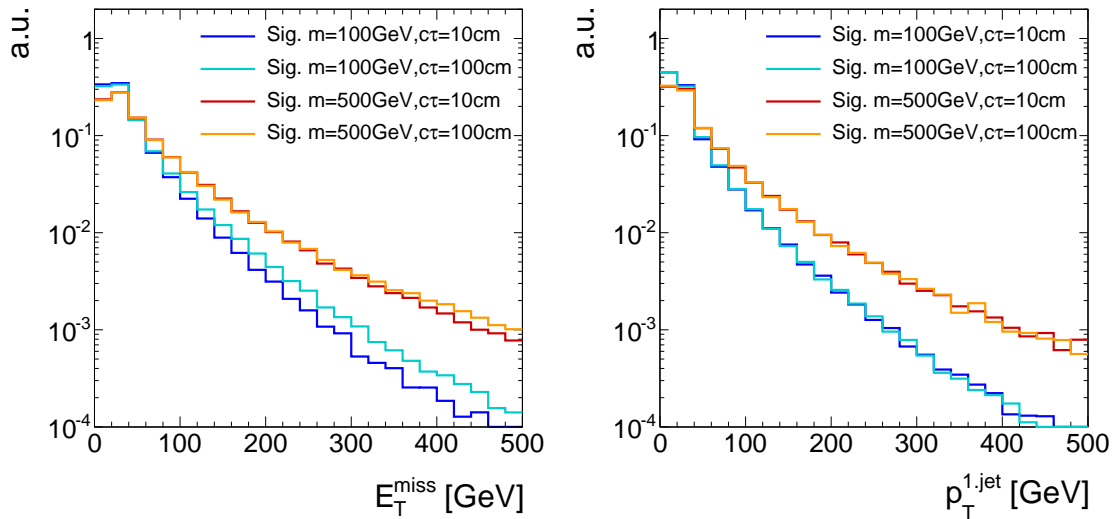- Neutral electromagnetic energy fraction $(\text{NEF}_{1^\text{st}\text{jet}}) < 0.7$.

Figure 5.1: Normalised distributions of the missing transverse momentum (left) and the transverse momentum of the leading jet (right) for four different signal models.

These additional jet quality criteria ensure that noise from cosmic and beam halo muons and high-p_T photons and electrons is suppressed [**?**].

The trigger efficiency as a function of $\not{E}_T$ and $p_T^{1^{st}\,jet}$ was determined within [**?**] with a single-muon reference sample. The trigger paths become fully efficient for $p_T^{1^{st}\,jet} \gtrsim$ 110 GeV and $\not{E}_T \gtrsim 220$ GeV [**?**]. However, it can be seen in Fig. **??** that for a selection of $\not{E}_T > 220$ GeV more than 99% of the signal events are rejected.

In order to achieve a reasonable signal acceptance, this search imposes, therefore, a trigger selection closer to the intrinsic trigger thresholds. The trigger requirements are as follows:

❖ There is at least one jet within $|\eta| < 2.4$ with transverse momentum larger than 110 GeV which fulfils the above mentioned jet noise cleaning criteria: $p_T^{1^{st}\,jet} > 110$ GeV.

❖ The missing transverse momentum must be larger than 100 GeV: $\not{E}_T > 100$ GeV

These requirements result in a trigger efficiency of 100% related to the trigger jet p_T requirement and $\sim 5-20\%$ in the trigger $\not{E}_T$ requirement at the cut thresholds [**?**]. Throughout the following sections, these trigger related requirements will be referred to as "trigger selection".

Because of the huge cross section, QCD-multijet events are frequently produced at the LHC. Due to jet energy mismeasurements, they can also contribute to data samples recorded with MET triggers. Therefore, special requirements are enforced in order to suppress events emerging from QCD-multijet processes. QCD-multijet events can be characterised by topologies where two jets are almost back-to back. Additionally, in QCD-multijet events the missing energy is usually aligned with one of the leading jets in the event. Figure **??** shows the maximum $\Delta\phi$ of any of two jets and the minimum $\Delta\phi$ between the $\not{E}_T$ vector and any of the two leading jets for the SM background and two different signal datasets.

The following two requirements are sufficient to suppress QCD-multijet events efficiently:

❖ $\Delta\phi$ between any of two jets (with $p_T > 20$ GeV and $|\eta| < 4.5$) in the event must be smaller than 2.5.

❖ $\Delta\phi$ between any of the two leading jets (with $p_T > 20$ GeV and $|\eta| < 4.5$) and the $\not{E}_T$ must be larger than 0.5.

5.2.2 Candidate track selection

After the reduction of background processes with event-based variables, a track-based selection is carried out. To get an optimised selection for possible chargino tracks several
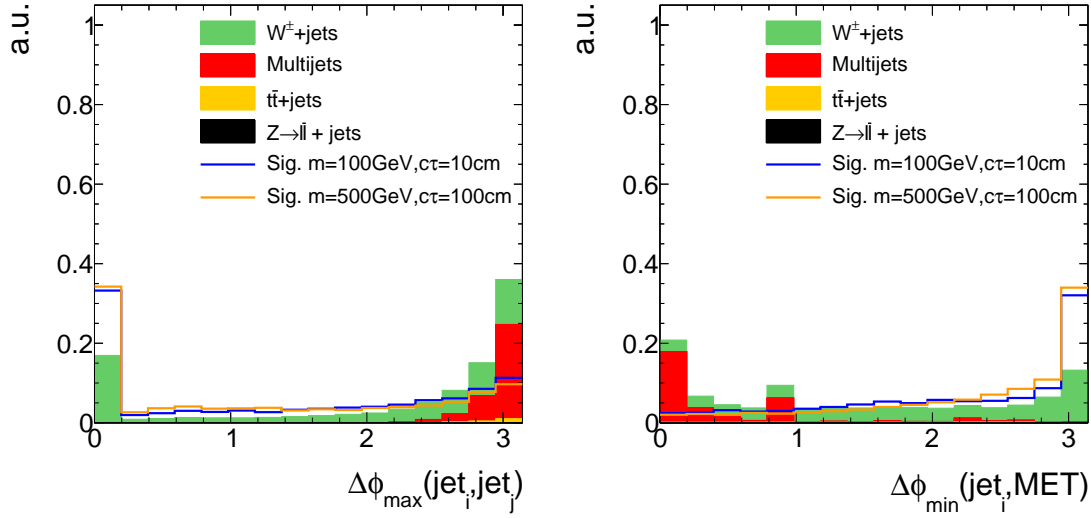
Figure 5.2: Maximum $\Delta\phi$ between any of two jets (left) and the minimum $\Delta\phi$ between the $\slashed{E}_{\mathrm{T}}$ vector and any of the two leading jets (right) normalised to unit area after trigger selection. Only jets with $p_{\mathrm{T}} > 20\,\mathrm{GeV}$ and $|\eta| < 4.5$ are considered.

signal candidate track characteristics are exploited.

First, a selection of high-quality tracks is enforced:

- ❖ The track must be classified as "high purity" as defined in [27].

- ❖ The track is required to have no missing middle or inner hits: $N_{\mathrm{miss}}^{\mathrm{middle/inner}} = 0$

- ❖ The radial and longitudinal distance of the track to the primary vertex must be small: $|d0| < 0.02\,\mathrm{cm}$, $|dz| < 0.5\,\mathrm{cm}$.

In Figs. **??** and **??**, the power of the latter two quality selection cuts is shown.

Furthermore, a first kinematic preselection is applied:

- ❖ Only tracks in the central region are considered : $|\eta| < 2.1$.

- ❖ Only tracks with a minimum transverse momentum of $20\,\mathrm{GeV}$ are considered: $p_{\mathrm{T}} > 20\,\mathrm{GeV}$.

In order to suppress background tracks emerging from SM processes, an electron, muon and tau veto is applied. This rejects tracks that are close to a reconstructed electron, muon or tau. Additionally, the candidate track must not be close to a jet ($p_{\mathrm{T}} > 20\,\mathrm{GeV}$ and $|\eta| < 4.5$):
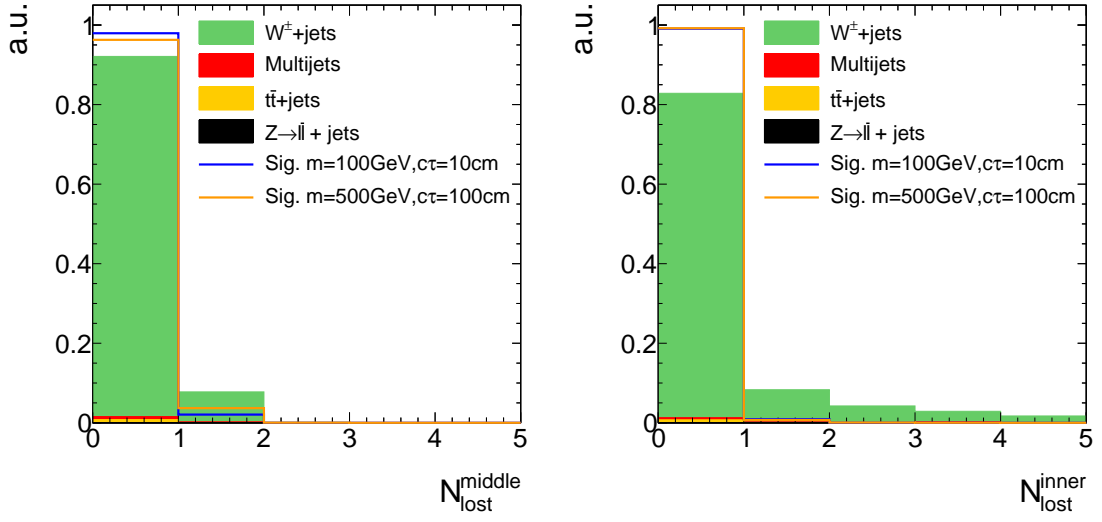
Figure 5.3: Normalised number of missing middle (left) and inner (right) hits of background and signal tracks after trigger selection and QCD suppression cuts.
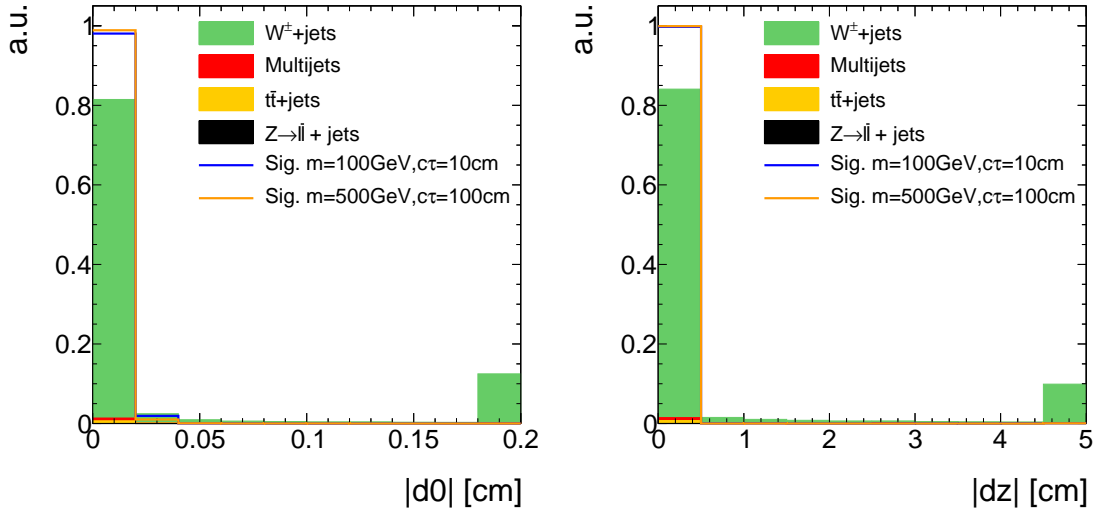
Figure 5.4: Absolute value of the radial (left) and longitudinal (right) distance between the track and the primary vertex after trigger selection and QCD-multijet suppression cuts. All events with a candidate track with a radial (longitudinal) distance larger than 0.2 cm (5 cm) are contained in the last bin.

❖ The track must not be within a cone of $\Delta R < 0.15$ to a reconstructed standalone, tracker or global muon with a transverse momentum larger than 10 GeV (see Section ?? for details on the different muon definitions).

❖ The track must not be within a cone of $\Delta R < 0.15$ to a reconstructed electron with a transverse momentum larger than $10\,\text{GeV}$ (see Section **??** for details on the electron reconstruction).

❖ The track must not be within a cone of $\Delta R < 0.15$ to a reconstructed tau with $p_\text{T} > 20\,\text{GeV}$ and $|\eta| < 2.3$ (see Section **??** for details on the tau reconstruction). Some loose isolation requirements are enforced to protect the tau reconstruction from jet contamination.

❖ The track must not be within a cone of $\Delta R < 0.5$ to a reconstructed jet ($p_\text{T} > 20\,\text{GeV}$ and $|\eta| < 4.5$).

These lepton and jet veto selection requirements are of course highly suppressing the background emerging from real lepton/jet production like in $W + $ jets events. The discrimination power of the lepton and jet vetos is shown in Fig. **??** where the minimum ΔR between the candidate track and a reconstructed electron, muon, tau or jet is shown.

Unfortunately, the lepton veto selection cuts lack efficiency in some of the detector directions. For example, the reconstruction of an electron easily fails in the direction of a dead ECAL cell. This reduces the discrimination power of the electron veto. For this reason, tracks that point towards dead or noisy ECAL cells are rejected. A general list of dead and noisy ECAL cells is provided centrally at CMS. Further dead cells were identified within a study in [29,30] resulting in a total number of 1234 dead or noisy ECAL channels. These are illustrated in Fig. **??** showing a map of all ECAL channels not considered in the search.

Additionally, tracks that point towards intermodule gaps of ECAL cells or to the ECAL barrel endcap gap at $1.42 < |\eta| < 1.65$ are rejected. A list of the ECAL intermodule gaps, that is supplied centrally at CMS, is given in Table **??**.

The muon reconstruction is less efficient for muons in detector regions with bad cathode strip chambers (CSC). These bad chambers are also identified centrally at CMS and their η and ϕ values are visualised in Fig. **??**. Thus, also tracks pointing towards these regions within a distance of $\Delta R < 0.25$ are rejected.

To summarise, tracks pointing towards detector regions, that are not working properly or where the lepton reconstruction efficiencies are reduced, are vetoed as follows:

❖ Veto tracks within a cone of $\Delta R < 0.05$ to a dead or noisy ECAL cell (visualised in Fig. **??**).

❖ Veto tracks that point towards the direction of the ECAL intermodule gap listed in Table **??**.
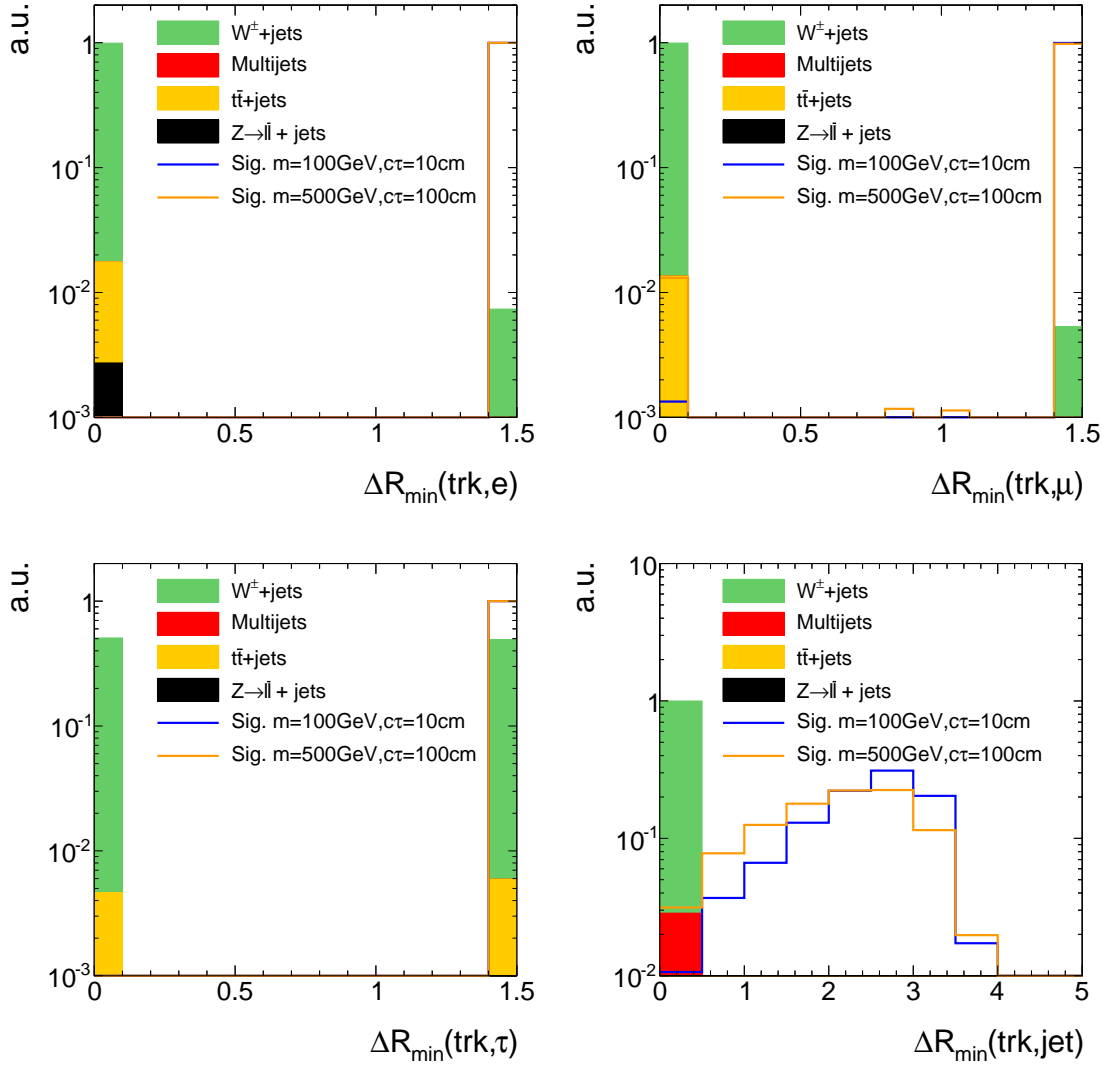
Figure 5.5: The minimum ΔR between the candidate track and a reconstructed electron (top left), muon (top right), tau (bottom left) or jet (bottom right) after the full candidate track selection cuts but without the one shown in the corresponding plot ("N-1 plot"). The last bin contains all events where the candidate track has a $\Delta R_{\min}$ larger than 1.5 or 5.0 to the next lepton or jet respectively. Events with no respective lepton or jet are all contained in the last bin.

❖ Veto tracks that point towards a bad CSC within $\Delta R < 0.25$ (visualised in Fig. **??**).

❖ Veto tracks that point towards the region between ECAL barrel and endcap at $1.42 < |\eta| < 1.65$

Finally, two further characteristics of chargino tracks are exploited. As the chargino is produced in a very clean environment (no further track activity around the chargino is
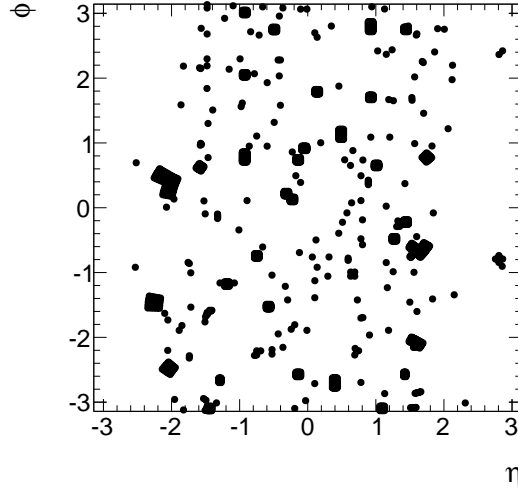
Figure 5.6: Visualisation of dead and noisy ECAL cells in the detector's $\phi - \eta$ plane according to [29,30]. The radius of the dots correspond to $\Delta R = 0.05$.

expected), the isolation of the track can discriminate signal against background events.

Furthermore, for charginos decaying inside the tracker there is no associated energy deposition in the calorimeters in the direction of the track. This is a very pronounced characteristics of signal tracks.

The resulting selection cuts are as follows

❖ No further substantial track activity is allowed in a cone of $\Delta R < 0.3$ around the

Table 5.3: Intermodule ECAL gaps.

η-ranges
-1.14018 < η < -1.1439
-0.791884 < η < -0.796051
-0.44356 < η < -0.447911
0.00238527 < η < -0.00330793
0.446183 < η < 0.441949
0.793955 < η < 0.789963
1.14164 < η < 1.13812
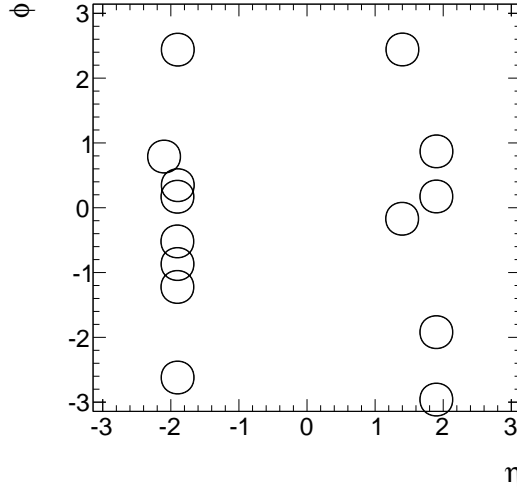
Figure 5.7: Visualisation of the excluded region by the bad cathode strip chamber veto in the detector's $\phi - \eta$.

candidate track: $\sum_{\Delta R < 0.3} p_{\mathrm{T}}^{\mathrm{trk}}/p_{\mathrm{T}}^{\mathrm{cand}} - 1 < 0.1$

❖ Little calorimeter energy deposits (ECAL+HCAL) in a cone of $\Delta R < 0.5$ around the track: $E_{\mathrm{calo}}^{\Delta R < 0.5} < 5\,\mathrm{GeV}$.

The discrimination power of these two variables is shown in Fig. **??**.

As emphasised before, this analysis aims at being sensitive especially on shorter lifetimes. Still, in order to allow for charginos decaying at any layer of the tracker, no explicit selection cut on the number of missing outer hits is required.

Events are selected if they at least contain one track fulfilling all candidate track selection requirements. An overview over the full analysis preselection is given in Table **??**. The event yields after the selections of each of the categories from Table **??** are listed in Table **??** for the simulated background samples, some exemplary simulated signal models and for observed data. Detailed event yield tables can be found in Appendix A.2.

Given the presented signal candidate selection, two variables remain that are highly discriminating: The transverse momentum p_{T} and the energy release per path length dE/dx of the candidate track. In this analysis, the Asymmetric Smirnov discriminator I_{as} is used to enhance the discriminating power of dE/dx. See Section 3.3 for the definition and a detailed explanation of I_{as}.

In Fig. **??**, the distribution of the remaining two variables are shown after the selection of signal candidate events. These variables are used to optimise the sensitivity of the
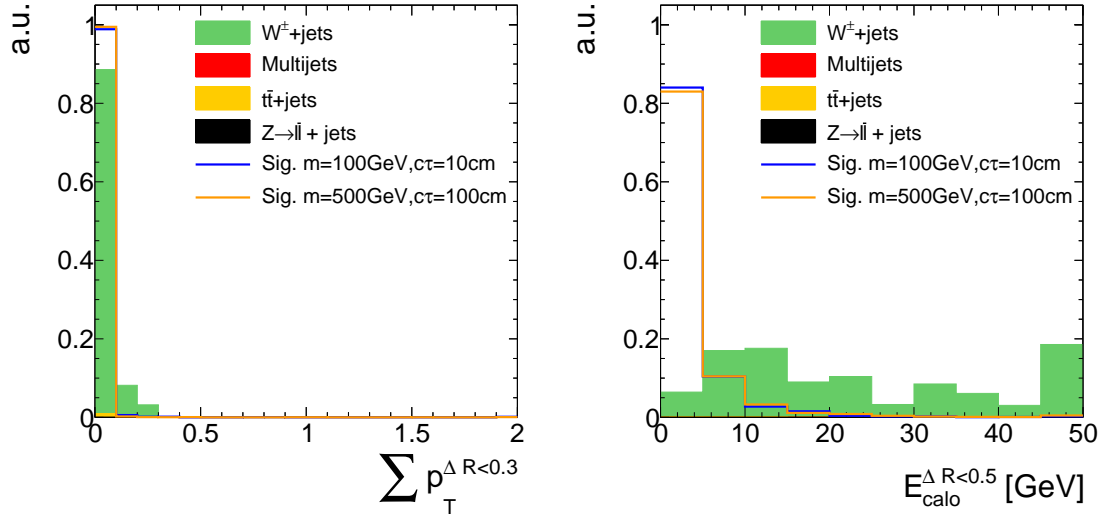
Figure 5.8: Track isolation (left) and calorimeter energy deposits (right) of the candidate track after the full previous selection. All events with a track isolation or a calorimeter energy deposit larger than the range shown in the figures are contained in the last bin.
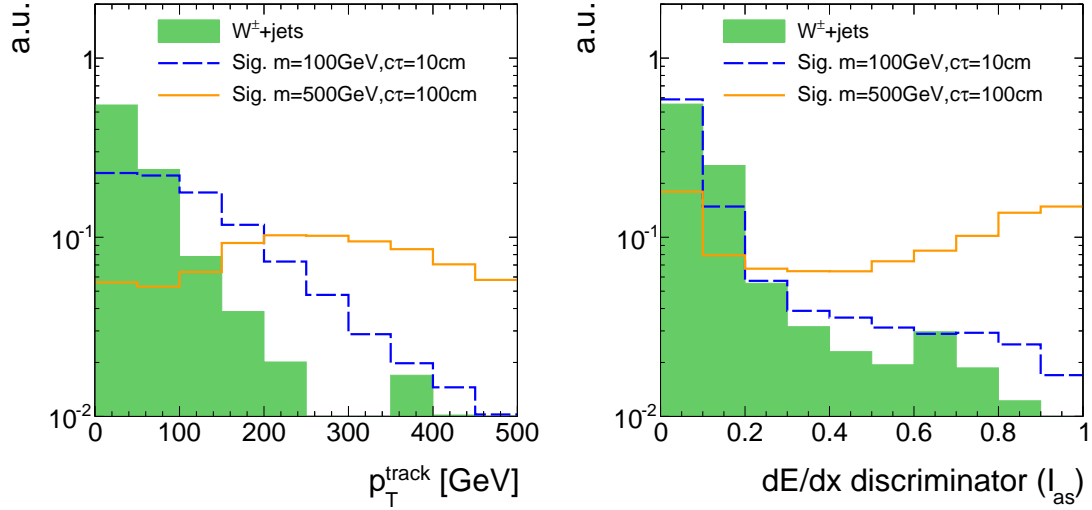
Figure 5.9: Candidate track p_{T} (left) and I_{as} (right) after the full signal candidate selection for signal and W + jets events. Because of the low statistical precision of the W + jets sample, the trigger selection is not applied.

search. The optimisation process will be explained in Section **??**. However, before the optimisation can be accomplished, a characterisation and estimation of the background is needed. This topic will be discussed in the following section.

Table 5.4: Summary and categorisation of the analysis selection.

Trigger	HLTMonoCentralPFJet80_PFMETnoMu95_NHEF0p95 HLTMonoCentralPFJet80_PFMETnoMu105_NHEF0p95 HLT_MET120_HBHENoiseCleaned	
Event-based selection	Trigger selection	$p_{\mathrm{T}}^{1^{\mathrm{st}}\,\mathrm{jet}} > 100\,\mathrm{GeV}$ with $\lvert\eta_{1^{\mathrm{st}}\mathrm{jet}}\rvert < 2.4$, $\mathrm{CHF}_{1^{\mathrm{st}}\mathrm{jet}} > 0.2$, $\mathrm{CEF}_{1^{\mathrm{st}}\mathrm{jet}} < 0.5$, $\mathrm{NHF}_{1^{\mathrm{st}}\mathrm{jet}} < 0.7$, $\mathrm{NEF}_{1^{\mathrm{st}}\mathrm{jet}} < 0.7$ $\not{E}_{\mathrm{T}} > 100\,\mathrm{GeV}$
	QCD suppression	$\Delta\phi_{\mathrm{max}}\left(\mathrm{jet}_i,\mathrm{jet}_j\right) < 2.7$ for all jets with $p_{\mathrm{T}} > 20\,\mathrm{GeV}$, $\lvert\eta\rvert < 4.5$ $\Delta\phi_{\mathrm{max}}\left(\mathrm{jet}_i,\not{E}_{\mathrm{T}}\right) > 0.5$ for two leading jets
Candidate track selection	≥ 1 track that fulfils the following criteria:	
	Good quality selection	high-purity as defined in [27] $N_{\mathrm{miss}}^{\mathrm{middle/inner}} = 0$ $\lvert d0\rvert < 0.02\,\mathrm{cm}$ $\lvert dz\rvert < 0.5\,\mathrm{cm}$
	Kinematic selection	$\lvert\eta\rvert < 2.1$ $p_{\mathrm{T}} > 20\,\mathrm{GeV}$
	Lepton/jet veto	No muon within $\Delta R < 0.15$ No electron within $\Delta R < 0.15$ No tau within $\Delta R < 0.15$ No jet within $\Delta R < 0.5$ No dead/noisy ECAL cell within $\Delta R < 0.05$ Not within an ECAL intermodule gap Not within $1.42 < \lvert\eta\rvert < 1.65$ Not within $\Delta R < 0.25$ to a bad CSC
	Isolation selection	$\sum\limits_{\Delta R < 0.3} p_{\mathrm{T}}^{\mathrm{trk}}/p_{\mathrm{T}}^{\mathrm{cand}} - 1 < 0.1$ $E_{\mathrm{calo}}^{\Delta R < 0.5} < 5\,\mathrm{GeV}$

Table 5.5: Event yields in simulation and observed data after the selections of each of the categories from Table **??**

Selection	Simulated background samples				Simulated signal samples				Data
	$W + \text{jets}$	$t\bar{t} + \text{jets}$	$Z \to \ell\bar{\ell}$	Multijet	m=100GeV $c\tau$=10cm	m=100GeV $c\tau$=100cm	m=500GeV $c\tau$=10cm	m=500GeV $c\tau$=100cm	MET data
After skim	$9.16 \cdot 10^7$	$1.04 \cdot 10^6$	$2.21 \cdot 10^7$	$1.38 \cdot 10^{11}$	$3.41 \cdot 10^5$	$3.41 \cdot 10^5$	$3.46 \cdot 10^2$	$3.46 \cdot 10^2$	$1.07 \cdot 10^7$
Event-based selection:									
Trigger	$4.31 \cdot 10^6$	$1.15 \cdot 10^5$	$4.23 \cdot 10^3$	$4.32 \cdot 10^6$	$1.55 \cdot 10^4$	$1.49 \cdot 10^4$	$4.62 \cdot 10^1$	$4.62 \cdot 10^1$	$1.07 \cdot 10^7$
Trigger selection	$1.89 \cdot 10^6$	$5.31 \cdot 10^4$	$6.26 \cdot 10^2$	$9.63 \cdot 10^5$	$1.09 \cdot 10^4$	$9.83 \cdot 10^3$	$3.63 \cdot 10^1$	$3.57 \cdot 10^1$	$3.94 \cdot 10^6$
QCD suppression	$1.11 \cdot 10^6$	$6.76 \cdot 10^3$	$1.32 \cdot 10^2$	$9.55 \cdot 10^3$	$7.90 \cdot 10^3$	$6.98 \cdot 10^3$	$2.76 \cdot 10^1$	$2.71 \cdot 10^1$	$1.38 \cdot 10^6$
Track-based selection:									
Good quality selection	$1.07 \cdot 10^6$	$6.63 \cdot 10^3$	$1.32 \cdot 10^2$	$9.55 \cdot 10^3$	$2.80 \cdot 10^3$	$5.38 \cdot 10^3$	$5.07 \cdot 10^0$	$2.00 \cdot 10^1$	$1.30 \cdot 10^6$
Kinematic selection	$8.14 \cdot 10^5$	$5.63 \cdot 10^3$	$1.32 \cdot 10^2$	$5.48 \cdot 10^3$	$2.54 \cdot 10^3$	$4.93 \cdot 10^3$	$4.73 \cdot 10^0$	$1.89 \cdot 10^1$	$9.51 \cdot 10^5$
Lepton/jet veto	$5.02 \cdot 10^2$	$5.88 \cdot 10^0$	$0 \cdot 10^0$	$0 \cdot 10^0$	$1.99 \cdot 10^3$	$3.67 \cdot 10^3$	$3.83 \cdot 10^0$	$1.50 \cdot 10^1$	$6.16 \cdot 10^2$
Isolation selection	$3.19 \cdot 10^1$	$0.67 \cdot 10^0$	$0 \cdot 10^0$	$0 \cdot 10^0$	$1.67 \cdot 10^3$	$3.04 \cdot 10^3$	$3.39 \cdot 10^0$	$1.26 \cdot 10^1$	$1.19 \cdot 10^2$

6 Characterisation and estimation of the Standard Model backgrounds

After the application of the signal candidate selection, explained in the previous section, the background arising from Standard Model processes is dramatically reduced. Only two events in the simulated $W + $ jets sample remain. One of these originates from an unreconstructed muon, the other one from an unreconstructed electron. This implies, that the electron, muon, and tau vetos cannot reject all leptons because some are not properly reconstructed. Due to the limited size of the simulated $W + $ jets dataset (15 times smaller than the number of events expected from $W + $ jets processes during 2012 data taking), it is not possible to rely on a full simulation-based estimation of the leptonic background. The underlying mechanism of the non-reconstruction of a lepton and the corresponding methods to estimate the leptonic background will be explained in detail in Section **??**.

Furthermore, there is the possibility that a track is reconstructed out of a set of hits that do not origin from only one single particle. Such tracks are called "fake tracks". Background tracks arising from a combination of unrelated hits will be explained in the following Section **??**. It should be noted that the fake background is contributing through all SM processes, not only via $W + $ jets. Still, as the characteristics of fake tracks are independent of the underlying process, this background can also be studied on simulation using $W + $ jets events only.

6.1 Fake background

Fake tracks are tracks that are not reconstructed out of the trajectory of one single particle. The rate at which this wrong reconstruction occurs is highly restrained by the quality cuts on χ^2 and the vertex compatibility of the track reconstruction algorithm. Details on the reconstruction algorithm of tracks at CMS can be found in Section **??**.

The probability that a reconstructed track is actually a fake is strongly correlated with the number of hits of the track. This can be seen in Fig. **??**, where the normalised distribution of the number of hits from fake tracks is depicted. There are almost no fakes with more than seven hits. In simulation, fake tracks are defined as tracks that cannot be matched to a generator-level particle within a distance of $\Delta R < 0.01$.

Fakes are efficiently suppressed by the requirements of no missing middle or inner hits

and the compatibility with the primary vertex. Unfortunately, wrongly reconstructed tracks which pass these criteria, do also easily pass the $E_{\text{calo}}^{\Delta R < 0.5} < 5\,\text{GeV}$ requirement with high efficiency.

In this analysis, the estimation of the fake background is split into two parts. First, the background is determined inclusively in dE/dx. Second, the dE/dx (I_{as}) distribution is estimated with the help of a fake enriched control region. This second step is needed to enable an optimisation in dE/dx (see Section **??**).

6.1.1 Inclusive fake background estimation

The inclusive background estimation closely follows the background estimation method done in [29, 30]. It aims at determining the probability of having a fake track in an event that passes the full signal candidate selection (Table **??**) plus a potential additional p_{T} selection cut that is determined in an optimisation procedure (Section **??**). This probability will be called the fake rate ρ_{fake}. Within [29, 30], it was checked that the fake rate is constant for different processes. Thus, it is possible to determine ρ_{fake} with the help of one SM process and then generalise it to all SM background Wprocesses.

The inclusive fake background is estimated with the help of $Z \to \mu\bar{\mu}$ and $Z \to e\bar{e}$ events from data. $Z \to \ell\bar{\ell}$ events can be selected with high purity by requiring two well reconstructed muons or electrons that are opposite in charge and for which the invariant mass is around the Z-boson mass of $\sim 90\,\text{GeV}$. As these events do not contain further
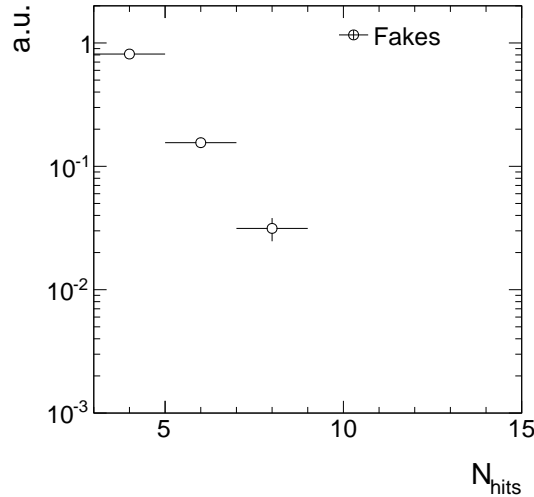

Figure 6.1: Normalised distribution of the number of hits for fake tracks. To increase the statistical precision, only the candidate track selection from Table **??** is applied.

leptons from the hard interaction, any additional track is either a constituent of an ISR jet, a soft particle from the underlying event or is a fake, reconstructed out of a combination of hits from several soft particles. Since the candidate track selection requires a track with a $p_\mathrm{T} > 20\,\mathrm{GeV}$ that is no lepton or jet, it suppresses ISR jets and soft tracks from the underlying event. Thus, applying the track-based signal candidate selection on $Z \to \ell\bar\ell$ events selects fake tracks with high purity.

The selection of two well reconstructed muons and electrons is done with the single-muon and single-electron datasets listed in Table **??**. These datasets contain at least one

Table 6.1: Datasets used for the determination of the fake rate.

Dataset	Integrated luminosity $[\,\mathrm{fb}^{-1}\,]$
/SingleMu/Run2012A-22Jan2013-v1/AOD	0.876
/SingleMu/Run2012B-22Jan2013-v1/AOD	4.405
/SingleMu/Run2012C-22Jan2013-v1/AOD	7.040
/SingleMu/Run2012D-22Jan2013-v1/AOD	7.369
/SingleElectron/Run2012A-22Jan2013-v1/AOD	0.876
/SingleElectron/Run2012B-22Jan2013-v1/AOD	4.412
/SingleElectron/Run2012C-22Jan2013-v1/AOD	7.050
/SingleElectron/Run2012D-22Jan2013-v1/AOD	7.368

muon or one electron in every event. For the $Z \to \mu\bar\mu$ selection, an event is required to have two muons with $p_\mathrm{T} > 25\,\mathrm{GeV}$ and $|\eta| < 2.4$. To suppress background from cosmic muons, the distance from the primary vertex must be less than $|d0| < 0.2\,\mathrm{cm}$ in radial and $|dz| < 0.5\,\mathrm{cm}$ in longitudinal direction. In order to suppress background arising from jets that fake muons, various quality criteria are applied: it is required that there is at least one hit in the muon detector that is considered in the global muon fit, and that at least two measurements are from different muon detector stations. Concerning the track of the muon in the tracker system, at least six hits in the full tracker system of which at least one pixel hit is required. An isolation criterion is applied that requires the sum of transverse momenta of all particle-flow particles in a cone of $\Delta R < 0.4$ around the muon to be less than 12% of the muon p_T. Finally, the muons are required to be opposite in charge and to have an invariant mass between 80 to $100\,\mathrm{GeV}$. The $Z \to \mu\bar\mu$ + fake track selection is

summarised in Table **??**.

Table 6.2: Event selection cuts for the $Z \to \mu\bar{\mu}$ + fake control sample to estimate the inclusive fake background.

Event-based selection	Two global muons with	$p_{\mathrm{T}} > 25\,\mathrm{GeV}$
		$\|\eta\| < 2.4$
		$\sum\limits_{\Delta R < 0.4} p_{\mathrm{T}}^{\mathrm{PF\ particle}} / p_{\mathrm{T}}(\mu) < 0.12$
		$\left.\frac{\chi^2}{ndof}\right\|_{\mathrm{global\ track}} < 10$
		$\|d0\| < 0.2\,\mathrm{cm}$
		$\|dz\| < 0.5\,\mathrm{cm}$
		≥ 1 hit in the muon detector considered in global fit
		≥ 2 hits in different muon stations
		≥ 1 hit in the pixel detector
		≥ 6 hits in the tracker system
	Muons opposite in charge	
	$80\,\mathrm{GeV} < M_{\mathrm{inv}}\,(\mu_1, \mu_2) < 100\,\mathrm{GeV}$	
Candidate track selection	Good quality selection	
	Kinematic selection	
	Lepton/jet veto	
	Isolation selection	

780

781 In order to select $Z \to e\bar{e}$ events in data, the two electrons are required to have
782 $p_{\mathrm{T}} > 25\,\mathrm{GeV}$, $\|\eta\| < 2.5$ and no missing hits in the inner layers of the tracker. Furthermore,
783 the electrons need to pass a conversion veto as described in [**?**] in order to reduce back-
784 ground arising from photon conversions. An isolation requirement similar to the muon
785 isolation criterion is applied with an increased threshold of 15%. The electron identifi-
786 cation is further based on a multivariate technique developed within [28] that exploits
787 electron characteristics about the track quality, the ECAL cluster shapes, and the com-
788 bination of the measurements in the tracker and in the ECAL. Again, the two electrons
789 must be opposite in charge and their invariant mass must be between $80 - 100\,\mathrm{GeV}$. A

790 summary of the $Z \to e\bar{e}$ + fake track event selection can be found in Table **??**.

Table 6.3: Event selection cuts for the $Z \to e\bar{e}$ + fake control sample to estimate the inclusive fake background.

Event-based selection	Two Electrons with	$p_{\mathrm{T}} > 25\,\mathrm{GeV}$
		$\|\eta\| < 2.5$
		$\sum_{\Delta R < 0.4} p_{\mathrm{T}}^{\mathrm{PF\ particle}}/p_{\mathrm{T}}(e) < 0.15$
		pass conversion veto [**?**]
		no missing inner tracker hits
		good MVA electron as defined in [28]
	Electrons opposite in charge	
	$80\,\mathrm{GeV} < M_{\mathrm{inv}}\,(e_1, e_2) < 100\,\mathrm{GeV}$	
Candidate track selection	Good quality selection	
	Kinematic selection	
	Lepton/jet veto	
	Isolation selection	

791

792   When applying a $Z \to \ell\bar{\ell}$ selection plus the candidate track selection, the selected tracks
793 are mostly fakes. Whether this is indeed the case can be tested on simulated $Z \to \ell\bar{\ell}$ events.
794 As can be seen in Fig. **??**, a reasonable purity in fake tracks can be achieved by applying
795 the candidate track selection on top of the $Z \to \ell\bar{\ell}$ selection. In simulated $Z \to \mu\bar{\mu}$ events,
796 a purity of 88% is achieved, whereas in simulated $Z \to e\bar{e}$ events a purity of 92% of fake
797 tracks is achieved.

798   As already mentioned, the fake rate is defined as the probability that an event contains
799 a fake track that fulfils the candidate track selection. Thus, for the $Z \to \ell\bar{\ell}$ datasets it is
800 defined as the number of events passing the full selection described in Table **??** (Table **??**)
801 divided by the number of events that pass only the event-based selection in Table **??**
802 (Table **??**)

$$\rho_{\mathrm{fake}} = \frac{N_{Z \to ll}^{\mathrm{cand\ trk\ selection}}}{N_{Z \to ll}}$$

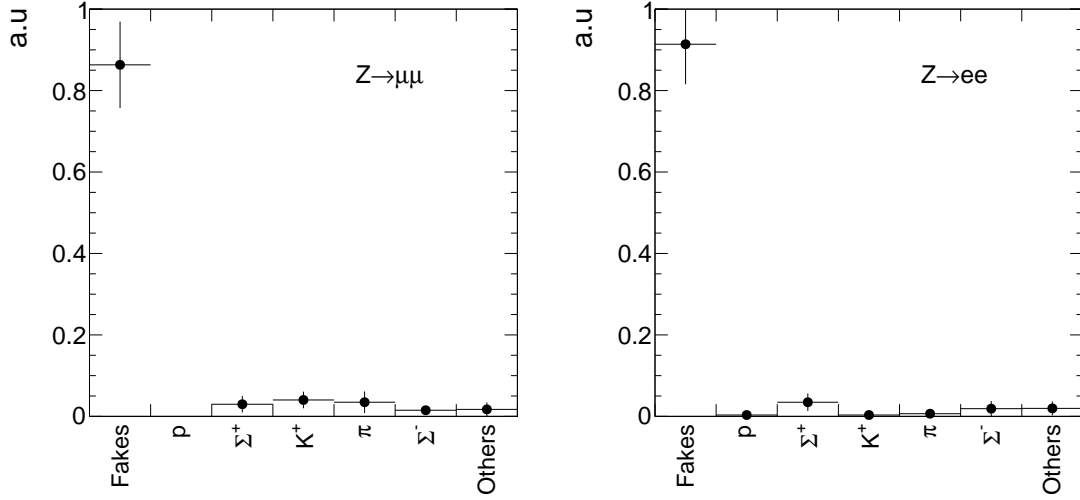803 Fake rates are determined independently for the $Z \to \mu\bar{\mu}$ + fake and $Z \to e\bar{e}$ + fake event

Figure 6.2: Corresponding generator-level particles of all tracks within $Z \rightarrow \ell\bar{\ell}$ + fake that were selected according to the candidate track selection. The full selection for tracks in $Z \rightarrow \mu\bar{\mu}$ events (left) is given in Table **??**. The full selection for tracks in $Z \rightarrow e\bar{e}$ events (right) is given in Table **??**. "Fake" means that no corresponding generator-level particle is found.

selection and then averaged to obtain the final fake rate. The fake rate with the candidate track selection given in Table **??** is $(6.86 \pm 0.25) \cdot 10^{-5}$. This is not the final result as the optimisation in p_T will add an additional p_T selection cut to the candidate track selection.

As mentioned before, it was checked within [29, 30] that the fake rate is constant for different Standard Model processes. This is shown in Fig. **??** where the fake rate is depicted for the most important SM processes. Since the fake rate is constant for different SM processes, the fake rate determined on the $Z \rightarrow \ell\bar{\ell}$ dataset can be generalised for all SM background possibly contributing to this search. Thus, the inclusive fake background can be estimated by multiplying the fake rate with the number of events selected from the MET dataset (Table **??**) by applying the event-based signal candidate requirements from Table **??**.

$$N_{\mathrm{bkg}}^{\mathrm{fake,\ inclusive\ in\ I_{as}}} = \rho_{\mathrm{fake}} \cdot N_{\mathrm{event\text{-}based\ selection}}^{\mathrm{MET}}.$$

Given the number of events after the event-based selection of $N_{\mathrm{event\text{-}based\ selection}}^{\mathrm{MET}} = 1.38 \cdot 10^6$ and the fake rate cited above, the inclusive fake background can be estimated to 94.7 ± 3.4 for the candidate track selection.

It should be noted again that the inclusive fake background estimation will be only inclusive in I_{as} not in p_T. That means that after the definition of the signal region, $N_{\mathrm{bkg}}^{\mathrm{fake,\ inclusive\ in\ I_{as}}}$ is determined with the additional optimal p_T selection.

Possible differences between the fake rate in $Z \rightarrow \ell\bar{\ell}$ events and other SM processes are

822 estimated on simulated events and taken into account as a systematic uncertainty (see
823 Section **??**).

6.1.2 dE/dx shape of fake background

825 The information about the energy release per path length for fake tracks should not be
826 taken from simulated samples as the simulation of dE/dx is not reliable (cf. Fig. 3.8).
827 Within this analysis the Asymmetric Smirnov discriminator I_{as} is used to discriminate
828 signal against background with respect to dE/dx (see Section 3.3). In order to estimate
829 the I_{as} shape of fake tracks, a control region $CR_{I_{as}}^{fake}$ is defined that is enriched with fakes
830 and shows the same I_{as} distribution as fake tracks in the signal region.

831   To enrich fake tracks, it is possible to invert the selection cuts on the number of
832 missing middle and inner hits, i.e. requiring at least one missing inner or middle hit
833 $\left(N_{miss}^{inner} + N_{miss}^{middle} > 0\right)$. Figure **??** shows the distribution of the number of missing inner
834 plus missing middle hits for fake and leptonic tracks in simulated $W + \text{jets}$ events. It can
835 be seen that this selection is enriched by fakes. The resulting purity of fakes in $CR_{I_{as}}^{fake}$ is
836 about 98% (see Fig. **??**).

837   Additionally, it must be checked whether the I_{as} shape in $CR_{I_{as}}^{fake}$ is nearly equal to the
838 I_{as} shape in the signal region. As the exact definition of the signal region will be addressed
839 during optimisation, this test is done for various p_T selection cuts.

840   The comparison of the I_{as} shape of fake tracks can only be done on simulation. Thus,
841 simulated $W + \text{jets}$ events are used to select fake tracks in both regions. A comparison of
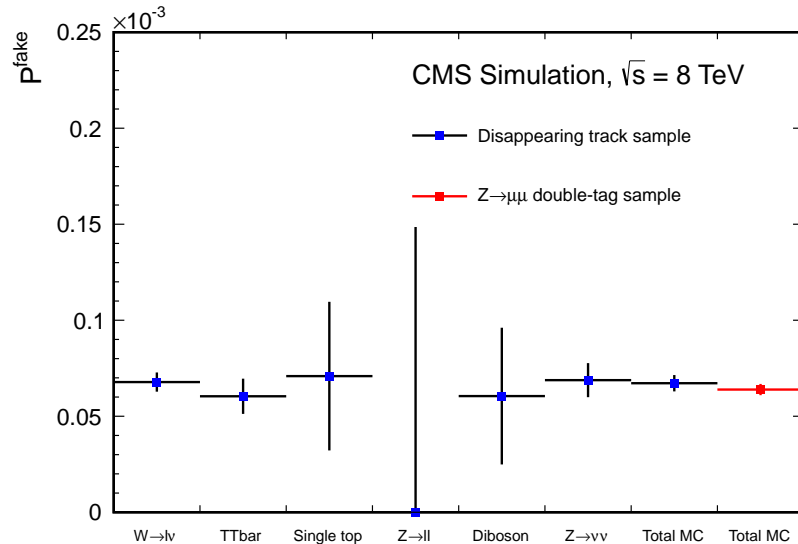
Figure 6.3: Fake track rate estimated in [29, 30] for tracks with four hits. Taken from [30]

the shape for the candidate track selection and the $\mathrm{CR}_{I_{\mathrm{as}}}^{\mathrm{fake}}$ is shown in Fig. **??**.

The I_{as} shape is almost identical in the signal and in the control region which makes the definition of the control region perfectly suited for estimating the I_{as} shape from $\mathrm{CR}_{I_{\mathrm{as}}}^{\mathrm{fake}}$ in data. The remaining shape differences are taken into account as a systematic uncertainty (discussed in Section **??**).
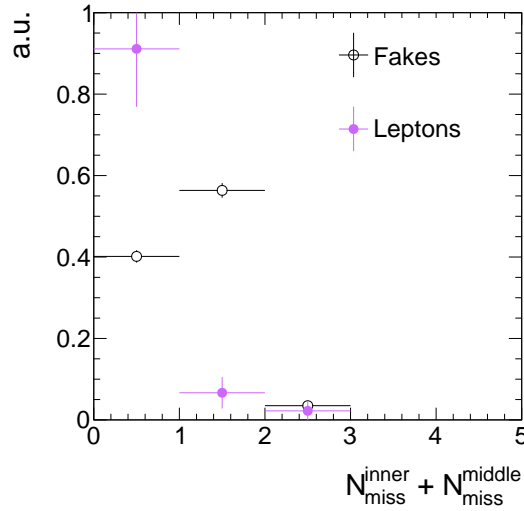
Figure 6.4: Normalised number of missing inner plus missing middle hits for fake and leptonic tracks for the full candidate track selection with the selection requirements on $N_{\mathrm{miss}}^{\mathrm{inner}}$ and $N_{\mathrm{miss}}^{\mathrm{middle}}$ removed. Trigger requirements and QCD suppression cuts were removed to enhance the statistical precision.
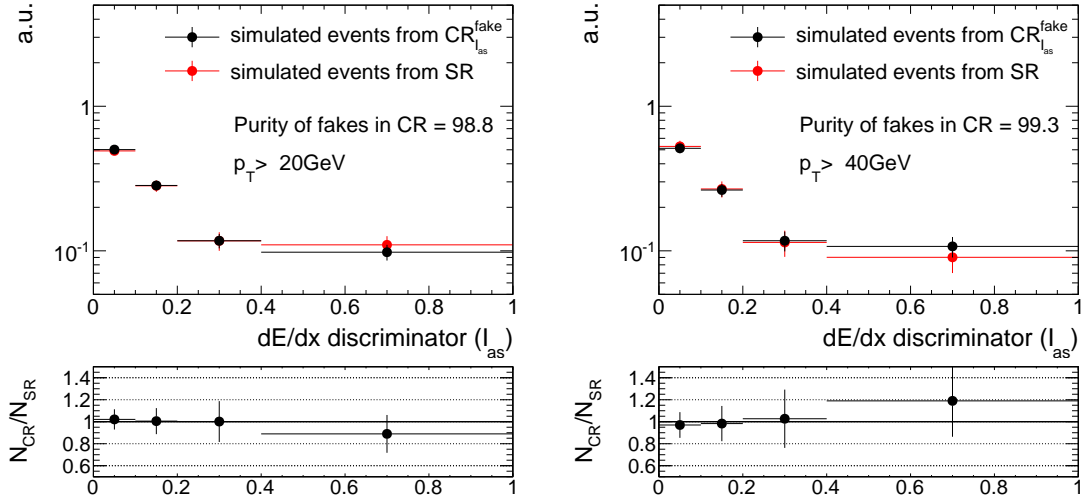
Figure 6.5: Comparison of the I_{as} shape between $CR_{I_{as}}^{fake}$ and the signal region for two different track p_T selections of $p_T > 20\,\text{GeV}$ (left) and $p_T > 40\,\text{GeV}$ (right). To enhance the statistical precision only the track-based selection is applied.

6.2 Leptonic background

The leptonic background of the here presented search is caused by non-reconstructed leptons that circumvent the lepton veto selection. However, at least non-reconstructed electrons or taus should in principle deposit enough energy in the calorimeters such that they can still be vetoed by the calorimeter isolation requirement $E_{calo}^{\Delta R < 0.5} < 5\,\text{GeV}$. As muons don't deposit much energy in the calorimeters, this reasoning does not apply to them. In the following, the sources of the three different leptonic backgrounds are characterised.

Electrons

To reject unreconstructed electrons, all tracks pointing to a dead or noisy ECAL cell, to an ECAL intermodule gap, or to the region between ECAL barrel and endcap at $1.42 < |\eta| < 1.65$ are vetoed, as described in Section **??**. By this selection, almost all electrons are efficiently rejected. In the simulated $W + \text{jets}$ sample only one simulated event remains that passes all signal candidate selection criteria and for which the candidate track can be matched to a generator-level electron. This event is visualised in Fig. **??**. The neutrino, only weakly interacting does not show any signature in the detector, whereas the electron ($p_T \simeq 90\,\text{GeV}$) leaves a track with $p_T \simeq 70\,\text{GeV}$ in the tracker. No ECAL energy deposits in the direction of the electron are visible. This is caused by the fact that the corresponding ECAL energy deposits were not read out in this event, which suggests that the corresponding ECAL tower was not working properly in 2012. An ISR

Figure 6.6: Visualisation of a $W \to e\nu_e$ event contributing to the SM background. In light blue, generator-level particles including e and ν_e of the W-boson decay are shown. Black lines represent reconstructed tracks and the red arrow indicates the missing transverse energy in the event.

jet ($p_\mathrm{T} \simeq 230\,\mathrm{GeV}$) causes the $\not\!\!E_\mathrm{T}$ in the event.

Additionally, electrons can do bremsstrahlung which can change the direction of the electron significantly. Thus, the energy deposits in the ECAL can possibly not be matched to the original electron.

Taus

Taus are contributing to the leptonic background through the hadronic decay of a tau lepton to one charged pion $\tau \to \pi^\pm \nu_\tau$. Other hadronic decay modes of the tau lepton are suppressed by the track isolation criterion. Taus can fail reconstruction if they don't deposit energy in the HCAL or ECAL. Unreconstructed taus can therefore also easily bypass the calorimeter isolation criterion. Because of nuclear interactions in the tracker, pions often result in short reconstructed tracks that can easily be highly mismeasured in p_T. Thus, taus can contribute to the background even if imposing a tight selection in the transverse momentum. Such an event is shown in Fig. **??**. The transverse momentum of the generator-level pion is only $p_\mathrm{T} \sim 10\,\mathrm{GeV}$, but because the reconstructed track is very short, it leads to a high mismeasurement of the track p_T of $\sim 40\,\mathrm{GeV}$. The shortness of the track is caused by nuclear interactions of the pion. As no corresponding ECAL or HCAL energy deposits are measured, the reconstruction of the pion fails. The ISR jet causes the $\not\!\!E_\mathrm{T}$ in the event.
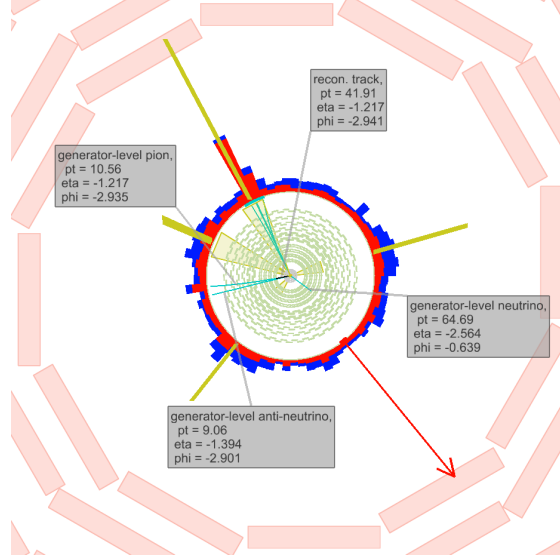
Figure 6.7: Visualisation of a $W^+ \to \tau^+ \nu_\tau \to \pi^+ \bar{\nu}_\tau \nu_\tau$ event contributing to the SM background. In light blue, the generator-level particles including π^+, $\bar{\nu}_\tau$ and ν_τ are shown. The black line represents the reconstructed pion track and the red arrow indicates the missing transverse energy in the event.

Muons

Muons can fail reconstruction if they point towards a bad cathode strip chamber. This is taken into account in the candidate track selection. However, some of the muons still fail reconstruction if they fall within the gap between stations 0 and 1 of the drift tube system at $|\eta| = 0.25$. The muon reconstruction efficiency drops from around 99% to a value of around 94% as shown in [29, 30]. This possibility is illustrated in a simulated event shown in Fig. **??**.

In [29, 30] events are rejected if the track is pointing in a region of $0.15 < |\eta| < 0.35$. In this search, this cut was omitted to maximise signal acceptance. Due to the additional selection in I_{as}, muons can be efficiently suppressed. E.g. in the event shown in Fig. **??**, the muon has an I_{as} value of about 0.007.

In general, all leptons behave like MIPs. However, as electrons are much lighter compared to muons or pions, they loose more energy via bremsstrahlung. Still, all three lepton types loose much less energy compared to hypothetical new heavy particles. To have the possibility to make an optimisation in the two main discriminating variables p_T and I_{as}, the background estimation methods are designed to work for all different p_T and I_{as} selection cuts.
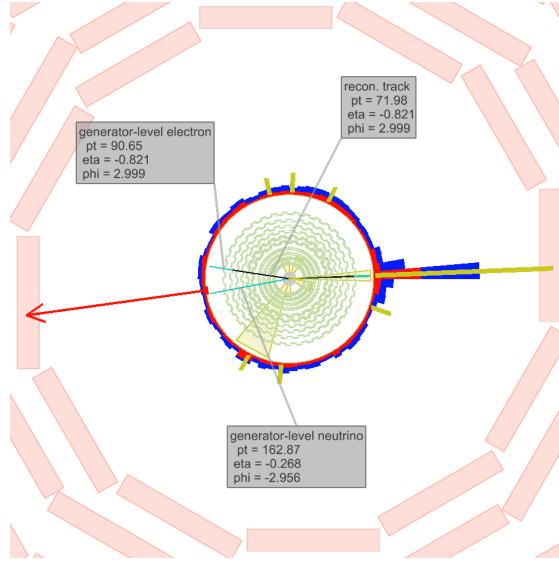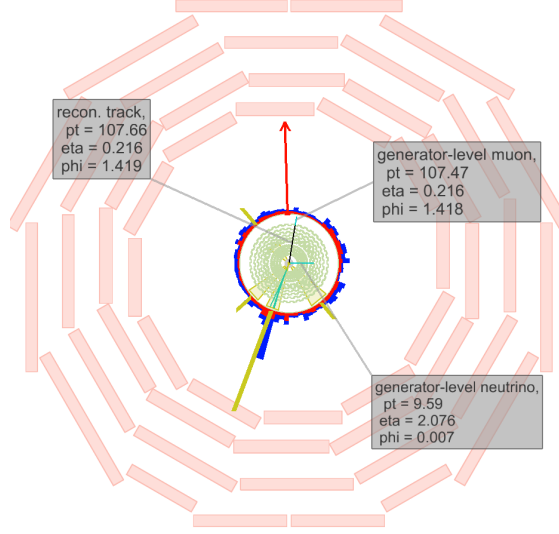
Figure 6.8: Visualisation of an $W \to \mu\nu_\mu$ event contributing to the SM background. In light blue, the generator-level particles including μ and ν_μ of the W decay are shown. The muon is pointing to the η-region between stations 0 and 1 of the DT system at $|\eta| \sim 0.25$. In this region the muon reconstruction is less efficient. No signal in the muon chambers is visible. Therefore the muon could not be reconstructed. The ISR jet causes the $\not{E}_T$ (read arrow) in the event.

As for the fakes, the leptonic background estimation is splitted into two parts. First, the estimation of the inclusive background without I_{as} information. Second, the estimation of the I_{as} shape for all three leptonic background sources.

6.2.1 Inclusive leptonic background estimation

The inclusive (without dE/dx information) lepton background estimation method is similar to the background estimation method used in [29, 30].

In order to estimate the number of events in the signal region originating from unreconstructed leptons, information from simulated events is used. With the help of simulated $W+$ jets events, the ratio $\rho_{MC}^{lep_i}$ between the number of events in the signal region with the selected track matched to a generator-level lepton $N_{SR}^{trk \text{ matched to lepton}_i}$ and the number of events in a control region $N_{CR}^{lepton_i \text{ veto inverted}}$ with a inverted lepton veto is determined. For muons, this lead to the following expression

$$\rho_{MC}^{\mu} = \frac{N_{SR,MC}^{trk \text{ matched to } \mu}}{N_{CR,MC}^{\mu \text{ veto inverted}}}.$$

Since for electrons and taus the reconstruction efficiency is highly correlated with the

916 $E_{\text{calo}}^{\Delta R<0.5}$ selection requirement, the $E_{\text{calo}}^{\Delta R<0.5}$ requirement is additionally removed in the

917 control regions for these two lepton types

$$\rho_{\text{MC}}^{e,\tau} = \frac{N_{\text{SR,MC}}^{\text{trk matched to } e,\tau}}{N_{\text{CR,MC}}^{e,\tau \text{ veto inverted}, \cancel{E_{\text{calo}}^{\Delta R<0.5}<5\,\text{GeV}}}}.$$

918 In order to estimate the inclusive background for all three lepton types, the scaling

919 factor $\rho_{\text{MC}}^{\text{lep}_i}$ is applied to the number of events in the lepton veto inverted control region

920 measured in data. Also in data the control region for electrons and taus is defined with

921 the $E_{\text{calo}}^{\Delta R<0.5}$ requirement removed. Thus, the inclusive number of predicted background

922 events can be estimated with

$$N_{\text{bkg}}^{\mu,\ \text{inclusive in I}_{\text{as}}} = \rho_{\text{MC}}^{\mu} \cdot N_{\text{CR,data}}^{\mu \text{ veto inverted}}.$$

923 for muons, and

$$N_{\text{bkg}}^{e,\tau,\ \text{inclusive in I}_{\text{as}}} = \rho_{\text{MC}}^{e,\tau} \cdot N_{\text{CR,data}}^{e,\tau \text{ veto inverted}, \cancel{E_{\text{calo}}^{\Delta R<0.5}<5\,\text{GeV}}}.$$

924 for electrons and taus.

925 This method relies on the simulation of the lepton reconstruction efficiencies which is

926 known to be reasonably accurate [?, ?, ?]. For electrons and taus the simulation of the

927 calorimeter isolation is utilised as well. Possible discrepancies between simulation and

928 data are taken into account as a systematic uncertainty via a comparison of the lepton

929 reconstruction efficiencies in data and simulation in $Z \to \ell\bar{\ell}$ events (see Section ??).

930 To reduce the statistical uncertainty, the scale factor is calculated without applying the

931 QCD suppression cuts. After the signal candidate selection described in Section ??, only

932 one event remains in the simulated $W +$ jets sample where the candidate track can be

933 matched to an electron. There are five events with a track candidate that can be matched

934 to a muon, and no selected events have tracks that can be matched to a pion from a tau

935 decay. The statistical uncertainties are calculated as the 68% upper and lower limits on

936 the inclusive background with the Neyman procedure [?, 20]. Table ?? gives the result for

937 the prediction of the inclusive leptonic background for the signal candidate selection from

938 Section ??.

939 6.2.2 dE/dx shape of leptonic background

940 In order to get information about the I_{as} (see Section 3.3) shape in the signal region

941 of electrons, muons and taus, a control region must be found where the shape of the

942 observable is at least similar to that in the signal region. The most natural control region,

943 being the lepton veto inverted control region, cannot be used because the variable I_{as} differs

Table 6.4: Scaling factor $\rho_{\mathrm{MC}}^{\mathrm{lep}_i}$, number of events in the data control region $N_{\mathrm{CR,data}}$ and the resulting inclusive estimation $N_{\mathrm{predicted}}$ after the candidate track selection.

	scaling factor $\rho_{\mathrm{MC}}^{\mathrm{lep}_i}$	$N_{\mathrm{CR,data}}$	$N_{\mathrm{predicted}}$
electrons	$1.25^{+1.70}_{-0.77} \cdot 10^{-4}$	60067	$7.49^{+10.19}_{-4.63}$
muons	$2.17^{+1.65}_{-0.93} \cdot 10^{-4}$	76664	$16.64^{+12.64}_{-7.12}$
taus	$< 2.13 \cdot 10^{-2}$	445	< 9.46

between the signal and the control region, as can be seen in Fig. **??**. The discrepancies reach factors up to an order of magnitude.

Various other control regions were tested and could not be used because of too large I_{as} shape differences to the signal region.

As no suitable control region is known where the I_{as} shape of the leptons is at least similar to the shape in the signal region, it is decided to use the I_{as} information from simulation. This introduces a large bias since dE/dx (and therefore I_{as}) is not simulated well. However, the corresponding bias is still smaller than the differences of the I_{as} shape between the signal and a control region: compare Fig. **??** and Fig. **??**.

In order to take into account the bias when using I_{as} from simulation, a systematic uncertainty is estimated that addresses simulation-data differences of the I_{as} distributions. This systematic uncertainty is discussed in Section **??**.
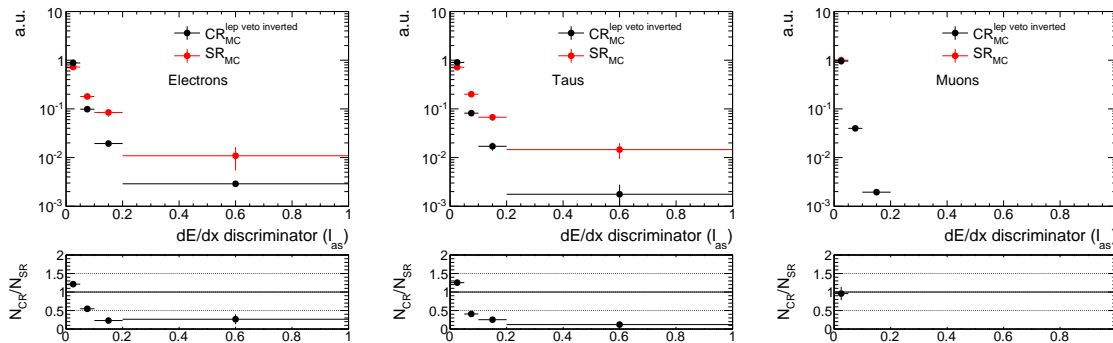

Figure 6.9: Normalised I_{as} distribution for electrons (left), pions from the tau decay (middle) and muons (right) in the signal region (red) and the lepton veto inverted control region (black).
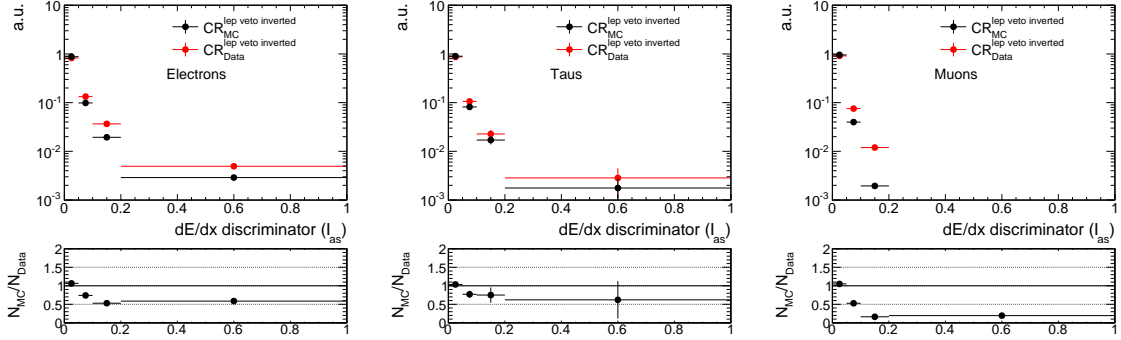
Figure 6.10: Normalised I_{as} distribution for electrons (left), pions from the tau decay (middle) and muons (right) in the lepton veto inverted control region from simulated (black) and real (red) events.

6.3 Background estimation validation

The background estimation methods are exhaustively validated in signal depleted control regions. Various control regions are used for validation. For each control region it has been verified that the signal contamination is less than the statistical uncertainty of the background prediction. For some of the models the expected number of events exceeds this limit. However, these models are already ruled out by the search for disappearing tracks [11] (see Appendix A.3).

First, to validate the estimation method of the leptonic background, a leptonic control region is defined by selecting only tracks with a minimum number of seven hits in the tracker. This reduces the fake contribution to a negligible level (cf. Fig. **??**). Additionally in order to minimise signal contamination, the calorimeter isolation requirement is inverted to $E_{\mathrm{calo}}^{\Delta R < 0.5} > 10\,\mathrm{GeV}$. This requirement ensures no overlap to the signal region.

The validation test for the control region with $E_{\mathrm{calo}}^{\Delta R < 0.5} > 10\,\mathrm{GeV}$ and $N_{\mathrm{hits}} > 6$ is shown in Table **??**. The predicted number of events by the leptonic background estimation is compatible with the observed data yield.

The fake background can only be estimated within the low calorimeter isolation region $\left(E_{\mathrm{calo}}^{\Delta R < 0.5} < 10\,\mathrm{GeV}\right)$ to ensure high fake purity. To be able to validate the method in the high calorimeter isolation region $\left(E_{\mathrm{calo}}^{\Delta R < 0.5} > 10\,\mathrm{GeV}\right)$, a translation factor from the low to the high calorimeter isolation region for the number of fake tracks is determined in the fake enriched control region $\mathrm{CR}_{I_{\mathrm{as}}}^{\mathrm{fake}}$ defined in Section **??**. In this control region, the ratio of $N_{E_{\mathrm{calo}}^{\Delta R < 0.5} > 10\,\mathrm{GeV}} / N_{E_{\mathrm{calo}}^{\Delta R < 0.5} < 10\,\mathrm{GeV}}$ is estimated and taken as a multiplicand to the number of events predicted from the $E_{\mathrm{calo}}^{\Delta R < 0.5} < 10\,\mathrm{GeV}$ region. In Table **??**, two different validation tests are shown, once an inclusive validation in I_{as} and once with an

Table 6.5: Validation test of leptonic background estimation. Left: $E_{\text{calo}}^{\Delta R<0.5} > 10\,\text{GeV}$ and $N_{\text{hits}} > 6$. Right: $E_{\text{calo}}^{\Delta R<0.5} > 10\,\text{GeV}$, $N_{\text{hits}} > 6$ and $I_{\text{as}} > 0.2$. Only statistical uncertainties are included.

	Predicted Yield	Data Yield			Predicted Yield	Data Yield
Total bkg	$131.70^{+26.30}_{-18.42}$	156		Total bkg	$0.0^{+0.50}_{-0.0}$	1
Electrons	$14.67^{+11.16}_{-6.29}$			Electrons	$0.0^{+0.07}_{-0.0}$	
Muons	$7.99^{+10.90}_{-5.00}$			Muons	$0.0^{+0.32}_{-0.0}$	
Taus	$109.04^{+21.18}_{-16.58}$			Taus	$0.0^{+0.38}_{-0.0}$	

I_{as} selection of 0.2. Again, the predicted background events is in agreement with the number of observed events.

The whole validation is done for different selections in p_{T} and I_{as}. All validation tests show good agreement. Results of a variety of validation tests with different p_{T} and I_{as} selections can be found in Appendix A.4.

Still, systematic uncertainties need to be estimated. The sources of systematic uncertainties and how they are estimated will be explained in the following section.

Table 6.6: Validation test of fake and leptonic background estimation methods. Left: $E_{\text{calo}}^{\Delta R<0.5} > 10\,\text{GeV}$. Right: $E_{\text{calo}}^{\Delta R<0.5} > 10\,\text{GeV}$ and $I_{\text{as}} > 0.2$. Only statistical uncertainties are included.

	Predicted Yield	Data Yield			Predicted Yield	Data Yield
Total bkg	$309.00^{+33.46}_{-26.62}$	324		Total bkg	$14.80^{+2.92}_{-2.85}$	16
Electrons	$59.92^{+16.11}_{-11.85}$			Electrons	$0.75^{+0.36}_{-0.25}$	
Muons	$8.04^{+10.97}_{-5.03}$			Muons	$0.00^{+0.32}_{-0.00}$	
Taus	$173.06^{+24.62}_{-20.23}$			Taus	$2.33^{+0.74}_{-0.55}$	
Fakes	$67.98^{+11.57}_{-11.57}$			Fakes	$11.72^{+2.79}_{-2.79}$	

6.4 Systematic uncertainties

Systematic uncertainties on the background estimation include:

- the uncertainty on the fake rate ρ_{fake};

- the uncertainty on the I_{as} shape of fake tracks predicted from a control region;

- the uncertainty on the leptonic scale factor $\rho_{\text{MC}}^{\text{lep}_i}$ determined with simulated events;

- the uncertainty on the I_{as} shape of the leptonic background.

6.4.1 Uncertainty on the fake rate

The fake rate ρ_{fake} is determined with the help of observed $Z \to \ell\bar{\ell}$ events. To estimate the uncertainty on this fake rate caused by differences in the fake rate between different underlying processes, a comparison between the fake rate in simulated $Z \to \ell\bar{\ell} + \text{jets}$ and simulated $W + \text{jets}$ events is done. The fake rate in the $Z \to \ell\bar{\ell} + \text{fake track}$ control samples (see Tables **??** and **??**) and the fake rate in the signal candidate selection from Table **??** in $W + \text{jets}$ events are compared.

Unfortunately, the statistical precision of the simulated $W + \text{jets}$ dataset is limited. Thus, the estimation of the systematic uncertainty is mainly driven by statistical uncertainties. In order to enhance the statistical precision of the estimation, the selection requirements on $\not{E}_{\text{T}}$ and $p_{\text{T}}^{1^{\text{st}}\,\text{jet}}$ are loosened and the QCD suppression requirements are removed. As these variables are not expected to be correlated with the fake rate, the relative uncertainty of the fake rate should stay the same. That this is indeed the case, can be seen in Table **??**.

Table 6.7: Fake rates in simulated $W + \text{jets}$ and $Z \to \ell\bar{\ell} + \text{jets}$ events for different event-based selections of the $W + \text{jets}$ sample. The track-based selection is the candidate track selection from Table **??**.

$W + \text{jets}$ selection	$\rho_{\text{fake}}^{W+\text{jets}}$	$\rho_{\text{fake}}^{Z\to\ell\bar{\ell}}$
$\not{E}_{\text{T}} > 100\,\text{GeV}$, $p_{\text{T}}^{1^{\text{st}}\,\text{jet}} > 110\,\text{GeV}$	$\left(3.16^{+4.26}_{-1.94}\right)\cdot 10^{-5}$	$(3.17 \pm 0.21)\cdot 10^{-5}$
$\not{E}_{\text{T}} > 0\,\text{GeV}$, $p_{\text{T}}^{1^{\text{st}}\,\text{jet}} > 70\,\text{GeV}$	$(3.03 \pm 0.68)\cdot 10^{-5}$	$(3.17 \pm 0.21)\cdot 10^{-5}$
$\not{E}_{\text{T}} > 0\,\text{GeV}$, $p_{\text{T}}^{1^{\text{st}}\,\text{jet}} > 70\,\text{GeV}$, no QCD cuts	$(3.05 \pm 0.44)\cdot 10^{-5}$	$(3.17 \pm 0.21)\cdot 10^{-5}$

The systematic uncertainty is estimated as the 1-sigma deviation of the ratio $\rho_{\text{fake}}^{W+\text{jets}}/\rho_{\text{fake}}^{Z\to\ell\bar{\ell}}$ from 1. For the candidate track selection, this is estimated to $\rho_{\text{fake}}^{W+\text{jets}}/\rho_{\text{fake}}^{Z\to\ell\bar{\ell}} = 0.96 \pm 0.16$ leading to a systematic uncertainty ont the fake rate of 20%.

6.4.2 Uncertainty on the dE/dx shape of fake tracks

The systematic uncertainty on the shape of the I_{as} distribution takes into account the differences between the I_{as} shape in the fake control region $\mathrm{CR}_{I_{as}}^{\mathrm{fake}}$ and in the signal region. For the estimation, information from simulated $W + \text{jets}$ events is used. A comparison between the simulated I_{as} shape in the signal and in the control region can be seen in Fig. **??**. To enhance the statistical precision only track-based selection cuts are applied.

The 1-sigma difference of the ratio of the number of events in the signal region and the control region from one is taken as systematic uncertainty. For a signal region definition with $p_T > 20\,\text{GeV}$ and $I_{as} > 0.2$ this corresponds to an uncertainty of around 21% and for a definition with $p_T > 40\,\text{GeV}$ and $I_{as} > 0.2$ of around 25%.
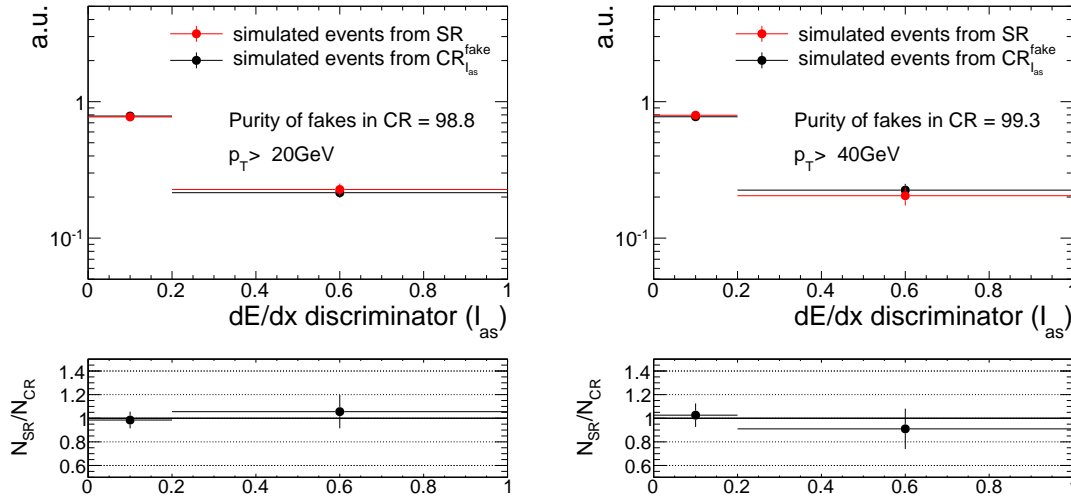
Figure 6.11: Normalised distributions of the I_{as} shape of fake tracks in the signal and control region of simulated $W + \text{jets}$ events with a p_T selection of $20\,\text{GeV}$ (left) and a $40\,\text{GeV}$ (right).

6.4.3 Uncertainty on the leptonic scale factor

The leptonic scale factor $\rho_{\mathrm{MC}}^{\mathrm{lep}_i}$ is estimated on simulated $W + \text{jets}$ events. The corresponding systematic uncertainty that addresses the use of information from simulation is derived by a "tag-and-probe" method conducted on real data and simulated events.

For this method a selection of $Z \to \ell\bar{\ell}$ events is done with one "tagged" well reconstructed lepton and one "probed" candidate track. To ensure a selection of $Z \to \ell\bar{\ell}$ events, a selection on the invariant mass of the reconstructed lepton and the candidate track is applied with $80\,\text{GeV} < M_{\mathrm{inv}}\,(\text{lepton}, \text{cand. trk}) < 100\,\text{GeV}$ for muons and electrons. For taus, a muon from a $\tau \to \mu\nu\nu$ decay is selected with $40\,\text{GeV} < M_{\mathrm{inv}}\,(\mu, \text{cand. trk}) < 75\,\text{GeV}$

1028 and $m_T\left(\mu, E_T\right) < 40\,\mathrm{GeV}$ [29, 30]. Furthermore, the candidate track and the lepton are
1029 required to be opposite in charge. In order to reduce the contamination of fakes in the
1030 "tag-and-probe" samples an additional selection on the number of hits of $N_{\mathrm{hits}} > 5$ is
1031 required.

1032 The "tag-and-probe" selection is done for each lepton type separately. In order to deter-
1033 mine the leptonic scale factors, the number of events is once estimated for the candidate
1034 track selection including the corresponding lepton veto which gives the number of events
1035 in the "tag-and-probe" signal region $N_{SR}^{\mathrm{T\&P}}$, and once inverting the lepton veto selection
1036 requirement which gives the number of events in the "tag-and-probe" lepton inverted con-
1037 trol region $N_{\mathrm{CR,\ lepton\ veto\ inverted}}^{\mathrm{T\&P}}$. As for the determination of the tau and electron scale
1038 factor with simulated $W + \mathrm{jets}$ events, no requirement on the calorimeter isolation is ap-
1039 plied in the lepton veto inverted control region for taus and electrons. This leads to the
1040 following expression of the lepton scale factor for muons

$$\rho^{\mu} = \frac{N_{\mathrm{SR}}^{\mathrm{T\&P}\mu}}{N_{\mathrm{CR,\ }\mu\mathrm{\ veto\ inverted}}^{\mathrm{T\&P}}}.$$

1041 and for electrons and taus

$$\rho^{e,\tau} = \frac{N_{\mathrm{SR}}^{\mathrm{T\&P}e,\tau}}{N_{\mathrm{CR,\ }e,\tau\mathrm{\ veto\ inverted}}^{\mathrm{T\&P}}}.$$

1042 The selection requirements for the three tag-and-probe samples are listed in Tables A.11, A.12
1043 and A.13 in Appendix A.5.

1044 The leptonic scale factors are calculated using simulated $Z \to \ell\bar{\ell}$ events and real data
1045 from the single-muon and single-electron samples listed in Table **??**. The 1-sigma difference
1046 of the ratio $\rho_{\mathrm{MC}}^{\mathrm{lep}_i}/\rho_{\mathrm{Data}}^{\mathrm{lep}_i}$ from unity is taken as systematic uncertainty. This results for the
1047 signal candidate selection in an uncertainty of 69% for the electron, 39% for the muon and
1048 79 % for the tau scale factor.

1049 6.4.4 Uncertainty on the leptonic dE/dx shape

1050 The uncertainty on lepton I_{as} shape is estimated by a comparison of the I_{as} shape in data
1051 and simulation in the lepton veto inverted control region. Figure **??** shows the leptonic
1052 I_{as} distributions for all three lepton types in the lepton veto inverted control region in
1053 data and simulation. The 1-sigma difference of the ratio of the number of events in the
1054 control region in data and simulation from 1 is taken as systematic uncertainty. This leads
1055 for example to uncertainties between $37\% - 81\%$ for the signal candidate selection plus a
1056 selection requirement of $I_{\mathrm{as}} > 0.2$.
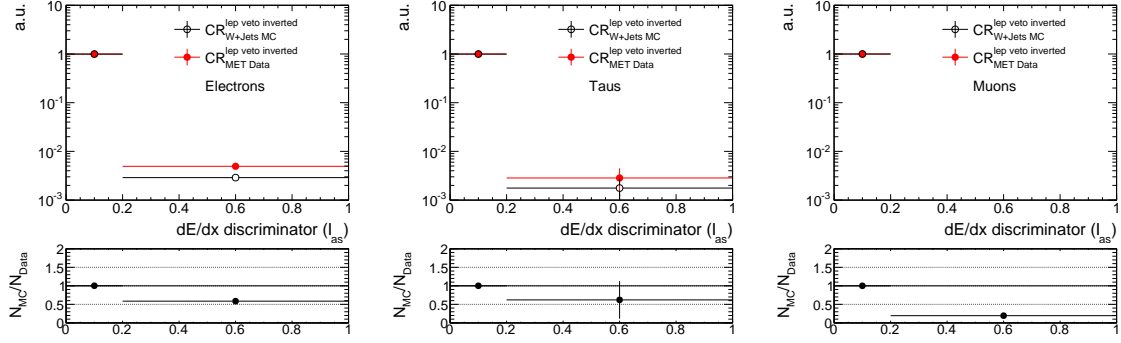
Figure 6.12: Normalised distributions of the lepton I_{as} distributions in the lepton veto inverted control region for data (red) and simulation (black) for all three lepton types. The event-based selection requirements and the calorimeter isolation requirement are removed to enhance the statistical precision.

A A search for highly ionising, short tracks

A.1 Lifetime reweighting

The probability density function of a particle's proper lifetime for a sample generated with a particle's mean lifetime τ^{gen} is given by

$$p\left(t\right) = \frac{1}{\tau^{\text{gen}}} \cdot \exp\left[-\frac{t}{\tau^{\text{gen}}}\right].$$

After carrying out the lifetime reweighting procedure, the targeted p.d.f of the particle's new mean lifetime τ^{target} is given by

$$p'\left(t\right) = \frac{1}{\tau^{\text{target}}} \cdot \exp\left[-\frac{t}{\tau^{\text{target}}}\right].$$

Thus, an event containing a particle with individual proper lifetime can be reweighted with the following weight

$$w = \frac{p'\left(t\right)}{p\left(t\right)} = \frac{\tau^{\text{gen}}}{\tau^{\text{target}}} \cdot \exp\left[\frac{t}{\tau^{\text{gen}}} - \frac{t}{\tau^{\text{target}}}\right].$$

For more than one non-stable particle, the event weight is calculated by multiplying the weights of the single reweighting procedures.

A.2 Event yields for simulated samples and data

Table A.1: Event yields after each selection step for various simulated background samples.

Selection	W + jets	$t\bar{t}$ + jets	$Z \to \ell\bar{\ell}$	Multijet
after skim	$9.16 \cdot 10^7$	$1.04 \cdot 10^6$	$2.21 \cdot 10^7$	$1.38 \cdot 10^{11}$
trigger	$4.31 \cdot 10^6$	$1.15 \cdot 10^5$	$4.23 \cdot 10^3$	$4.32 \cdot 10^6$
$p_T^{\text{1st jet}} > 110\,\text{GeV}$	$2.47 \cdot 10^6$	$7.17 \cdot 10^4$	$2.60 \cdot 10^3$	$2.75 \cdot 10^6$
$\not{E}_T > 100\,\text{GeV}$	$1.89 \cdot 10^6$	$5.31 \cdot 10^4$	$6.26 \cdot 10^2$	$9.63 \cdot 10^5$
$\Delta\phi_{\max}\left(\text{jet}_i, \text{jet}_j\right) < 2.7$	$1.11 \cdot 10^6$	$6.81 \cdot 10^3$	$1.32 \cdot 10^2$	$2.01 \cdot 10^4$
$\Delta\phi_{\max}\left(\text{jet}_{1,2}, \not{E}_T\right) > 0.5$	$1.11 \cdot 10^6$	$6.76 \cdot 10^3$	$1.32 \cdot 10^2$	$9.55 \cdot 10^3$
≥ 1 track in the event with:				
reconstructed trk	$1.10 \cdot 10^6$	$6.75 \cdot 10^3$	$1.32 \cdot 10^2$	$9.55 \cdot 10^3$
high-purity	$1.10 \cdot 10^6$	$6.74 \cdot 10^3$	$1.32 \cdot 10^2$	$9.55 \cdot 10^3$
$N_{\text{miss}}^{\text{middle}} = 0$	$1.09 \cdot 10^6$	$6.72 \cdot 10^3$	$1.32 \cdot 10^2$	$9.55 \cdot 10^3$
$N_{\text{miss}}^{\text{inner}} = 0$	$1.07 \cdot 10^6$	$6.70 \cdot 10^3$	$1.32 \cdot 10^2$	$9.55 \cdot 10^3$
$|d0| < 0.02\,\text{cm}$	$1.07 \cdot 10^6$	$6.64 \cdot 10^3$	$1.32 \cdot 10^2$	$9.55 \cdot 10^3$
$|dz| < 0.5\,\text{cm}$	$1.07 \cdot 10^6$	$6.63 \cdot 10^3$	$1.32 \cdot 10^2$	$9.55 \cdot 10^3$
$|\eta| < 2.1$	$1.03 \cdot 10^6$	$6.58 \cdot 10^3$	$1.32 \cdot 10^2$	$9.55 \cdot 10^3$
$p_T > 20\,\text{GeV}$	$8.14 \cdot 10^5$	$5.63 \cdot 10^3$	$1.32 \cdot 10^2$	$5.48 \cdot 10^3$
No μ within $\Delta R < 0.15$	$7.15 \cdot 10^5$	$4.52 \cdot 10^3$	$1.32 \cdot 10^2$	$5.48 \cdot 10^3$
No e within $\Delta R < 0.15$	$6.69 \cdot 10^5$	$3.67 \cdot 10^3$	$7.86 \cdot 10^1$	$5.48 \cdot 10^3$
No τ within $\Delta R < 0.15$	$6.62 \cdot 10^5$	$3.61 \cdot 10^3$	$7.86 \cdot 10^1$	$5.47 \cdot 10^3$
No jet within $\Delta R < 0.5$	$1.18 \cdot 10^3$	$1.44 \cdot 10^1$	$1.09 \cdot 10^1$	$0.00 \cdot 10^0$
Not within $\Delta R < 0.05$ of a dead/noisy ECAL cell	$7.25 \cdot 10^2$	$8.02 \cdot 10^0$	$0.00 \cdot 10^0$	$0.00 \cdot 10^0$
Not within an ECAL intermodule gap	$7.15 \cdot 10^2$	$8.02 \cdot 10^0$	$0.00 \cdot 10^0$	$0.00 \cdot 10^0$
Not within $1.42 < |\eta| < 1.65$	$5.89 \cdot 10^2$	$6.53 \cdot 10^0$	$0.00 \cdot 10^0$	$0.00 \cdot 10^0$
Not within $\Delta R < 0.25$ to a bad CSC	$5.02 \cdot 10^2$	$5.88 \cdot 10^0$	$0.00 \cdot 10^0$	$0.00 \cdot 10^0$
$\sum_{\Delta R < 0.3} p_T^{\text{trk}} / p_T^{\text{cand}} - 1 < 0.1$	$4.46 \cdot 10^2$	$4.78 \cdot 10^0$	$0.00 \cdot 10^0$	$0.00 \cdot 10^0$
$E_{\text{calo}}^{\Delta R < 0.5} < 5\,\text{GeV}$	$3.19 \cdot 10^1$	$0.67 \cdot 10^0$	$0.00 \cdot 10^0$	$0.00 \cdot 10^0$
$p_T > 30\,\text{GeV}$	$\cdot 10^1$	$\cdot 10^1$	$\cdot 10^1$	$\cdot 10^1$
$I_{\text{as}} > 0.05$	$\cdot 10^1$	$\cdot 10^1$	$\cdot 10^1$	$\cdot 10^1$

Table A.2: Event yields after each selection step for various signal models.

Selection	m=100 GeV $c\tau$=10 cm	m=100 GeV $c\tau$=100 cm	m=500 GeV $c\tau$=10 cm	m=500 GeV $c\tau$=100 cm
total	$3.41 \cdot 10^5$	$3.41 \cdot 10^5$	$3.46 \cdot 10^2$	$3.46 \cdot 10^2$
trigger	$1.55 \cdot 10^4$	$1.49 \cdot 10^4$	$4.62 \cdot 10^1$	$4.62 \cdot 10^1$
$p_T^{1^{st} jet} > 110\,GeV$	$1.10 \cdot 10^4$	$1.04 \cdot 10^4$	$3.64 \cdot 10^1$	$3.58 \cdot 10^1$
$\not{E}_T > 100\,GeV$	$1.09 \cdot 10^4$	$9.83 \cdot 10^3$	$3.63 \cdot 10^1$	$3.57 \cdot 10^1$
$\Delta\phi_{max}\left(jet_i, jet_j\right) < 2.7$	$7.90 \cdot 10^3$	$7.04 \cdot 10^3$	$2.76 \cdot 10^1$	$2.72 \cdot 10^1$
$\Delta\phi_{max}\left(jet_{1,2}, \not{E}_T\right) > 0.5$	$7.90 \cdot 10^3$	$6.98 \cdot 10^3$	$2.76 \cdot 10^1$	$2.71 \cdot 10^1$
≥ 1 track in the event with:				
reconstructed trk	$3.13 \cdot 10^3$	$5.74 \cdot 10^3$	$5.74 \cdot 10^0$	$2.13 \cdot 10^1$
high-purity	$2.91 \cdot 10^3$	$5.65 \cdot 10^3$	$5.25 \cdot 10^0$	$2.08 \cdot 10^1$
$N_{miss}^{middle} = 0$	$2.87 \cdot 10^3$	$5.46 \cdot 10^3$	$5.23 \cdot 10^0$	$2.02 \cdot 10^1$
$N_{miss}^{inner} = 0$	$2.86 \cdot 10^3$	$5.40 \cdot 10^3$	$5.22 \cdot 10^0$	$2.01 \cdot 10^1$
$|d0| < 0.02\,cm$	$2.81 \cdot 10^3$	$5.39 \cdot 10^3$	$5.07 \cdot 10^0$	$2.00 \cdot 10^1$
$|dz| < 0.5\,cm$	$2.80 \cdot 10^3$	$5.38 \cdot 10^3$	$5.07 \cdot 10^0$	$2.00 \cdot 10^1$
$|\eta| < 2.1$	$2.63 \cdot 10^3$	$4.97 \cdot 10^3$	$5.01 \cdot 10^0$	$1.91 \cdot 10^1$
$p_T > 20\,GeV$	$2.54 \cdot 10^3$	$4.93 \cdot 10^3$	$4.73 \cdot 10^0$	$1.89 \cdot 10^1$
No μ within $\Delta R < 0.15$	$2.54 \cdot 10^3$	$4.65 \cdot 10^3$	$4.72 \cdot 10^0$	$1.87 \cdot 10^1$
No e within $\Delta R < 0.15$	$2.54 \cdot 10^3$	$4.65 \cdot 10^3$	$4.72 \cdot 10^0$	$1.87 \cdot 10^1$
No τ within $\Delta R < 0.15$	$2.54 \cdot 10^3$	$4.64 \cdot 10^3$	$4.72 \cdot 10^0$	$1.87 \cdot 10^1$
No jet within $\Delta R < 0.5$	$2.53 \cdot 10^3$	$4.59 \cdot 10^3$	$4.63 \cdot 10^0$	$1.82 \cdot 10^1$
Not within $\Delta R < 0.05$ of a dead/noisy ECAL cell	$2.32 \cdot 10^3$	$4.25 \cdot 10^3$	$4.19 \cdot 10^0$	$1.69 \cdot 10^1$
Not within an ECAL intermodule gap	$2.31 \cdot 10^3$	$4.23 \cdot 10^3$	$4.17 \cdot 10^0$	$1.68 \cdot 10^1$
Not within $1.42 < |\eta| < 1.65$	$2.09 \cdot 10^3$	$3.88 \cdot 10^3$	$3.95 \cdot 10^0$	$1.56 \cdot 10^1$
Not within $\Delta R < 0.25$ to a bad CSC	$1.99 \cdot 10^3$	$3.67 \cdot 10^3$	$3.83 \cdot 10^0$	$1.50 \cdot 10^1$
$\sum_{\Delta R < 0.3} p_T^{trk}/p_T^{cand} - 1 < 0.1$	$1.97 \cdot 10^3$	$3.64 \cdot 10^3$	$3.78 \cdot 10^0$	$1.49 \cdot 10^1$
$E_{calo}^{\Delta R < 0.5} < 5\,GeV$	$1.67 \cdot 10^3$	$3.04 \cdot 10^3$	$3.39 \cdot 10^0$	$1.26 \cdot 10^1$
$p_T > 30\,GeV$	$\cdot 10^1$	$\cdot 10^1$	$\cdot 10^1$	$\cdot 10^1$
$I_{as} > 0.05$	$\cdot 10^1$	$\cdot 10^1$	$\cdot 10^1$	$\cdot 10^1$

Table A.3: Observed event yield after each selection step in data.

Selection	MET dataset
after skim	$1.07 \cdot 10^7$
trigger	$1.07 \cdot 10^7$
$p_T^{1^{st}\,jet} > 110\,\mathrm{GeV}$	$6.82 \cdot 10^6$
$\not{E}_T > 100\,\mathrm{GeV}$	$3.94 \cdot 10^6$
$\Delta\phi_{\mathrm{max}}\left(\mathrm{jet}_i, \mathrm{jet}_j\right) < 2.7$	$1.39 \cdot 10^6$
$\Delta\phi_{\mathrm{max}}\left(\mathrm{jet}_{1,2}, \not{E}_T\right) > 0.5$	$1.38 \cdot 10^6$
≥ 1 track in the event with:	
reconstructed trk	$1.37 \cdot 10^6$
high-purity	$1.36 \cdot 10^6$
$N_{\mathrm{miss}}^{\mathrm{middle}} = 0$	$1.34 \cdot 10^6$
$N_{\mathrm{miss}}^{\mathrm{inner}} = 0$	$1.31 \cdot 10^6$
$|d0| < 0.02\,\mathrm{cm}$	$1.30 \cdot 10^6$
$|dz| < 0.5\,\mathrm{cm}$	$1.30 \cdot 10^6$
$|\eta| < 2.1$	$1.26 \cdot 10^6$
$p_T > 20\,\mathrm{GeV}$	$9.51 \cdot 10^5$
No μ within $\Delta R < 0.15$	$8.40 \cdot 10^5$
No e within $\Delta R < 0.15$	$8.01 \cdot 10^5$
No τ within $\Delta R < 0.15$	$7.95 \cdot 10^5$
No jet within $\Delta R < 0.5$	$1.75 \cdot 10^3$
Not within $\Delta R < 0.05$ of a dead/noisy ECAL cell	$9.11 \cdot 10^2$
Not within an ECAL intermodule gap	$9.06 \cdot 10^2$
Not within $1.42 < |\eta| < 1.65$	$7.33 \cdot 10^2$
Not within $\Delta R < 0.25$ to a bad CSC	$6.16 \cdot 10^2$
$\sum\limits_{\Delta R < 0.3} p_T^{\mathrm{trk}}/p_T^{\mathrm{cand}} - 1 < 0.1$	$5.26 \cdot 10^2$
$E_{\mathrm{calo}}^{\Delta R < 0.5} < 5\,\mathrm{GeV}$	$1.19 \cdot 10^2$
$p_T > 30\,\mathrm{GeV}$	$9.10 \cdot 10^1$
$I_{\mathrm{as}} > 0.05$	$5.60 \cdot 10^1$

A.3 Signal contamination in validation regions

Signal contamination in the four validation regions from Section **??**. The highest signal contamination is visible for a lifetime of 100 cm for all signal masses. For higher lifetimes the signal contamination is again reduced due to the muon veto selection requirement. The most extreme values (from $c\tau = 100\,\text{cm}$) of expected signal events and some other selected signal models are shown in the following tables. The signal contamination is rapidly falling towards lower lifetimes and higher masses.

Table A.4: Signal contamination in leptonic control region: $E_{\text{calo}}^{\Delta R<0.5} > 10\,\text{GeV}$ and $N_{\text{hits}} > 6$. N_S is the number of expected signal events and ΔB is the statistical uncertainty on the background prediction.

Signal model	N_S	$N_S/\Delta B$	Excluded by [11]
mass=100 GeV, $c\tau$ =100 cm	211.93	8.06	yes
mass=100 GeV, $c\tau$ =10 cm	27.83	1.06	yes
mass=100 GeV, $c\tau$ =5 cm	7.39	0.28	yes
mass=100 GeV, $c\tau$ =1 cm	0	0	no
mass=300 GeV, $c\tau$ =100 cm	6.97	0.26	yes
mass=300 GeV, $c\tau$ =10 cm	0.33	0.01	yes
mass=300 GeV, $c\tau$ =5 cm	0.0	0.0	no
mass=500 GeV, $c\tau$ =100 cm	0.72	0.03	yes
mass=500 GeV, $c\tau$ =10 cm	0.00	0.00	no

Table A.5: Signal contamination in leptonic control region: $E_{\text{calo}}^{\Delta R<0.5} > 10\,\text{GeV}$, $N_{\text{hits}} > 6$ and $I_{\text{as}} > 0.2$. N_S is the number of expected signal events and ΔB is the statistical uncertainty on the background prediction.

Signal model	N_S	$N_S/\Delta B$	Excluded by [11]
mass=100 GeV, $c\tau$ =100 cm	24.11	48.21	yes
mass=100 GeV, $c\tau$ =10 cm	0.00	0.00	yes
mass=300 GeV, $c\tau$ =100 cm	2.03	4.06	yes
mass=300 GeV, $c\tau$ =10 cm	0.03	0.07	yes
mass=300 GeV, $c\tau$ =5 cm	0.0	0.0	no
mass=500 GeV, $c\tau$ =100 cm	0.38	0.75	yes
mass=500 GeV, $c\tau$ =10 cm	0.00	0.00	no

Table A.6: Signal contamination in fake+lepton control region: $E_{\text{calo}}^{\Delta R<0.5} > 10\,\text{GeV}$. N_S is the number of expected signal events and ΔB is the statistical uncertainty on the background prediction.

Signal model	N_S	$N_S/\Delta B$	Excluded by [11]
mass=100 GeV, $c\tau$ =100 cm	257.33	7.69	yes
mass=100 GeV, $c\tau$ =10 cm	116.21	3.47	yes
mass=100 GeV, $c\tau$ =5 cm	48.07	1.44	yes
mass=100 GeV, $c\tau$ =1 cm	1.26	0.04	no
mass=300 GeV, $c\tau$ =100 cm	9.35	0.28	yes
mass=300 GeV, $c\tau$ =10 cm	2.20	0.07	yes
mass=300 GeV, $c\tau$ =5 cm	0.85	0.03	no
mass=500 GeV, $c\tau$ =100 cm	1.10	0.03	yes
mass=500 GeV, $c\tau$ =10 cm	0.15	0.00	no

Table A.7: Signal contamination in fake+lepton control region: $E_{\text{calo}}^{\Delta R<0.5} > 10\,\text{GeV}$, and $I_{\text{as}} > 0.2$. N_S is the number of expected signal events and ΔB is the statistical uncertainty on the background prediction.

Signal model	N_S	$N_S/\Delta B$	Excluded by [11]
mass=100 GeV, cτ =100 cm	36.40	12.47	yes
mass=100 GeV, cτ =10 cm	5.22	1.79	yes
mass=100 GeV, cτ =5 cm	1.76	0.60	yes
mass=300 GeV, cτ =100 cm	3.20	1.10	yes
mass=300 GeV, cτ =10 cm	0.58	0.20	yes
mass=300 GeV, cτ =5 cm	0.12	0.04	no
mass=500 GeV, cτ =100 cm	0.63	0.22	yes
mass=500 GeV, cτ =10 cm	0.07	0.02	no

A.4 Validation tests of the background estimation methods

Table A.8: Validation tests of the background estimation methods in the calorimeter isolation control region $E_{\text{calo}}^{\Delta R<0.5} > 10\,\text{GeV}$ for two different p_{T} selection requirements: $p_{\text{T}} > 40\,\text{GeV}$ (left) and $p_{\text{T}} > 60\,\text{GeV}$ (right). Only statistical uncertainties are included.

	Predicted Yield	Data Yield
Total bkg	$84.36^{+16.47}_{-10.88}$	94
Electrons	$15.69^{+11.92}_{-6.72}$	
Muons	$5.67^{+7.74}_{-3.55}$	
Taus	$35.78^{+5.09}_{-4.18}$	
Fakes	$27.23^{+6.57}_{-6.57}$	

	Predicted Yield	Data Yield
Total bkg	$35.56^{+11.95}_{-6.20}$	53
Electrons	$0.00^{+9.14}_{-0.00}$	
Muons	$3.65^{+4.98}_{-2.28}$	
Taus	$13.22^{+1.88}_{-1.55}$	
Fakes	$18.70^{+5.55}_{-5.55}$	

Table A.9: Validation tests of the background estimation methods in the calorimeter isolation control region $E_{\mathrm{calo}}^{\Delta R<0.5} > 10\,\mathrm{GeV}$ with an additional I_{as} selection of $I_{\mathrm{as}} > 0.2$ for two different p_{T} selection requirements: $p_{\mathrm{T}} > 40\,\mathrm{GeV}$ (left) and $p_{\mathrm{T}} > 60\,\mathrm{GeV}$ (right). Only statistical uncertainties are included.

	Predicted Yield	Data Yield
Total bkg	$4.76^{+1.42}_{-1.39}$	8
Electrons	$0.20^{+0.17}_{-0.10}$	
Muons	$0.00^{+0.22}_{-0.00}$	
Taus	$0.48^{+0.15}_{-0.11}$	
Fakes	$4.08^{+1.38}_{-1.38}$	

	Predicted Yield	Data Yield
Total bkg	$2.31^{+0.97}_{-0.95}$	3
Electrons	$0.00^{+0.11}_{-0.00}$	
Muons	$0.00^{+0.14}_{-0.00}$	
Taus	$0.18^{+0.06}_{-0.04}$	
Fakes	$2.14^{+0.95}_{-0.95}$	

Table A.10: Validation tests of the background estimation methods in the calorimeter isolation control region $E_{\mathrm{calo}}^{\Delta R<0.5} > 10\,\mathrm{GeV}$ with an additional I_{as} selection of $I_{\mathrm{as}} > 0.4$ for two different p_{T} selection requirements: $p_{\mathrm{T}} > 40\,\mathrm{GeV}$ (left) and $p_{\mathrm{T}} > 60\,\mathrm{GeV}$ (right). Only statistical uncertainties are included.

	Predicted Yield	Data Yield
Total bkg	$1.98^{+0.87}_{-0.83}$	2
Electrons	$0.00^{+0.05}_{-0.00}$	
Muons	$0.00^{+0.22}_{-0.00}$	
Taus	$0.08^{+0.09}_{-0.04}$	
Fakes	$1.91^{+0.83}_{-0.83}$	

	Predicted Yield	Data Yield
Total bkg	$1.10^{+0.63}_{-0.61}$	1
Electrons	$0.00^{+0.00}_{-0.00}$	
Muons	$0.00^{+0.14}_{-0.00}$	
Taus	$0.03^{+0.03}_{-0.02}$	
Fakes	$1.07^{+0.61}_{-0.61}$	

The underprediction in the control regions with $I_{\mathrm{as}} > 0.2$ is caused by the prediction of the leptonic I_{as} shape from simulation. This leads to a bias as the I_{as} distribution in simulation is softer than in data. However, this bias is taken into account as systematic uncertainty (see Section **??**).

1080 A.5 Selection requirements of the "tag-and-probe" samples

Table A.11: Event selection cuts for the muon "tag-and-probe" samples (T&P signal region sample and T&P lepton veto inverted control region sample) that are used to estimate the uncertainty on the muon scale factor ρ_{MC}^{μ}.

Muon selection	$p_{\mathrm{T}} > 25\,\mathrm{GeV}$
	$\|\eta\| < 2.4$
	$\sum\limits_{\Delta R < 0.4} p_{\mathrm{T}}^{\mathrm{PF\ particle}}/p_{\mathrm{T}}(\mu) < 0.12$
	$\left.\frac{\chi^2}{ndof}\right\|_{\mathrm{global\ track}} < 10$
	$\|d0\| < 0.2\,\mathrm{cm}$
	$\|dz\| < 0.5\,\mathrm{cm}$
	≥ 1 hit in the muon detector
	≥ 2 hits in different muon detector planes
	≥ 1 hit in the pixel detector
	≥ 6 hits in the tracker system
Candidate track selection	Good quality selection
	Kinematic selection
	Lepton/jet veto (μ veto inverted for the "tag-and-probe" control region)
	Isolation selection
	$N_{\mathrm{hits}} > 5$
Event-based selection	Muon and candidate track opposite in charge
	$80\,\mathrm{GeV} < M_{\mathrm{inv}}(\mu, \mathrm{can.\ trk}) < 100\,\mathrm{GeV}$

Table A.12: Event selection cuts for the tau "tag-and-probe" samples (T&P signal region sample and T&P lepton veto inverted control region sample) that are used to estimate the uncertainty on the tau scale factor ρ^τ_{MC}.

Muon selection that is compatible with a $\tau \to \mu\nu\nu$ decay	$p_{\mathrm{T}} > 25\,\mathrm{GeV}$
	$\lvert\eta\rvert < 2.4$
	$\sum\limits_{\Delta R < 0.4} p_{\mathrm{T}}^{\mathrm{PF\ particle}}/p_{\mathrm{T}}(\mu) < 0.12$
	$\left.\dfrac{\chi^2}{ndof}\right\rvert_{\mathrm{global\ track}} < 10$
	$\lvert d0 \rvert < 0.2\,\mathrm{cm}$
	$\lvert dz \rvert < 0.5\,\mathrm{cm}$
	≥ 1 hit in the muon detector
	≥ 2 hits in different muon detector planes
	≥ 1 hit in the pixel detector
	≥ 6 hits in the tracker system
Candidate track selection	Good quality selection
	Kinematic selection
	Lepton/jet veto (τ veto inverted for the "tag-and-probe" control region)
	$\sum\limits_{\Delta R < 0.3} p_{\mathrm{T}}^{\mathrm{trk}}/p_{\mathrm{T}}^{\mathrm{cand}} - 1 < 0.1$
	$N_{\mathrm{hits}} > 5$
Event-based selection	Muon and candidate track opposite in charge
	$40\,\mathrm{GeV} < M_{\mathrm{inv}}\,(\mu, \mathrm{cand.\ trk}) < 75\,\mathrm{GeV}$
	$m_T\,(\mu, \not{E}_{\mathrm{T}}) < 40\,\mathrm{GeV}$

Table A.13: Event selection cuts for the electron "tag-and-probe" samples (T&P signal region sample and T&P lepton veto inverted control region sample) that are used to estimate the uncertainty on the electron scale factor ρ^e_{MC}.

Electron selection	$p_{\mathrm{T}} > 25\,\mathrm{GeV}$
	$\|\eta\| < 2.5$
	$\sum\limits_{\Delta R < 0.4} p_{\mathrm{T}}^{\mathrm{PF\ particle}}/p_{\mathrm{T}}(e) < 0.15$
	pass conversion veto
	no missing tracker hits
	good MVA electron as defined in [28]
Candidate track selection	Good quality selection
	Kinematic selection
	Lepton/jet veto (e veto inverted for the "tag-and-probe" control region)
	$\sum\limits_{\Delta R < 0.3} p_{\mathrm{T}}^{\mathrm{trk}}/p_{\mathrm{T}}^{\mathrm{cand}} - 1 < 0.1$
	$N_{\mathrm{hits}} > 5$
Event-based selection	Electron and candidate track opposite in charge
	$80\,\mathrm{GeV} < M_{\mathrm{inv}}\,(e, \mathrm{cand.\ trk}) < 100\,\mathrm{GeV}$

₁₀₈₁ ## A.6 Optimisation results with the number of missing outer hits

₁₀₈₂ Also an optimisation in the number of missing outer hits is performed. No significant im-
₁₀₈₃ provement is visible in the search sensitivity for different selection requirements of $N_{\text{lost}}^{\text{outer}}$,
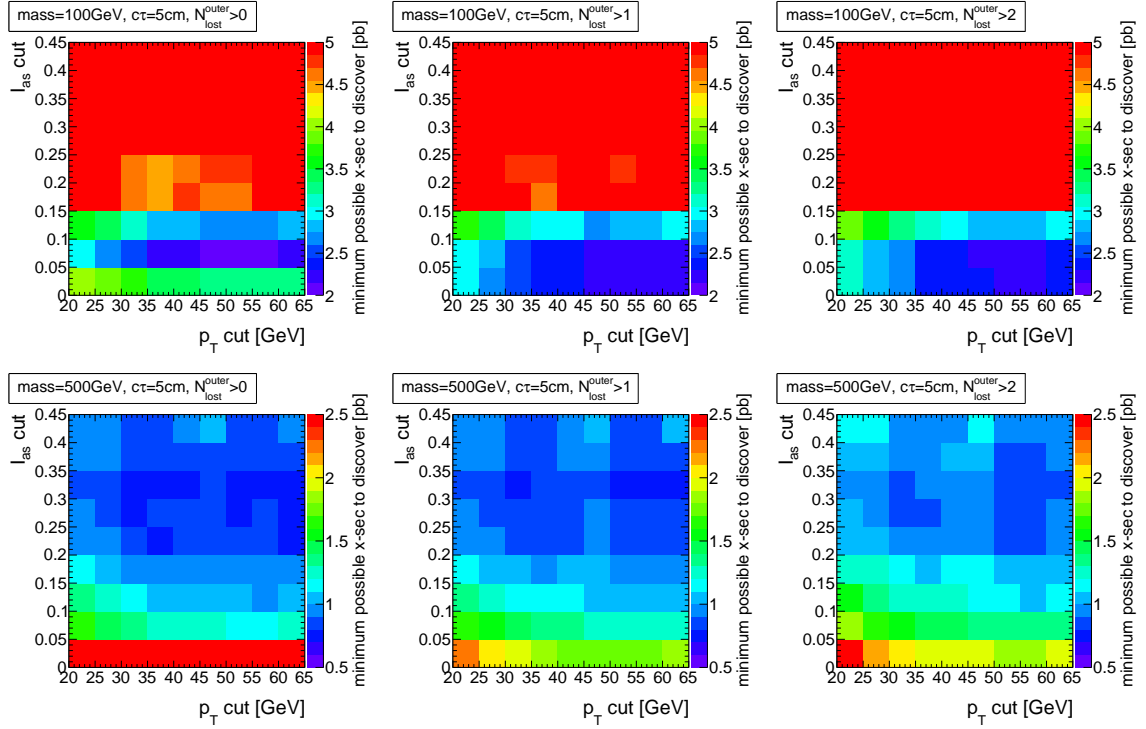see Fig A.1. This is caused by the fact, that the main background, the fake background,

Figure A.1: Minimum possible cross section that can be discovered with 5σ significance in
the $I_{\text{as}}p_{\text{T}}$ plane for two different signal models with a chargino lifetime of 5 cm
and a mass of 100 GeV (top) and 500 GeV (bottom). The requirement on the
number of missing outer hits is varied between $N_{\text{lost}}^{\text{outer}} > 0$ (left), $N_{\text{lost}}^{\text{outer}} > 1$
(middle), $N_{\text{lost}}^{\text{outer}} > 2$ (right). A difference in the sensitivity can be spotted
when looking at the lowest value of the minimum cross section that occurs. No
sizable discrimination improvement is visible for a tighter selection in $N_{\text{lost}}^{\text{outer}}$.

₁₀₈₄

₁₀₈₅ also shows missing outer hits. A comparison between the number of missing outer hits for
₁₀₈₆ the fake background and two signal models is shown in Fig. A.2.
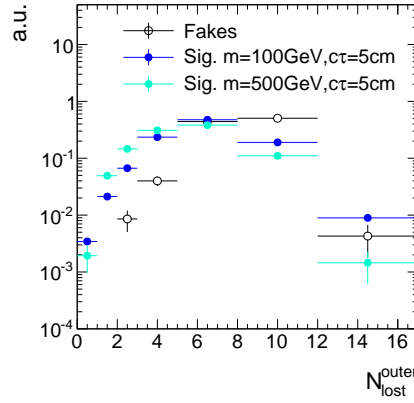
Figure A.2: Normalised distribution of the number of missing outer hits for fake tracks and two different signal models.

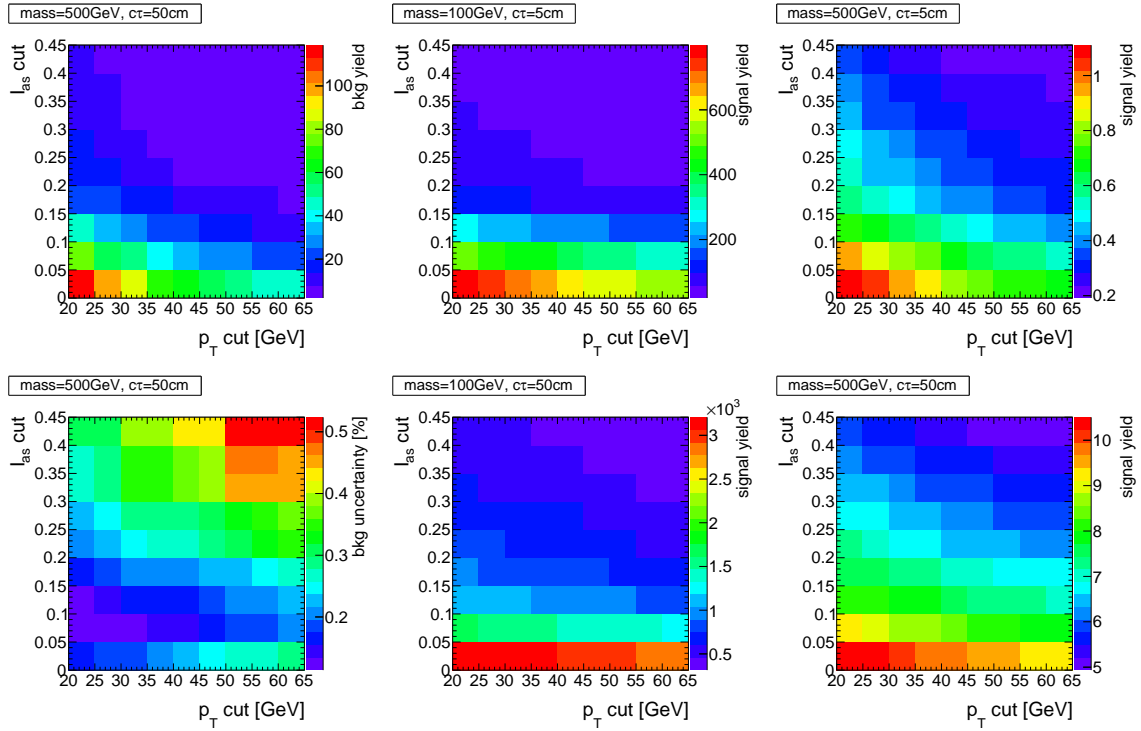## A.7 Underlying distributions for the qualitative search sensitivity optimisation

Figure A.3: Background yield, background uncertainty and signal yield for different p_T and I_{as} selection requirements and four different signal models.

A.8 Trigger emulation

As the HLTMonoCentralPFJet80_PFMETnoMu105_NHEF0p95 trigger is not available in the simulated signal samples, this trigger is emulated in these samples. Since HLT trigger information is stored in the samples, it is possible to rebuild the trigger afterwards.

The following requirements must be fulfilled in order to consider the trigger firing [29,30]:

- p_T of hltL1sL1ETM40 $> 40\,\text{GeV}$

- p_T of hltCentralJet65L1FastJet $> 65\,\text{GeV}$

- p_T of hltMET65 $> 65\,\text{GeV}$

- p_T of hltCentralPFJet80 $> 80\,\text{GeV}$

- p_T of hltPFMETWOM95 $> 105\,\text{GeV}$

As a cross check, also the HLTMonoCentralPFJet80_PFMETnoMu95_NHEF0p95 is rebuild with the looser selection of p_T of hltPFMETWOM95 $> 95\,\text{GeV}$. The correct implementation could be verified with this test.

A.9 Exclusion limits for all simulated lifetimes
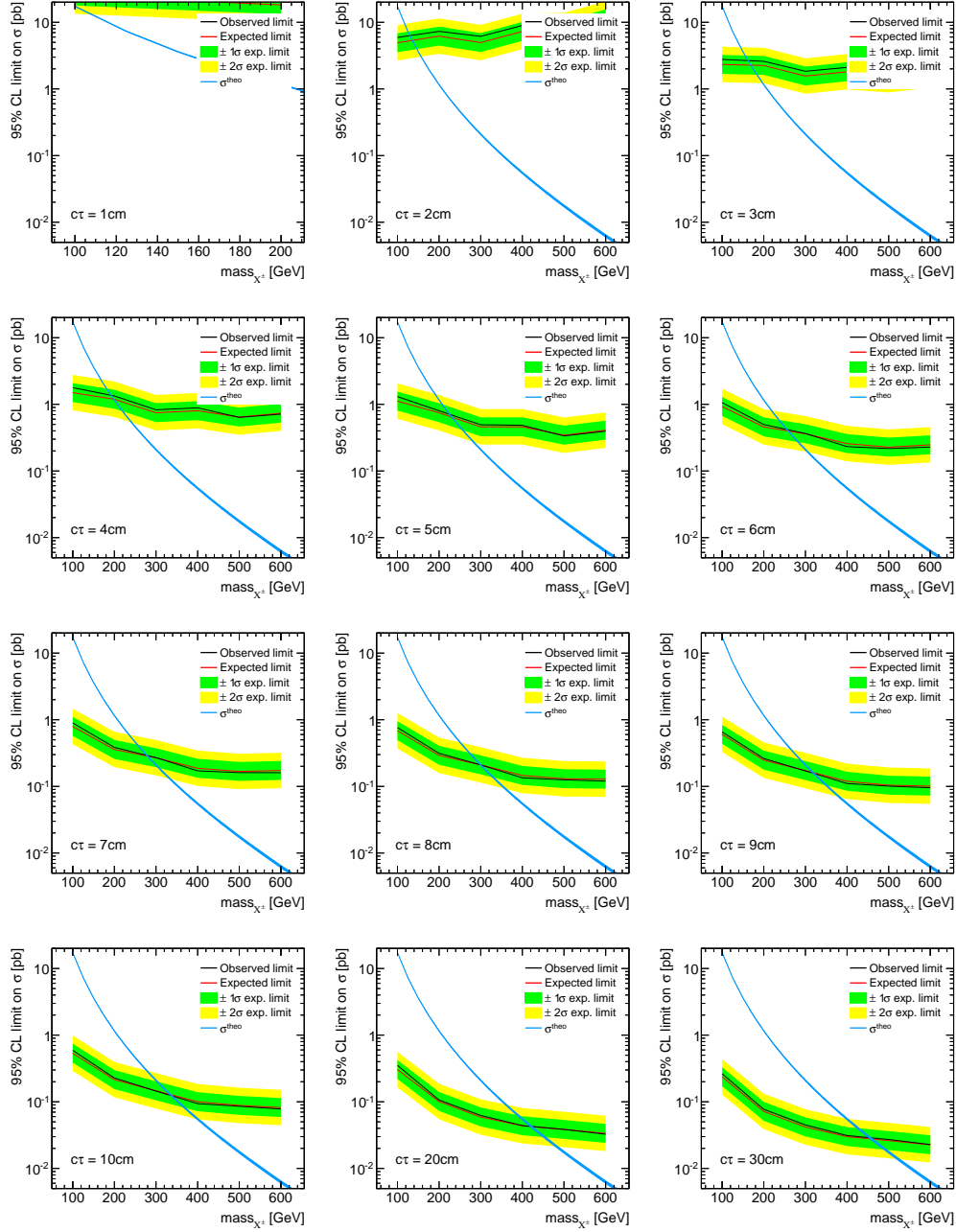
Figure A.4: 95% CL exclusion limits for signal models with $c\tau = 1 - 30\,\text{cm}$.
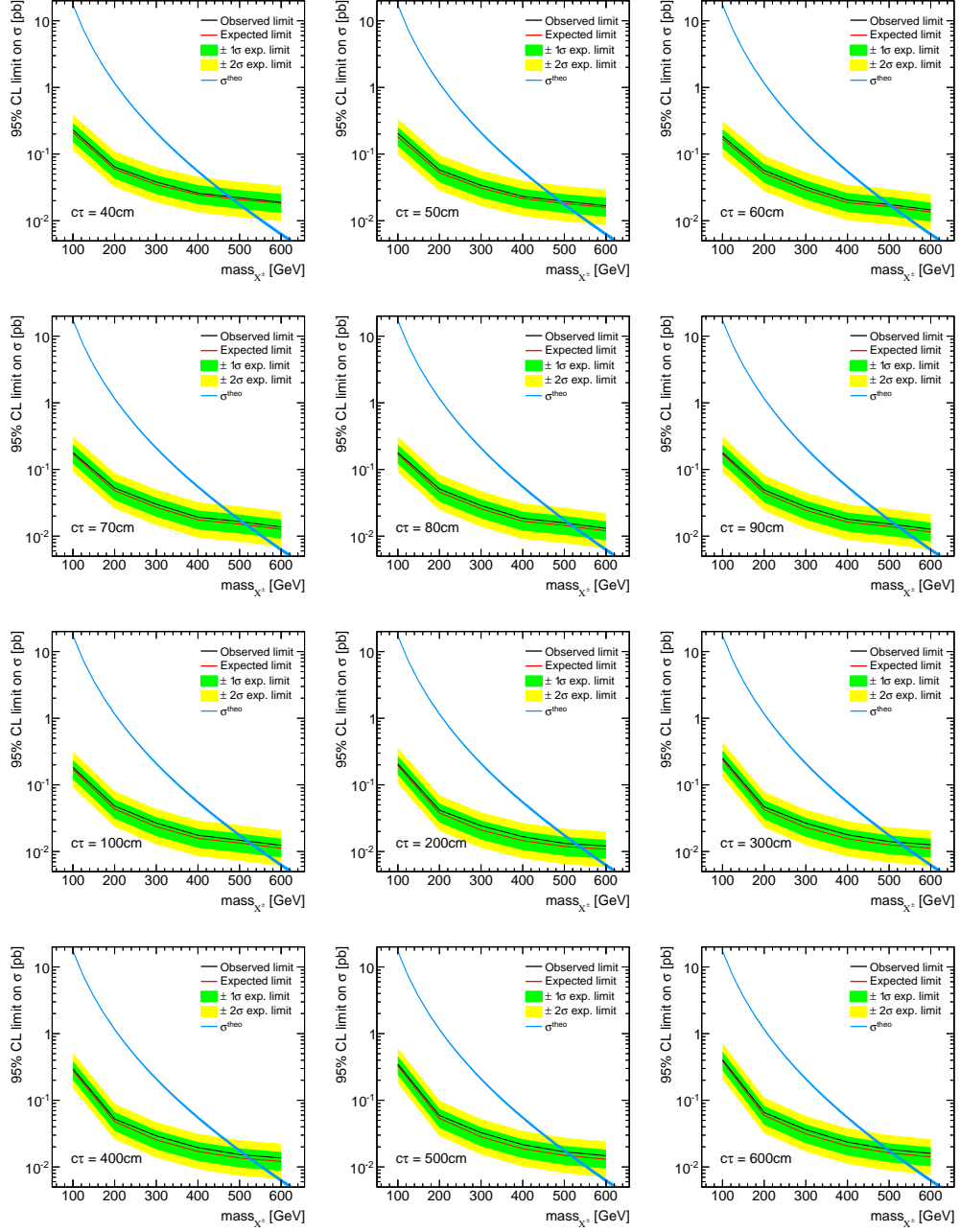
Figure A.5: 95% CL exclusion limits for signal models with $c\tau = 40 - 600\,\mathrm{cm}$.
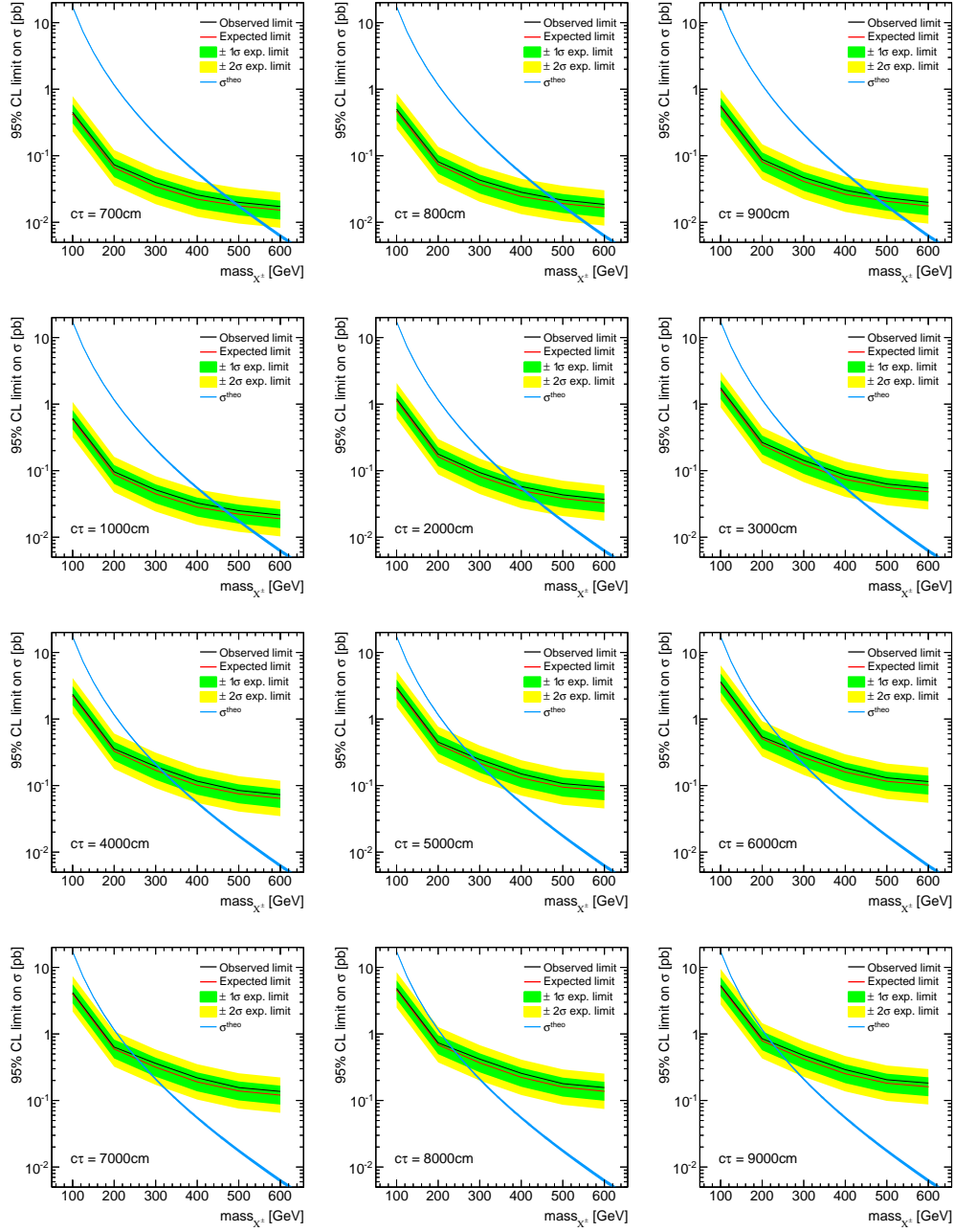
Figure A.6: 95% CL exclusion limits for signal models with $c\tau = 700 - 9000\,\mathrm{cm}$.

Bibliography

[1] CDF, D0 Collaboration, T. Adams, "SUSY Searches at the Tevatron", in *Hadron collider physics. Proceedings, 19th Symposium, HCP2008, Galena, USA, May 27-31, 2008*. 2008. `arXiv:0808.0728`.

[2] ALEPH, DELPHI, L3 and OPAL Collaborations, "Joint SUSY Working Group". `http://http://lepsusy.web.cern.ch/lepsusy/`. LEPSUSYWG (June 2004).

[3] CMS Collaboration, "Search for new physics in the multijet and missing transverse momentum final state in proton-proton collisions at $\sqrt{s} = 8$ TeV", *JHEP* **06** (2014) 055, `arXiv:1402.4770`. `doi:10.1007/JHEP06(2014)055`.

[4] CMS Collaboration, "Searches for Supersymmetry using the M_{T2} Variable in Hadronic Events Produced in pp Collisions at 8 TeV", *JHEP* **05** (2015) 078, `arXiv:1502.04358`. `doi:10.1007/JHEP05(2015)078`.

[5] ATLAS Collaboration, "Search for squarks and gluinos with the ATLAS detector in final states with jets and missing transverse momentum using $\sqrt{s} = 8$ TeV proton–proton collision data", *JHEP* **09** (2014) 176, `arXiv:1405.7875`. `doi:10.1007/JHEP09(2014)176`.

[6] T. Moroi and L. Randall, "Wino cold dark matter from anomaly mediated SUSY breaking", *Nucl. Phys.* **B570** (2000) 455–472, `arXiv:hep-ph/9906527`. `doi:10.1016/S0550-3213(99)00748-8`.

[7] J. Hisano, S. Matsumoto, M. M. Nojiri et al., "Direct detection of the Wino and Higgsino-like neutralino dark matters at one-loop level", *Phys. Rev.* **D71** (2005) 015007, `arXiv:hep-ph/0407168`. `doi:10.1103/PhysRevD.71.015007`.

[8] M. Ibe, S. Matsumoto, S. Shirai et al., "Wino Dark Matter in light of the AMS-02 2015 Data", *Phys. Rev.* **D91** (2015), no. 11, 111701, `arXiv:1504.05554`. `doi:10.1103/PhysRevD.91.111701`.

[9] T. Moroi, M. Nagai, and M. Takimoto, "Non-Thermal Production of Wino Dark Matter via the Decay of Long-Lived Particles", *JHEP* **07** (2013) 066, `arXiv:1303.0948`. `doi:10.1007/JHEP07(2013)066`.

[10] J. Hisano, S. Matsumoto, and M. M. Nojiri, "Explosive dark matter annihilation", *Phys. Rev. Lett.* **92** (2004) 031303, `arXiv:hep-ph/0307216`. `doi:10.1103/PhysRevLett.92.031303`.

[11] CMS Collaboration, "Search for disappearing tracks in proton-proton collisions at $\sqrt{s} = 8$ TeV", *JHEP* **01** (2015) 096, `arXiv:1411.6006`. `doi:10.1007/JHEP01(2015)096`.

[12] CMS Collaboration, "Searches for long-lived charged particles in pp collisions at $\sqrt{s}$=7 and 8 TeV", *JHEP* **07** (2013) 122, `arXiv:1305.0491`. `doi:10.1007/JHEP07(2013)122`.

[13] CMS Collaboration, "Phenomenological MSSM interpretation of the CMS 2011 5fb-1 results", *CMS Physics Analysis Summary* **CMS-PAS-SUS-12-030** (2013).

[14] CMS Collaboration, "Reinterpreting the results of the search for long-lived charged particles in the pMSSM and other BSM scenarios", *CMS Physics Analysis Summary* **CMS-PAS-EXO-13-006** (2014).

[15] CMS Collaboration, "Search for disappearing tracks in proton-proton collisions at $\sqrt{s} = 8$ TeV", *Public CMS Wiki* (2015). https://twiki.cern.ch/twiki/bin/view/CMSPublic/PhysicsResultsEXO12034, Topic revision: r9.

[16] CMS Collaboration, "Search for heavy long-lived charged particles in *pp* collisions at $\sqrt{s} = 7$ TeV", *Phys. Lett.* **B713** (2012) 408–433, `arXiv:1205.0272`. `doi:10.1016/j.physletb.2012.06.023`.

[17] CMS Collaboration, "Description and performance of track and primary-vertex reconstruction with the CMS tracker", *JINST* **9** (2014), no. 10, P10009, `arXiv:1405.6569`. `doi:10.1088/1748-0221/9/10/P10009`.

[18] H. Bethe, "Theory of the Passage of Fast Corpuscular Rays Through Matter", *Annalen Phys.* **5** (1930) 325–400. [Annalen Phys.397,325(1930)]. `doi:10.1002/andp.19303970303`.

[19] "National Institute of Standards and Technology". `http://physics.nist.gov/cgi-bin/Star/compos.pl?mode=text&matno=014`. Accessed: 2015-10-21.

[20] Particle Data Group Collaboration, "Review of Particle Physics", *Chin. Phys.* **C38** (2014) 090001. `doi:10.1088/1674-1137/38/9/090001`.

[21] L. Landau, "On the energy loss of fast particles by ionization", *J. Phys.(USSR)* **8** (1944) 201–205.

[22] H. Bichsel, "Straggling in Thin Silicon Detectors", *Rev. Mod. Phys.* **60** (1988) 663–699. `doi:10.1103/RevModPhys.60.663`.

[23] L. Quertenmont, "Search for Heavy Stable Charged Particles with the CMS detector at the LHC". PhD thesis, Louvain, U., 2010. `https://inspirehep.net/record/1088192/files/openfile.pdf`.

[24] D. Kotlinski. personal communication.

[25] T. W. Anderson, "On the Distribution of the Two-Sample Cramr-von Mises Criterion", *The Annals of Mathematical Statistics* **33** (1962), no. 3, pp. 1148–1159.

[26] F. James, "Statistical methods in experimental physics". 2006.

[27] CMS Collaboration, "Tracking and Vertexing Results from First Collisions", *CMS Physics Analysis Summary* **CMS-PAS-TRK-10-001** (2010).

[28] CMS Collaboration, "Measurement of Higgs boson production and properties in the WW decay channel with leptonic final states", *JHEP* **01** (2014) 096, `arXiv:1312.1129`. `doi:10.1007/JHEP01(2014)096`.

[29] J. D. Brinson, "A search for disappearing tracks in proton-proton collisions at $\sqrt{s} = 8$ TeV". PhD thesis, Ohio State U. `https://inspirehep.net/record/1381347/files/CERN-THESIS-2015-030.pdf`.

[30] C. H. J. Brinson and W. Wulsin, "Search for disappearing tracks", *CMS Analysis Note* **CMS-AN-12-400** (2014). Internal documentation.

1184